Southern Methodist University

SMU Scholar

Fall 2018

Molecular Dynamics Studies on Nanoscale Confined Liquids

Alper Celebi

Southern Methodist University, alper_tungacelebi@hotmail.com

Recommended Citation

Celebi, Alper, "Molecular Dynamics Studies on Nanoscale Confined Liquids" (2018). *Mechanical Engineering Research Theses and Dissertations*. 14.
https://scholar.smu.edu/engineering_mechanical_etds/14

MOLECULAR DYNAMICS STUDIES ON NANOSCALE CONFINED LIQUIDS

Approved by:

_____
Prof. Ali Beşkök
Professor in Mechanical Engineering

_____
Prof. MinJun Kim
Professor in Mechanical Engineering

_____
Prof. Wei Tong
Professor in Mechanical Engineering

_____
Prof. Xin-Lin Gao
Professor in Mechanical Engineering

_____
Prof. Vladimir Ajaev
Professor in Mathematics

MOLECULAR DYNAMICS STUDIES ON NANOSCALE CONFINED LIQUIDS

A Dissertation Presented to the Graduate Faculty of

Bobby B. Lyle School of Engineering

Southern Methodist University

in

Partial Fulfillment of the Requirements

for the degree of

Doctor of Philosophy

with a

Major in Mechanical Engineering

by

Alper Tunga Çelebi

(B.S., Istanbul Technical University, Mechanical Engineering, 2011)
(M.S., Istanbul Technical University, Mechanical Engineering, 2013)

December 15, 2018

ACKNOWLEDGMENTS

Çelebi, Alper Tunga   B.Sc., Istanbul Technical University, Turkey, 2011
                                                   M.Sc., Istanbul Technical University, Turkey, 2013

Molecular Dynamics Studies on Nanoscale Confined Liquids

     Advisor: Professor Ali Beşkök

Doctor of Philosophy in Mechanical Engineering degree conferred December 15, 2018

Dissertation completed October 25, 2018

Liquid transport in nanochannels have been attracting great interests, especially for last two decades, owing to its potential applicability in various fields including biochemistry, medical science and engineering. For exploring and generating new ideas in the field of nanofluidics, molecular simulation techniques have become an ideal way due to the experimental challenges impeding the field of nanofluidics in fabrication and measurements.

In this dissertation, we perform molecular dynamics simulations to investigate liquid transport behavior in nanoscale channels. The expanse of this dissertation concerns several fundamental topics in nanoscale liquid transport phenomena such as liquid properties in nanoscale confinements, interfacial flows and slippage of fluids at the solid interface, electrokinetic transport phenomena, and limits of continuum solutions along with developing continuum models. Our objectives are to systematically investigate the effects of several physical variables such as channel size, wall curvature, surface charge, salt ions, liquid-wall interfacial strength and driving force on the nanoconfined liquid behavior. Specifically, we examine the variations of density distributions, molecular orientations, velocity profiles, viscosities, slip lengths and flow rates, and identify the deviations from well-known continuum bulk properties at predefined thermodynamic state. Furthermore, we develop continuum-based analytical solutions with slip corrections for electroosmotic flows that accurately predict transport in nanochannels.

TABLE OF CONTENTS

LIST OF FIGURES

LIST OF TABLES

This work is dedicated to my parents Sema & Osman Çelebi, my sister Deniz and her

husband Kerem and their little baby, our beloved Minnoş Balkan Alaz.

Chapter 1

INTRODUCTION

1.1 Nanofluidics

Nanofluidics often refers to study and application of fluid motions through and around nanosized objects with a characteristic length scale in the range of 0-100 nm[1]. Research about the fluids at nanoscale have been around for several decades. Rapid developments in nanoscience and nanotechnology have led various advanced tools and fabrication techniques that became widely accessible for scientific usage such as atomic force microscope (AFM), scanning tunneling microscope (STM), x-beam and ion-beam lithography, micromachining techniques[2]. Owing to these novelties, probing and controlling of fluids at nanoscale have become much easier, and nanofluidics has received its own name along with an exceptional worldwide interest.

Nanometric scale enables new fluidic functionalities to be emerged[3]. These newly established nanoscale features are one of the main motivations for development and fabrication of new nanofluidic devices for various applications spanning from drug delivery[4] to water desalination[5], energy storage[6], biosensing[7] nanoelectropumping[8], and heat management[9] etc. Such diverse applications of nanofluidics clearly involve a vast array of core subjects which requires a multidisciplinary understanding. In Fig. 1.1, a schematic representation demonstrates various disciplines that nanofluidics could interact

1

with[2]. From chemistry to colloidal science, physics, engineering and most importantly biology carry the fingerprints of nanofluidics. One must know that nanofluidics is not only related to molecular level applications, it is also implicit with many natural phenomena that happen at larger scales. For example, oil and water transport in shale reservoirs is a matter of nanofluidics due to nanometer pore size in shale reservoirs.[10] In another example, insects can run on the water regarding the relation between the surface tension and their nonwetting nanogrooved legs. Furthermore, tree leaves can provide water flow from root using nanoscale capillary effect due to osmotic pressure difference.
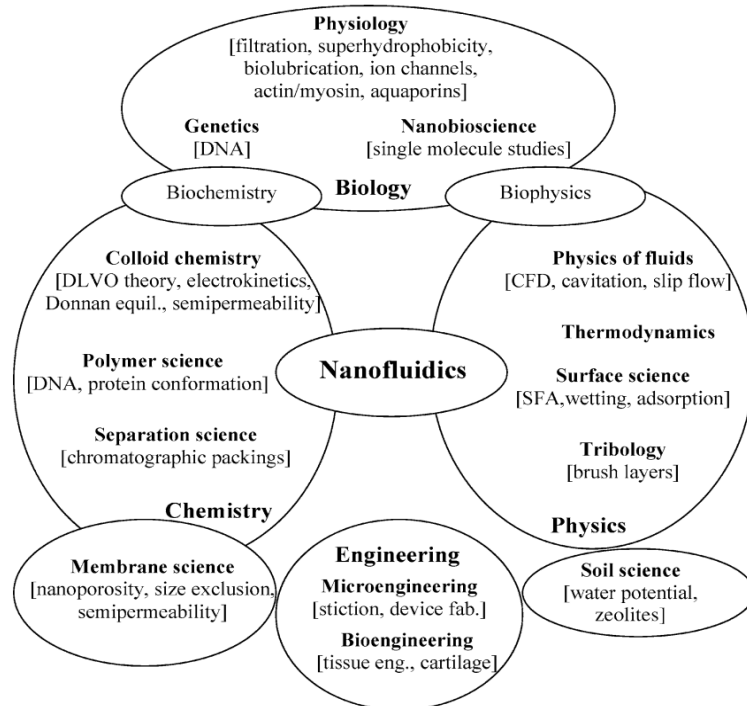
Fig. 1.1 Nanofluidics and Relevant Disciplines. Adopted from *Nanofluidics: what is it and what can we expect from it?* by JCT Eijkel and A. Van Den Berg, *Microfluidics and Nanofluidics*, 1, 249 (2005)[2].

1.2 Fluid Flow in Nanochannels

Progress in nanotechnology has pushed the characteristic length scale of devices from micrometers down to nanometers, which resulted in a demand for enhanced

understanding of liquid transport phenomena in nanochannels[11]. Nanochannel liquid flows can be utilized in various applications including drug delivery, pumping, ion separation, where carbon nanotubes, boron nitride nanotubes, planar silicon channels and single layer graphene membranes are some of the typical examples of the liquid carriers. In such systems, surface area to volume ratio becomes very high. Accordingly, the interplay between interfacial and bulk phenomena is extremely significant due to the comparable size of the fluid molecules with channel dimensions. This results in a non-local nature of momentum and energy transport[12]. Importantly, at this scale, well-established continuum flow theories may fail and the no-slip boundary condition may be no longer valid[12]. In other words, local thermodynamic equilibrium, definitions of hydrodynamic properties such as velocity profiles, density distributions, viscosity, flow rate and classical boundary conditions could be significantly different than their macroscopic counterparts defined in well-known Navier-Stokes equations[13-14].

Density is the first significant quantity that may alter the liquid transport properties in nanochannels. For decreasing domain size, molecular interactions become extremely important at the liquid/solid interface. Liquid molecules near the solid surfaces experience strong wall-force field effect, creating solid-like density oscillations normal to the surface[15-17]. This density inhomogeneity may create spatially varying density dependent transport properties[18]. Herein, a distinct physics could be observed in nanoscale than what is observed in the continuum regime[19]. For example, the average liquid density in nanochannels are typically lower than the bulk thermodynamic value. As the channel height increases, the effect of interfacial density layering disappears, and the bulk density converges to the desired thermodynamic value[20-22]. As a result, liquid show

different average channel densities for different channel heights, creating size related local thermodynamic state and transport properties. To avoid this, one can simply fix the local thermodynamic state by controlling the temperature and bulk density[18, 23]. In addition, the surface wettability greatly affects the density profiles both in layering and bulk regions. High wettability implies strong liquid-wall interaction strength that shows more pronounced layering due to the accumulation of water molecules near the wall, while low wettability implies weak wall coupling and less pronounced density layering[24].

Secondly, hydrodynamic boundary conditions at the liquid-solid interface also play a critical role in characterization of the liquid transport behavior in nanoconfinements. Liquids on solid surfaces can show no-slip, slip or stick boundary conditions depending on the liquid-solid coupling strength as illustrated in Fig 1.2. No-slip boundary conditions are traditionally accepted in continuum flow theory, and assumes zero tangential velocity at the liquid-solid interface[25]. Stick conditions correspond to molecular adsorption at the interface, and results in reduced channel dimensions and flow rate[26]. For weak liquid-wall coupling strengths, a finite slip-velocity is observed at the interface, where this slip behavior is typically quantified using the "s*lip length*". Slip length is the extrapolated distance relative to the wall where the tangential velocity component vanishes as illustrated in Fig 1.2c. Navier-type slip condition represents the slip length (β), relating the slip-velocity (u_s) and shear rate, which will be explained in detail in Chapter 3. Slip behavior is closely related to the surface properties. Slip increases as interaction strength between the liquid molecules and solid walls decreases, which is also traditionally related to reduced wettability. Hydrophobic surfaces have nonwetting nature with a contact angle generally larger than 90° showing strong slip behavior while hydrophilic surfaces have

wetting nature with a contact angle generally smaller than 90° showing weak slip behavior. Furthermore, high surface density and smooth surface implies large slip behavior at the interface due to low surface potential corrugations[27]. For example, carbon-based nanomaterials combine all these attributes, resulting in large liquid slip behavior. Accordingly, any factor altering the liquid-wall coupling can create variations in the interfacial slip behavior. Multiple studies in the literature investigated the effects of various physical parameters on liquid slip in nanochannels such as the channel size[14, 28], surface roughness[29], wall curvature[30], surface wettability[31], temperature[32], surface charge[33], shear rate[34], as well as thermal or cold wall models used in atomistic simulations[35]. It is theoretically possible that one can achieve tunable liquid transport in nanochannels by actively controlling the liquid slip at the interface.
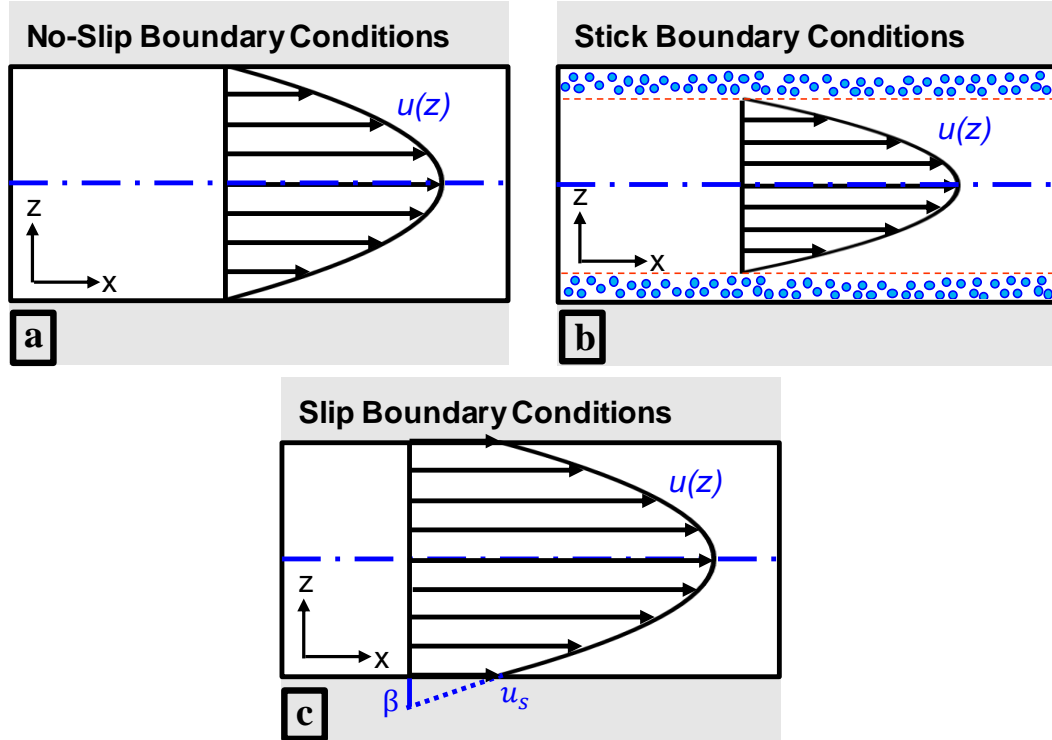
Fig. 1.2 Hydrodynamic boundary conditions (a) No-slip (b) Stick and (c) Slip.

Furthermore, slip strongly correlates with the liquid velocity profiles and flow rate in the channel. Increased slip length implies a weak interfacial resistance, which significantly enhances the liquid flow rate, while stick (adsorption) conditions imply strong interfacial resistance and hinder the flow. In literature, a flow enhancement factor is defined to quantify the variations in the flow due to the slip effect, which is the ratio of the actual flow rate (either measured in experiments or calculated from simulations) to that of predicted by no-slip continuum flow equations. Furthermore, one can also quantify the slip effect on the nanoscale transport phenomena using these well-known continuum flow equations. For example, nanochannel pressure driven flow can be described by Poiseuille flow relation with slip corrections[28] while nanoscale electroosmotic flow could be defined by slip modified Helmholtz-Smoluchowski model[36]. It is also imperative to know that the channel height is crucial in describing the flow rate. As the slip length is comparable with critical channel dimensions, the channel permeability significantly enhances, that enables many potential applications[12]. For pressure-driven channel flow, a 50 nm slip length value show insignificant effect on the mass flow rate in a 10 μm height channel but exhibits 31-fold enhancement in flowrate for 10 nm high channel.

Described by classical Navier-Stokes equations, liquid transport is implicitly a function of the liquid viscosity. Many studies show the apparent liquid viscosity in nanoconfinements could be different than what is expected in continuum scale at a specified thermodynamic state mainly because of the surface charge effects[37-38], ion effects[39-40] or size effect[41-42]. For instance, the viscosity of water in nanoconfinement shows a substantial increase with increased surface charge and/or the presence of salt

ions in the solution[23, 36, 43]. Homogenous bulk fluid viscosity is still observable for channel sizes of 5 molecular diameters, while it shows the strong effect of density oscillations for narrower pore sizes [17, 44 45] . For these reasons, one must determine the apparent viscosity of liquids in intrinsic conditions to correctly predict the flow in nanochannels. Furthermore, the globality of the liquid viscosity in nanoconfinements is still controversial, and no consensus has been reached yet. Several studies report locally varying liquid viscosity in nanochannels[37, 45] while some contradict with the apparent viscosity as a global (non-local) property since the velocity profiles are not locally varied, that requires to have a single value[33, 46].

Liquid viscosity and slip length at the interface can be predicted using molecular dynamics (MD) simulations. Equilibrium MD simulations are adopted using Green-Kubo relation[47-49] and Stokes-Einstein relation[50-51] in order to find the viscosity of liquids. Green-Kubo relation can be also used to find friction coefficient in nanochannels, where the ratio of the friction coefficient to shear viscosity defines the slip length[12, 52]. Equilibrium MD methods generally require large simulation time to converge, thus they are computationally expensive. Non-equilibrium MD simulations provide an alternative approach for evaluating the slip length and apparent viscosity in nanochannel based on the velocity profiles. Simulating the Couette flow results in a simple linear velocity profile, and slip length is found by extrapolation of this straight line. Poiseuille flow simulations may show different velocity profiles across the channel from perfect parabola to flat line depending on the liquid-solid interaction strength. Using polynomial curve fitting to parabolic velocity profiles, one can pull out the apparent viscosity and slip lengths in nanochannels[53-54]. Parabolic velocity behavior is correlated with strong liquid-

wall coupling such as interaction between water and silica surface. However, using hydrophobic surfaces (i.e. graphene) result in weak interactions, creating plug flow across the channel rather than a parabola. For such cases, a plug-flow method is used to find the slip length instead of the curve fitting method[18, 23].

Liquids in channels could be driven by using various external means such as pressure-drop, temperature gradient or electrokinetic effect. Electrokinetic effect is one of the most significant aspects in liquid transport phenomena, which provides easy and efficient flow control particularly in micro/nanochannels[19]. When an ionic solution is in contact with the static charges of a dielectric surface, an electrical double layer (EDL) with a net charge forms over the surface. EDL is the essential for all electrokinetic related phenomena such as electroosmosis[55]. Electroosmosis is the motion of ionic liquid due to the moving ions in EDL when an external electric field is applied in the direction tangential to the surface. Electroosmotic flow (EOF) is practical in narrow channels since it enables low electric field instead of unrealistically large pressure drops to create the same mass flux. The flow rate for EOF between two parallel plates scales linearly with the channel height, while the flow rate in pressure-driven flows varies with the cube of the channel height and varies linearly with the channel width[56]. Furthermore, one must consider the variations in slip length, viscosity enhancements arising from the interface and finite-size effects when elucidating electroosmotic nanochannel flows. Molecular level simulations can be successfully applied to acquire a greater and improved perspective in electrokinetic theory. In an early study, Qiao and Aluru[45] performed non-equilibrium MD simulations to investigate electroosmotic flow of ionic solution in silicon nanochannels with different channel heights. They also compared their MD results with

predictions based on the classical continuum flow theory. The discrepancies in the ion distributions are handled by introducing a correction term to the Poisson-Boltzmann equation. The validity of continuum-based equations in electrokinetic flows were also discussed in terms of velocity distribution, where continuum solutions fails in predicting the molecular velocity profiles due to the absence of slip contribution[29]. Marry *et al.*[57] reported a short study to model slip contribution on the channel walls for a nanoscale EOF. Later, Joly *et al.*[58] presented an extensive study on the hydrodynamics within the electric double layer on slipping surfaces. Recently, multiscale transport models for EOFs are reported including the effects of interfacial friction and viscosity variations[36, 59]. Furthermore, a number of MD studies in literature focus on electrokinetic flows focusing on different aspects including effects of surface roughness[60-61], surface charge density[62], and ionic concentration[63].

In conclusion, liquid flows inside nanochannels require an advanced understanding of nanoscale liquid transport phenomena. Many theoretical, computational and experimental studies have been devoted to this purpose in the literature. Experiments generally provide reliable and accurate insight to the nanofluidic systems. However, various aspects in nanofluidics such as prediction of electrokinetic nanochannel flows, quantification of interfacial friction between liquid molecules and solid surface or determination of local thermodynamic variables of liquids in confinements cannot be easily observed in experiments[64]. Furthermore, classical continuum theories are occasionally incapable of explaining the intrinsic nanoscale phenomena. For instance, flow reversal due to charge reversal in electroosmotic flow is beyond the capability of well-known classical Poisson-Boltzmann model[65]. Particle based simulations such as

molecular dynamics, Monte Carlo and dissipative particle dynamics are employed to model the nanoscale transport. Molecular dynamics is one of the most well-known methods for atomistic modeling and simulations of nanofluidic systems.

Chapter 2

MOLECULAR DYNAMICS SIMULATIONS

2.1 Historical Background

Through the rapid advances in computer technology during the last century, computational modeling and numerical simulations become essential in providing mathematical descriptions of many natural systems in physics, chemistry, biology, engineering as well as social sciences. Computer simulations are alternative approaches to the experiments for studying dynamical behaviors of objects or systems in response to the conditions that cannot be easily, safely and inexpensively applied in real life. For example, probing atomic particles are difficult due to the small scale and mostly require the use of expensive advanced tools, while computer simulations are perfectly feasible to overcome these difficulties. Furthermore, predictions based on simulations can be useful in validating existing theories and bringing insights to experimental measurements and observations (See Fig. 2.1).

At molecular level, computer simulations act as a bridge connecting microscopic length and time scales with the macroscopic world as well describing a relationship between the theory and experiment[66]. They provide a direct passage from microscopic details of a system (molecular interactions, atomic masses, geometry etc.) to macroscopic properties of experimental interest (equation of state, transport coefficients, structural
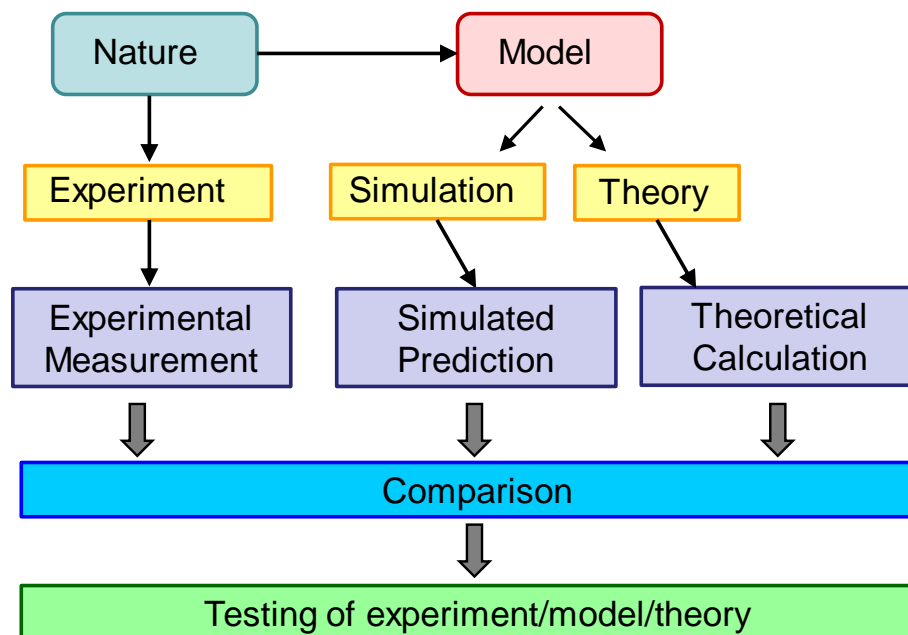
Fig. 2.1 Understanding the nature through experimenting and mathematical modelling.

Properties). Considering experimental challenges of probing molecular motions due to the size and the speed effects, molecular simulations have been serving as a complement to conventional experiments for several decades. In a very early study, Morell and Hildebrand[67] used a large number of macroscopic size gelatin balls suspended in liquid gelatin, representing the molecules in a closed system, where they were mechanically shaken in their vessel. The positions of the balls were computed by periodically taking the photographs of the system. This approach allowed a crude three-dimensional picture of the dynamics and structure of a molecular liquid. Since then, several methods have been developed over the years for modeling nanoscale particles and simulating their motions. The two main families of these methods are Molecular Dynamics and Monte Carlo (MC) simulations. In early 1950s, Monte Carlo method was first attempted to investigate properties of neutron travel through radiation shielding[68] and then it was used

to predict the interactions between simple molecules[69]. Following the successes of Monte Carlo simulations, a new technique named molecular dynamics is developed to predict the dynamical behavior of molecular systems based on the fundamental principles of physical laws. Alder and Wainwright[70] were pioneers who first carried out MD simulations using IBM 704 computer using elastic collisions between hard spheres in 1957. Later, Rahman[71] solved equations of motions to calculate the self-diffusion coefficient of liquid argon using Lennard-Jones (LJ) potential. In 1967, Verlet[72] presented a study on the calculation of equilibrium properties of liquid argon at different thermodynamic conditions using MD simulations. With the implementation of larger molecules in the simulations, MD's popularity has grown immensely. Harp and Berne[73] studied linear and angular momentum autocorrelation functions in diatomic liquids using MD. Later, researchers attempted to model liquid water molecules[74]. In the following years, more complicated molecules such as hydrocarbons[75-76], proteins[77], polymers[78] have been studied, which allowed scientists to utilize MD in various research areas including material science, biochemistry and biophysics etc. MD method has been improved step-by-step from 1950's till today, although much of the fundamental methodology is the same. Today, it is accessible to a very wide variety of real-life applications spanning from DNA sequencing to water desalination, energy storage, advanced material design, phase transition etc.

2.2 Fundamentals of Molecular Dynamics

Molecular dynamics is a computational method for simulating physical motions of a set of interacting particles (i.e. atoms and molecules) for a given period of time. In MD simulations, positions and velocities of the particles are determined by numerically

solving the Newton's equation of motion in time, where the forces and potential energies between the interacting particles are calculated based on the interatomic potentials or molecular force fields[79]. This accessible dynamic behavior of the atomistic systems is one of the most important advantages of MD over other atomistic simulation methods such as MC simulations. Furthermore, affordable computational cost, high capability to study considerably large systems and good accuracy also make MD a very powerful tool. The number of atoms in a typical MD system may vary from thousands to millions, where the total simulation time may be in the range of picoseconds to a couple of hundreds of nanoseconds. In this time scale, inter-atomic potentials are calculated using a characteristic time step which must be chosen small enough to avoid any discretization errors in the integration algorithm (i.e., smaller than the fastest vibrational frequency in the system and typically 1 *fs*)[11]. Number of particles, total time and time step are important parameters because MD simulation must represent kinetics of a natural process to make statistically valid conclusions. Depending on these criteria, CPU time needed for MD simulations span from minutes to several weeks, where high computing clusters and parallel computation is required. In addition to these limitations, several assumptions are made in MD technique, such as domain periodicity, thermostatting, rigid molecule assumptions and etc.

The motion of the atoms in a microscopic system is determined by the intra/inter-atomic forces arising from interactions of electrons and nuclei. These forces are defined as the gradient of the potential energy function (force-field) between the interacting particles. Therefore, final macroscopic properties of an N-body system in a MD simulation are directly dependent on the ability of the potential energy function of

interacting particles to represent the real conditions. In a typical MD simulation, equations of motion are integrated using numerical algorithms until a steady-state is reached and then statistical averaging is done to collect data. Fig. 2.2 shows the general schematics of molecular dynamics simulations.
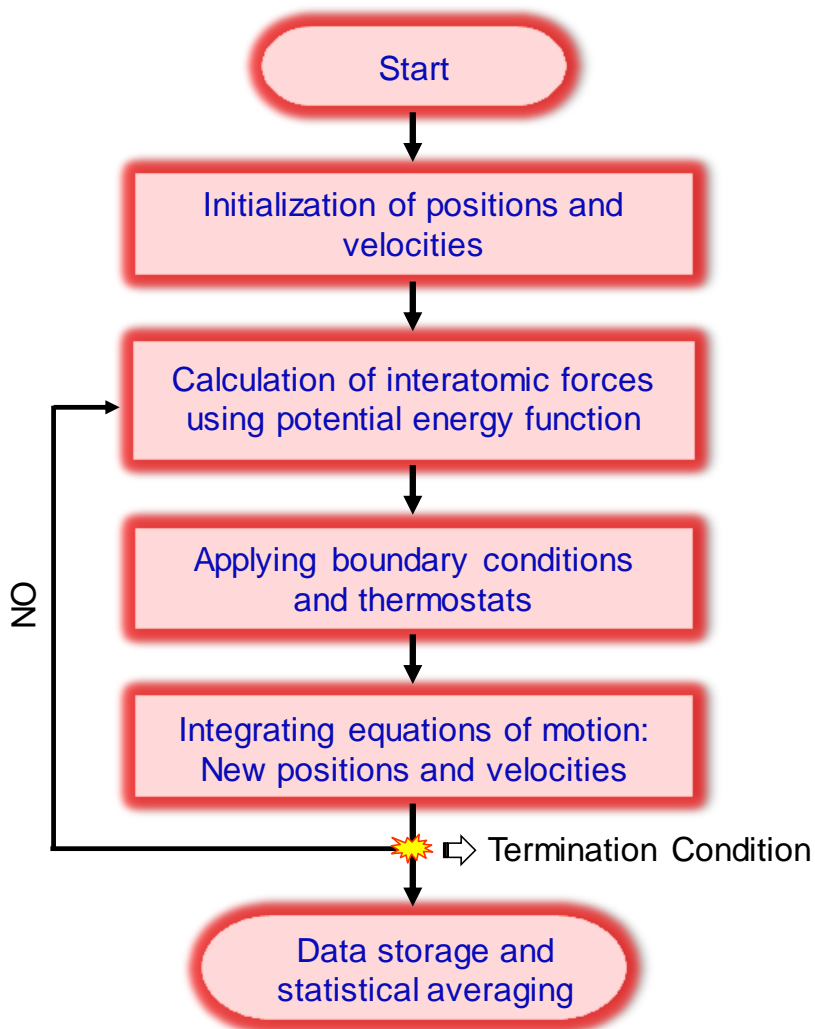
Fig. 2.2 Schematic of the molecular dynamics algorithm.

2.3 Statistical Mechanics and Thermodynamic Ensembles

Molecular dynamics simulations are based on the frameworks of statistical mechanics and thermodynamics[80]. MD corresponds to ensemble averages of the

microscopic properties of a large number of particles in a molecular system obtained by integrating the equations of motion at a particular thermodynamic state. It generates a sequence of points in phase space as a function of time, where these points belong to the same ensemble corresponding to the different conformations of the system (positions) and their respective momenta (velocities)[81]. The conversion of these microscopic properties to macroscopic observables such as pressure, energy, heat capacities, etc., is done via statistical mechanics. In statistical mechanics, an ensemble is described as the collection of possible microscopic states of a molecular system satisfying the requirements of a particular thermodynamic state. A thermodynamic state of a system is usually described by a set of parameters such as temperature (T), pressure (P) and the number of particles (N), volume (V), energy (E) or chemical potential (μ_c). The commonly used ensembles in statistical mechanics are isobaric-isothermal ensemble (*NPT*), microcanonical ensemble (*NVE*) canonical ensemble (*NVT*) and grand canonical ensemble ($\mu_c VT$), where some of these thermodynamic ensembles are satisfied using thermostats.

2.3.1 Microcanonical Ensemble (*NVE*)

Microcanonical ensemble represents the combination of possible thermodynamic states of an atomic system at specified total energy. It is also called as *NVE* because the total energy and volume are conserved. Equation of motions is solved without any control of pressure and temperature, so that the system is isolated from its environment, preventing energy exchange. Therefore, the energy remains constant with time. Although it is required constant energy, there are often small drifts in energy due to rounding and truncation errors. Microcanonical ensemble represents an ideal thermodynamic situation.

In practice, it is difficult to obtain fixed energy state because of the ambiguities in the temperature, pressure, entropy, etc. For equilibrium simulations, microcanonical ensemble is not recommended since desired temperature might not be achieved without any control of temperature using heat bath. For such cases, microcanonical ensemble is practical to confirm constant energy state and desired temperature after equilibrium state reached. Microcanonical ensemble is useful for such a system at constant energy, consisting of N particles in an insulated box where no heat flows in or out. One can investigate the distribution of energy and thermodynamic properties for different particles in this system.

2.3.2 Canonical Ensemble (*NVT*)

Canonical ensemble represents the combination of possible thermodynamic states of an atomic system in thermal equilibrium using a heat bath at a constant temperature. The canonical ensemble is the most popular ensemble in practice since, one is generally concerned with the systems in thermal equilibrium. The system can exchange energy with its environment, so that the total energy may change as a function of time. In this ensemble, temperature is controlled through direct temperature scaling in the initialization and by thermostats during the data storage stage. Canonical ensemble is named *NVT* because the volume is kept constant in addition to the temperature. The microcanonical ensemble is a special case of the canonical ensemble in equilibrium where the energies in canonical and microcanonical ensembles become approximately a constant value. *NVT* does not have a control on the pressure of the system. There might be perturbation on the trajectories using canonical ensemble if pressure is a significant factor.

2.3.3 Isothermal and Isobaric Ensemble (*NPT*)

NPT ensemble controls both temperature and pressure using appropriate thermostat/barostat. In this ensemble, volume is not constant and adjusted to maintain the desired pressure. It is useful when the pressure and temperature are significant in the system, where volume and density are directly related to these quantities. *NPT* can be used for equilibrium simulations to simultaneously achieve desired temperature and pressure state. *NPT* particularly provides a good approximation if the constant volume approach is inconvenient such as in case with phase change.

2.3.4 Grandcanonical Ensemble ($\mu_c VT$)

The grandcanonical ensemble represents the combination of possible thermodynamic states of an atomic system in thermal and chemical equilibrium using a heat and particle bath. In the reservoir, the system is allowed to exchange energy and particles for reaching thermal and chemical equilibrium, so that the energy and total number of particles are not constant. This ensemble also called as μ_cVT since the volume, chemical potential and absolute temperature remain constant in the simulation. For example, consider a liquid or solid in contact with its vapor in equilibrium so that particles can exchange between liquid and vapor and heat is traded between thermostat bath and the system.

For all these statistical ensembles, thermostatting and barostatting is achieved for constant temperature and pressure which is directly associated with the particle velocities (thermostatting) and simulation domain dimensions (barostatting). In MD simulations, thermostat is a more commonly used concept, where it modulates temperature by adding or removing energies from the boundaries of a system. The main objective of a

thermostat is to ensure that an average stable temperature of a system is to be correct rather than keeping the temperature constant. This is important because temperature may not be stable in the simulations due to several reasons such as force truncation, integration errors, heating due to friction and external forces. Temperature control is obtained by scaling atom velocities at the relevant value, which may update the equation of motions. Several algorithms are introduced to control temperature such as Anderson thermostat, velocity rescaling, Berendsen thermostat, Nosé-Hoover thermostat and Langevin thermostat. Among all, Nosé-Hoover thermostat is one of the first and most popular method, where it introduces a thermal reservoir (heat bath) and a frictional parameter (ξ) in the equations of motion. The bath acts as a source of thermal energy, providing or removing heat from the domain as required. The frictional term is a time-dependent quantity which has own equation of motion. The equations of motion for this thermostat is given by

$$\frac{d^2\bar{r}_i}{dt^2} = \frac{\bar{F}_i}{m_i} - \xi\frac{d\bar{r}_i}{dt} \tag{2.1}$$

where $\bar{F}_i$ is the force on the particle, $\bar{r}_i$ is the particle position, m_i is the particle mass. The time derivative is computed using the difference between kinetic energy and the reference temperature[82] as

$$\frac{d\xi}{dt} = \frac{1}{Q}(T - T_0) \tag{2.2}$$

where T is the instantaneous temperature, T_0 is the reference temperature and Q is the mass parameter of the reservoir, which shows the strength of the coupling associated with the reference temperature. One must know that each thermostat is described by different mathematical formulations.

2.4 Initialization

Initialization is the first step in a typical MD simulation. To obtain the trajectory of the particles as a function of time, one must know the initial positions ($\bar{r}_0$) and velocities ($\bar{v}_0$) of the particles in the simulation domain. In general, initial positions are obtained from experimental observations such as crystal structures, theoretical modeling such as MC simulations or randomly distributing to the simulation domain. Then, the positions of the atoms are updated with time evolution to reach a minimum energy state. Furthermore, initial velocities are typically assigned by Maxwell-Boltzmann or Gaussian distribution at a given temperature. Maxwell-Boltzmann distribution predicts the probability (p) of the atom i having velocities of $\bar{v}_{ix}$, $\bar{v}_{iy}$ and $\bar{v}_{iz}$ respectively in the x, y and z-directions at a temperature T as

$$p(\bar{v}_{ix}, \bar{v}_{iy}, \bar{v}_{iz}) = \left(\frac{m_i}{2\pi k_B T}\right)^{2/3} e^{-\frac{m_i(\bar{v}_{ix}^2 + \bar{v}_{iy}^2 + \bar{v}_{iz}^2)}{2k_B T}} \qquad (2.3)$$

where k_B is the Boltzmann constant. Fig. 2.3, shows Maxwell-Boltzmann distribution of molecular speed of atomic species.

Initial velocities are set considering total linear momentum is equal to zero. An ensemble of initial velocities must satisfy the temperature from kinetic energy using

$$T = \langle \frac{1}{3Nk_B} \sum_{i=1}^{N} m_i \bar{v}_i^2 \rangle \qquad (2.4)$$

2.5 Empirical Potential Functions in MD simulations

The accuracy of any MD simulation strictly depends on the empirical potential energy functions, which is defined by the interaction parameters specified to model a microscopic system. The derivative of the potential energy function is the molecular
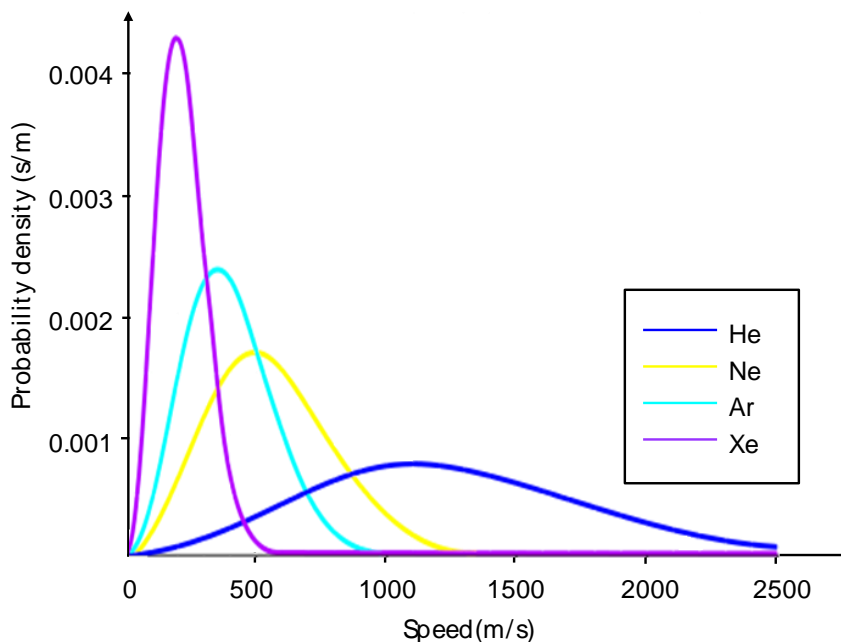
Fig. 2.3 Maxwell-Boltzmann molecular speed distribution of some noble gases at 298 K. Adopted from Maxwell-Boltzmann Distribution in Wikipedia, from https://en.wikipedia.org/wiki/Maxwell-Boltzmann_distribution.[83]

forces between the interacting particles, describing how particles move with time evolution. It is often desirable to use simple models with minimum parameters in simulations because they are easy to implement and they reduce the computational time. Most importantly, the selected force-fields (potential energy function) in MD simulations must well represent real inter/intramolecular forces between interacting atomic species. The general form of force-fields in molecular modelling is described by bonded and non-bonded interactions

$$V_{Total} = V_{Bonded} + V_{Non-bonded} \tag{2.5}$$

The bonded potentials model the internal energy of interacting particles, where it allows stretching, bending and torsion. Intramolecular interactions such as covalent bond is introduced by bonded potentials while the non-bonded term is used to describe distant

interactions such as electrostatic and van der Waals forces. Schematic of the sphere-bond illustration of these interactions is given in Fig. 2.4.
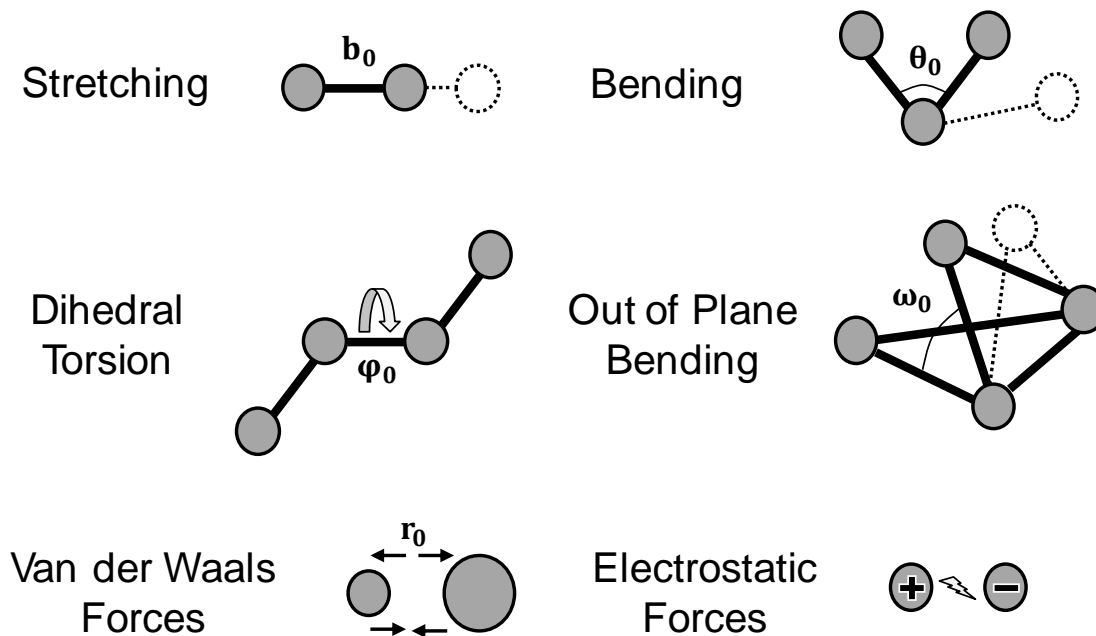
Fig. 2.4 Force-fields in molecular mechanics.

2.5.1 Bonded Potentials

The chemical bonds typically correspond to stretching along the bonds, bending between the bonds and twisting around the bonds. The work done by the molecular or external forces acting on the bonds manifests itself as elastic strain energy, where one can consider atoms as spheres and bonds as springs. The mathematics of spring deformation is used to describe bond stretching, bending and torsion. Stretching refers to length change in the covalent bond while simple bending is related to planar angle change. Furthermore, dihedral torsion term represents the twisting motion of a covalent bond around the bond axis, while out-of-plane bending reflects non-planar bending motion. The mathematical form of the energy terms for bonded interactions are given as

$$V_{Bonded} = V_r + V_\theta + V_\varphi + V_\omega \qquad (2.6)$$

where V_r is the bond stretching energy, V_θ is the bond angle bending energy, V_φ is the dihedral angle torsion energy, V_ω is the out of plane torsion energy.

$$V_{Bonded} = \sum_{Bond} k_b (b - b_0)^2 + \sum_{Angle} k_\theta (\theta - \theta_0)^2$$
$$+ \sum_{Dihedral} k_\varphi (1 + \cos(\varphi + \varphi_0))^2 + \sum_{Improper} k_\omega (\omega - \omega_0)^2 \qquad (2.7)$$

in the above, k_b, k_θ, k_φ and k_ω are the force constants for bond stretching stiffness, angle bending, dihedral torsion and out of plane torsion, respectively. The force constants are often obtained from experiments (infrared frequencies) or quantum mechanical calculations. In the equation, b_0, θ_0, φ_0 and ω_0 denote the initial bond lengths and angles while b,θ, φ and ω denote the values after deformation. These bond quantities can be evaluated from high resolution crystal structure or microwave spectroscopy data. In literature, different force fields are designed for modelling of different materials. For example, AMBER and CHARM are popular force fields used for larger molecules such as proteins and polymers[84-85]. MM2 is designed for hydrocarbons[86]. SPC/E, TIP3P and TIP4P/2005 are some of the force-field models for water molecules[87]. The adaptive intermolecular reactive empirical bond-order (AIREBO) is introduced to model potential energy function of carbon based structures such as graphene and carbon nanotubes[88-89].

2.5.2 Non-bonded Potentials

Non-bonded interactions are described by van der Waals and electrostatic forces, which are relatively weaker forces when compared to intramolecular forces such as

covalent bonds. The general form of the potential energy for non-bonded interactions is given by

$$V_{Non-bonded} = V_{vdW} + V_{electrostatic} \qquad (2.8)$$

where V_{vdW} is the van der Waals interaction potential and $V_{electrostatic}$ is the electrostatic interaction term. Traditionally, Lennard-Jones (LJ) potential is used to mimic van der Waals interactions while Coulomb potential is used to introduce electrostatic interactions. In addition, both terms can be buffered or scaled by a constant factor to account for electronic polarizability and produce better agreement with experimental observations.

LJ potential is assumed as one of the most accurate intermolecular potential for simple liquids based on the balance of repulsive and attractive forces. LJ potential simultaneously considers the difference between short-range repulsion forces and long-range attractive (dispersion) forces that occur at larger separations. This potential is given by the following equation

$$V_{LJ}(r_{ij}) = 4\varepsilon \left[\left(\frac{\sigma_{ij}}{r_{ij}} \right)^{12} - \left(\frac{\sigma_{ij}}{r_{ij}} \right)^{6} \right] \qquad (2.9)$$

where r_{ij} is the separation distance between two atoms or molecules, ε is well-depth of the potential well which measures how strongly the two particles attract each other and σ_{ij} is the molecular diameters, showing the distance where intermolecular potential is zero. In this equation, the first term represents steep repulsive short-range behavior (Pauli repulsion) while second term is the smoother attractive force effective in the long range (London Dispersion). Potential distribution of a typical LJ model as a function of intermolecular distance is illustrated in Fig. 2.5.

- The deeper ε means stronger interaction of two particles.
- The potential energy becomes zero when the intermolecular distance is equal to σ.
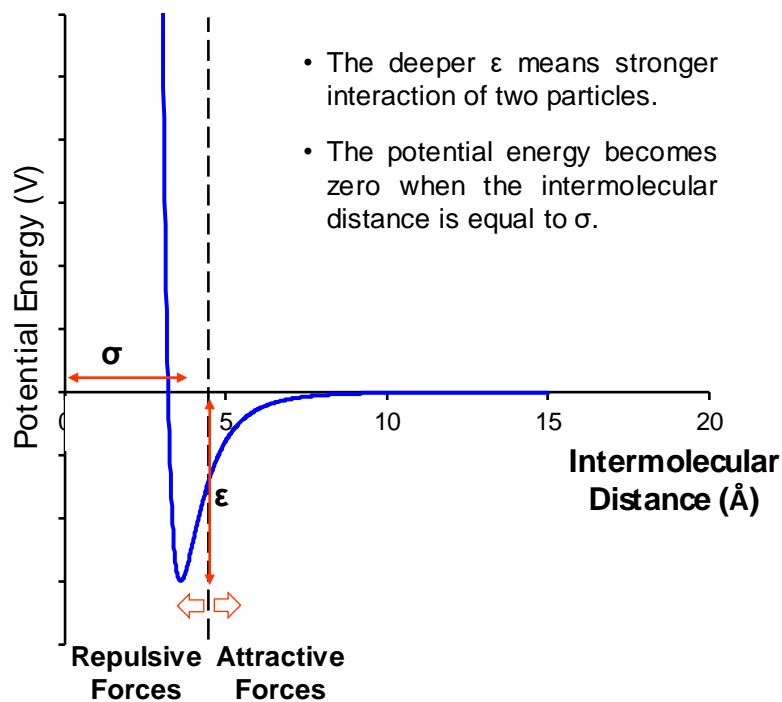
Fig. 2.5 LJ potential as a function of intermolecular distance.

Considering two atoms in an infinite distance, interatomic potential between these particles is zero. When the two atoms are brought closer, they start interacting and the attractive forces are dominant to get the particles together. The distance between the atoms continuously decrease until the potential energy reaches a minimum. At this point, additional energy is needed to bring the atoms closer where repulsive forces are dominant. At a couple of molecular distance, intermolecular potential converges to zero (Please see Fig. 2.5). Therefore, a certain cut-off radius (r_c) is considered to exclude the interactions at large distances to reduce the computational cost. For LJ potentials, it is customary to use a cut-off distance of 1.1nm, which is approximately equal to 3σ[90]. Using a larger cut-off distance does not affect the density predictions for LJ fluids. However, long-range attractive LJ interactions are crucial for accurate calculations of dense gas and liquid pressure[82]. Truncating cut-off the LJ potential results in a

discontinuity in energy conservation and atomic motion. To prevent this jump, LJ potential is shifted upwards, making intermolecular potential equal to zero at the specified cut-off distance. Beyond this distance, the potential energy contribution is considered as zero. The shifted L-J potential function is denoted by

$$V_{LJ}(r_{ij}) = 4\varepsilon \left[\left\{ \left(\frac{\sigma_{ij}}{r_{ij}}\right)^{12} - \left(\frac{\sigma_{ij}}{r_{ij}}\right)^{6} \right\} - \left\{ \left(\frac{\sigma_{ij}}{r_c}\right)^{12} - \left(\frac{\sigma_{ij}}{r_c}\right)^{6} \right\} \right]$$ (2.10)

In the presence of charged particles, electrostatic forces must be taken into consideration in addition to the van der Waals forces. If the charges have the same sign (e.g., two positive or two negative ions), the interaction force is repulsive while it is attractive force when the charged particles have opposite signs. The Coulomb potential accounts for the electrostatic interactions given by

$$V_{Electrostatic}(r_{ij}) = \frac{1}{4\pi\epsilon_0} \sum_{i}^{a} \sum_{j}^{b} \frac{q_i q_j}{r_{ij}}$$ (2.11)

where ϵ_0 is the dielectric constant for vacuum, q_i values are the partial charges, r_{ij} is the distance between two charged pair. The potential energy distribution with intermolecular distance of Coulomb potential is different than that of LJ potential. Typical distribution of Coulomb potential is shown in Fig. 2.6.

Electrostatic interactions are effective in very long range compared to the LJ potential. Neighboring molecules would actually eliminate the effect of the potential at large systems. However, this could happen at several tens or hundreds of nanometers while typical simulation domains are on the order of nanometers.[91] To account for long range interactions of interacting charged particles in systems, one must consider the effect of the periodic images. However, summation of long-range potential for infinite
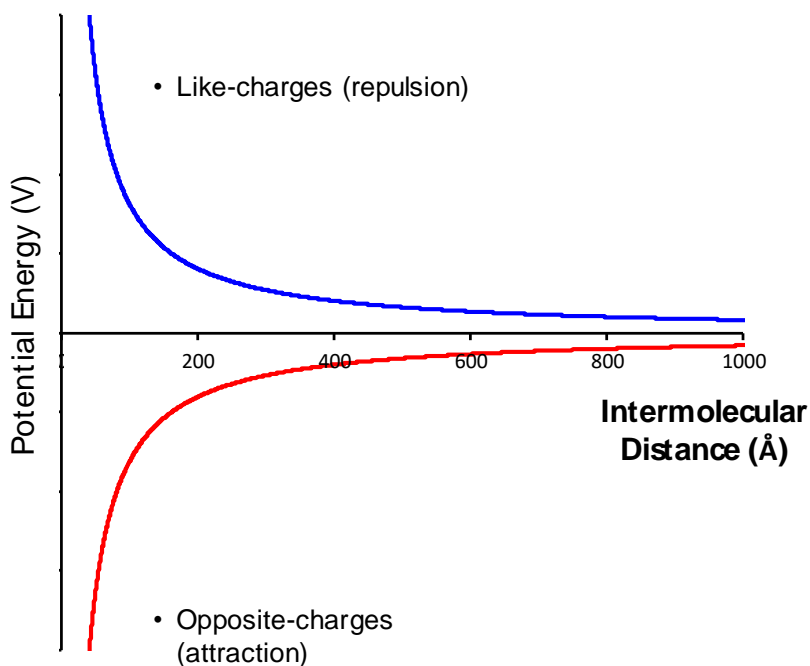
Fig. 2.6 Coulomb potential as a function of intermolecular distance.

neighboring atoms and periodic images are not convergent. This problem can be handled reasonably using a long-range solver by Ewald summation algorithms. In Ewald method, the long-range interaction is divided into two parts: a short-range and a long-range contribution which does not have a singularity. The short-range contribution is computed in real space, but the long-range contribution is calculated using a Fourier transform in periodic images. First, each charge in a simulation system is surrounded by equally but oppositely signed charge distribution. This artificial charge cloud typically follows a Gaussian distribution. Screening the original charges with counter charges makes the potential short-ranged and then computed in real space. Subsequently, another imaginary charge distribution of opposite sign to the first (and of the same sign as the point charges) is presented to eliminate the initially conducted screening charge, where this is summed in reciprocal space[91]. Fourier transform becomes rapidly convergent as this smooth

screening function. There are also two further terms in the Ewald method. Self-term is to diminish the interaction between a point charge and its own screening distribution. Second, surface-term considers the dipolar layer that appears at the surface of a sphere in a vacuum[91]. Ewald algorithms in conjunction with periodic boundary conditions adequately approximate the electrostatic interaction for neutral systems, while it is not applicable for systems with net charge. For such cases, artificial counter charges are added to neutralize the domain which may cause an unphysical behavior.

Calculation of the intermolecular forces between atomic species is computationally the most expensive part of an MD simulation. The use of cut-off in LJ potential significantly reduces the number of interacting particles. Otherwise, calculating the pair potential of particles outside the cut-off distance would be wasteful. To address this, link cell method can be utilized to construct the list of pairs needed to be considered in force calculations[90]. In this method, the simulation domain is divided into small identical cells which are at least one cut-off distance long in all directions, creating the list of molecules inside each cell. Link cell method is applicable to compute the short-range non-bonded interactions (i.e LJ potential), as well as short-range part of the electrostatic interaction when using Ewald summation algorithm.

In general, the potential energy of a system of total N interacting particles is given by

$$V_{Total} = \sum_{I} V_1(r_i) + \sum_{I} \sum_{j>i} V_2(r_i, r_j) + \sum_{I} \sum_{j>i} \sum_{k>j>i} V_3(r_i, r_j, r_k) + \ldots \qquad (2.12)$$

where V_1 is the potential energy due to external felds such as electric field and external force. As second term (V_2) computes the pairwise potential energy while the thirdterm

(V_3) is the potential energy of the triplets. Typically, higher-order interactions are neglected. The gradient of the total potential energy between interacting particle and energy due to external effects give the interatomic force on an individual atom in the system. Then, Newton's equation of motion is integrated at each timestep to obtain new velocities and positions.

2.6 Integrating Equations of Motion

Molecular dynamics method is based on the Newton's second law or the equation of motion, where a force ($\bar{F}$) exerted on a system/particle is related to its mass (m) and its acceleration ($\bar{a}$) with the following well-known formula

$$\bar{F} = m \cdot \bar{a} \tag{2.13}$$

In molecular systems, the atoms interact by exerting forces on each other. Based on the force ($\bar{F}_i$) on each particle, acceleration of the atoms can be determined. Then, integrating of the equation of motion as a function of time alters the positions ($\bar{r}_i$), velocities ($\bar{v}_i$) and accelerations ($\bar{a}_i$) of the particles. Once the positions and velocities are known, the state of the system can be predicted for any time and the average macroscopic quantities are calculated using the trajectory of position and velocities. The forces on the atomic species are expressed as the gradient of the potential energy function given by

$$\bar{F}_i = -\nabla V(\bar{r}_i) \tag{2.14}$$

where $V(\bar{r}_i)$ is the potential energy. Relating equations of motion to the derivative of the potential energy function as

$$\frac{dV(\bar{r}_i)}{d\bar{r}_i} = -m_i \frac{d^2\bar{r}_i}{dt^2} \tag{2.15}$$

Total energy (E_{Total}) of the particle is the sum of kinetic ($E_{Kinetic}$) and potential energy contributions (Hamiltonian formulation).

$$E_{Total} = E_{Kinetic} + V(\bar{r}_i) = \frac{1}{2} m_i \bar{v}_i^2 + V(\bar{r}_i) \tag{2.16}$$

Hamiltonian of the system represents the total potential energy as a function of positions and momenta ($\bar{p}_i = m_i \bar{v}_i$) given by

$$H(r,p) = \frac{|\bar{p}_i|^2}{2m} + V(\bar{v}_i) \tag{2.17}$$

The Hamiltonian is a conserved quantity as the particles move, which means total energy is conserved as a function of time.

$$\frac{dE_{Total}}{dt} = 0 = m_i \bar{v}_i \frac{d\bar{v}_i}{dt} + \frac{dV(\bar{r}_i)}{d\bar{r}_i} \frac{d\bar{r}_i}{dt} = m_i \frac{d\bar{r}_i}{dt} \left[-\frac{1}{m_i} \frac{dV(\bar{r}_i)}{d\bar{r}_i} \right] + \frac{dV(\bar{r}_i)}{d\bar{r}_i} \frac{d\bar{r}_i}{dt} \tag{2.18}$$

The kinetic and potential energy can interchange to each other if a particle follows Newton's equation of motions in a conservative force field (spatial derivative of the potential energy). So, Newton's equations in the Hamiltonian formulation are

$$\frac{dH(\bar{r},\bar{p})}{dt} = 0 = \frac{\partial H(\bar{r},\bar{p})}{\partial \bar{r}_i} \cdot \frac{d\bar{r}_i}{dt} + \frac{\partial H(\bar{r},\bar{p})}{\partial \bar{p}_i} \cdot \frac{d\bar{p}_i}{dt} \tag{2.19}$$

Considering a simple case where intermolecular force on between two atoms does not change as a function of time, the equations of motion are time-integrated to calculate the dynamic behavior of the particles. Initially, force exerted on the atoms is calculated by the gradient of the potential energy function as

$$\bar{a} = \bar{a}_{\Delta t} = -\frac{1}{m_i} \frac{dV(\bar{r}_i)}{d\bar{r}_i} \tag{2.20}$$

The force is constant for each time step, resulting in constant acceleration of the particles. To obtain updated values of velocities and positions, one must know the initial

position ($\bar{r}_0$) and velocity ($\bar{v}_0$). The velocities ($\bar{v}_{\Delta t}$) after a specified time interval (Δt) can be found by

$$\bar{v}_{i,\Delta t} = \bar{v}_0 + \bar{a}(\Delta t) \tag{2.21}$$

Similarly, new position ($\bar{r}_{i-\Delta t}$) of the atoms is calculated by

$$\bar{r}_{i,\Delta t} = \frac{1}{2}\bar{a}(\Delta t)^2 + \bar{v}_0(\Delta t) + \bar{r}_0 \tag{2.22}$$

For time evolution, same procedure starting with the force calculation is repeated for given time using different time integration algorithms, which are introduced in MD simulations to simplify integration of the equations of motion.

2.6.1 Time-integration Algorithms

In MD simulations, time-integration algorithms employ finite difference method to integrate the equations of motion. Computationally efficient numerical algorithms allow a long-time step for integration while conserving energy and momentum. Several algorithms have been developed for this purpose such as Verlet, Leap-frog, Beeman's and Velocity Verlet algorithms. In all of these algorithms, the positions, velocities and acceleration fundamentally are derived from Taylor series of expansion.

$$\bar{r}(t + \Delta t) = \bar{r}(t) + \bar{v}(t)\Delta t + \bar{a}(t)\frac{\Delta t^2}{2} + \bar{r}'''(t)\frac{\Delta t^3}{6} + \ldots \tag{2.23}$$

$$\bar{v}(t + \Delta t) = \bar{v}(t) + \bar{a}(t)\Delta t + \bar{v}''(t)\frac{\Delta t^2}{2} + \bar{v}'''(t)\frac{\Delta t^3}{6} + \ldots \tag{2.24}$$

$$\bar{a}(t + \Delta t) = \bar{a}(t) + \bar{a}'(t)\Delta t + \bar{a}''(t)\frac{\Delta t^2}{2} + \bar{a}'''(t)\frac{\Delta t^3}{6} + \ldots \tag{2.25}$$

"Verlet algorithm" is the most commonly used algorithm in MD simulations, providing a simple, effective, time-reversible and stable method for even large system with considerably low memory and CPU requirement. The Verlet algorithm uses the current positions and accelerations at time t and the backward positions from time t-Δt to calculate new positions at time t+Δt. The Verlet algorithm uses no explicit velocities.

$$\bar{r}(t + \Delta t) = \bar{r}(t) + \bar{v}(t)\Delta t + \bar{a}(t)\frac{\Delta t^2}{2} + \bar{r}'''(t)\frac{\Delta t^3}{6} + O(\Delta t^4) \qquad (2.26)$$

and

$$\bar{r}(t - \Delta t) = \bar{r}(t) - \bar{v}(t)\Delta t + \bar{a}(t)\frac{\Delta t^2}{2} - \bar{r}'''(t)\frac{\Delta t^3}{6} + O(\Delta t^4) \qquad (2.27)$$

where $O(\Delta t^4)$ is the higher-order term. The first and third-order terms from the Taylor expansion cancel out, thus making the Verlet integrator an order more accurate than integration by simple Taylor expansion alone. Adding these two expansions, new position is given by

$$\bar{r}(t + \Delta t) = 2\bar{r}(t) - \bar{r}(t + \Delta t) + \bar{a}(t)\Delta t^2 \qquad (2.28)$$

The Verlet algorithm does not use velocity to determine a solution to the atomic positions for the next time step. The velocities are approximated using the forward and backward positions as follows

$$\bar{v}(t) = \frac{\bar{r}(t + \Delta t) - \bar{r}(t - \Delta t)}{2\Delta t} + O(\Delta t^3) \qquad (2.29)$$

One disadvantage of the Verlet algorithm is that it requires to store in memory two sets of positions at t and $t - \Delta t$. An alternative approach called "Velocity Verlet" reformulates the expansions to directly use the velocities. This algorithm initially uses the positions, velocities and acceleration at current time to calculate the new positions at $t +$

Δt. Based on the new positions, the accelerations at $t + \Delta t$ are calculated. Then, new velocities are found from current velocity and acceleration and forward acceleration

$$\bar{r}(t + \Delta t) = \bar{r}(t) + \bar{v}(t)\Delta t + \bar{a}(t)\frac{\Delta t^2}{2} + O(\Delta t^3) \qquad (2.30)$$

and

$$\bar{v}(t + \Delta t) = \bar{v}(t) + \frac{1}{2}[\bar{a}(t) + \bar{a}(t + \Delta t)]\Delta t \qquad (2.31)$$

"The Leap-frog" algorithm is a similar algorithm to the Verlet algorithm, but explicitly computes the velocities at half time-step intervals. One significant drawback of this approach is that the velocities are not known at the same time as the positions, creating problems in the calculation of the total energy in time.

$$\bar{v}(t) = \frac{1}{2}\left[\bar{v}\left(t - \frac{1}{2}\Delta t\right) + \bar{v}\left(t + \frac{1}{2}\Delta t\right)\right] + O(\Delta t^2) \qquad (2.32)$$

"Beeman's algorithm" is also similar to Verlet method but provides a more accurate expression for the velocity. This allows a better approximation of energy conservation where it is directly calculated from the velocities. However, it is more complex and computationally expensive.

$$\bar{r}(t + \Delta t) = \bar{r}(t) + \bar{v}(t)\Delta t + \left[\frac{2}{3}\bar{a}(t) + \frac{1}{3}\bar{a}(t - \Delta t)\right]\Delta t^2 + O(\Delta t^4) \qquad (2.33)$$

and velocity is

$$\bar{v}(t + \Delta t) = \bar{v}(t) + \left[\frac{5}{6}\bar{a}(t) + \frac{1}{3}\bar{a}(t + \Delta t) - \frac{1}{6}\bar{a}(t - \Delta t)\right]\Delta t + O(\Delta t^3) \qquad (2.34)$$

2.7 Periodic Boundary Conditions

The number of atomic species in a microscopic system is typically negligible when compared to their counterparts in the macro-world. This finite behavior in the small scale might affect the bulk properties of macroscopic system, where infinitely large number of

atoms is available. Furthermore, simulating massive number of particles is not convenient in terms of computation time and data size. In addition, only small fraction of the particles is located near the boundaries in the presence of a surface (for liquid with solid interactions), where the surface interactions become significant. Thus, it may not be necessary to consider long-range distant atoms from the surface unless surface effects are of particular interest. Periodic boundary conditions (PBCs) is an appropriate approach in addressing these important issues. PBCs use a small part of the infinitely large system to approximate the macroscopic behavior. In PBCs, the particles in the original system are enclosed in a box and then replicated to infinity using rigid translation in all directions. The image particles in the replicated cell move soldiery with their original counterparts. When an atom enters or exits one side of the unit cell, it comes out on the opposite site with identical velocity as shown in Fig. 2.7. Consequently, the total number of atoms in the simulation box is always conserved. PBCs allow calculating short-range interactions of particles within the cutoff distance for original and image cells. For long-range correlations, Ewald summation algorithms are specialized to approximate the interaction of periodic images. It should be noted that three-dimensional periodicity might not be necessary in some cases (i.e. liquids confined in nanochannels), where slab modification can be used to calculate interactions in reduced periodicity. On the other hand, using PBCs requires some restrictions. A sufficiently large simulation domain must be used to avoid any artifacts due to the topology. For a very small domain, an atomic particle may interact with its own image, creating unphysical dynamical behavior of the system.
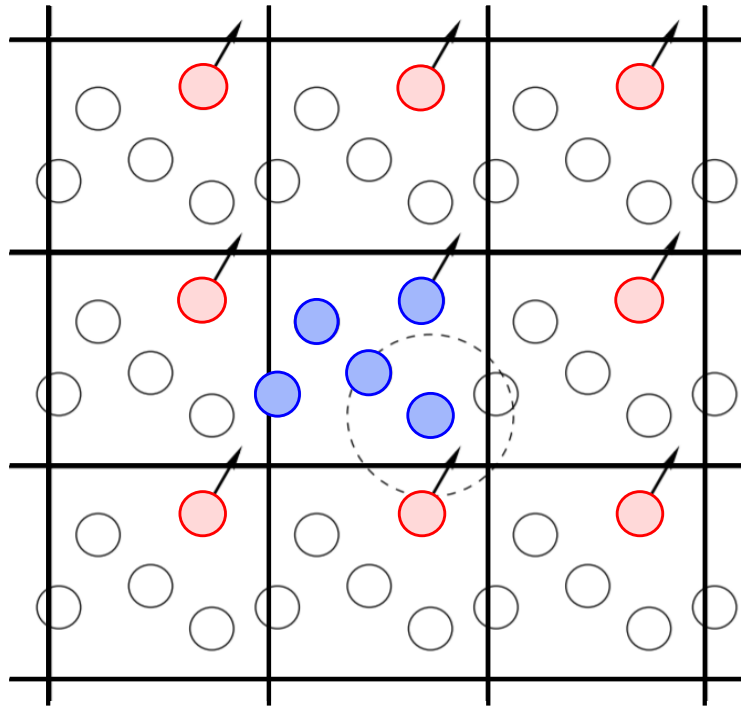
Fig. 2.7 Periodic boundary conditions. An image particle replaces when the original particle moves out of the simulation box

2.8 Data Collecting and Statistical Averaging

For a system having N particles in a typical MD simulation, equations of motion are integrated until properties of the system no longer change as a function of time. Once equilibrium is satisfied, desired properties of the system (e.g., density, pressure, flow rate, temperature, stress) can be directly stored or calculated from the trajectories of particles. Spatial distributions of these relevant properties are generally calculated using "Binning Method"[90]. In this method, the spatial domain is divided into a number of cells which are named as bin. Various binning styles such as slab bin, spherical shell bins or cylindrical bins could be achieved for analyzing different geometries. Each bin may carry different number of particles based on the positions of the particles in the domain, where this result in spatial variety of the properties. In addition, MD simulations are capable of calculating per-atom averages. The relevant properties such as velocity, positions, force, energy,

pressure can be computed and averaged atom by atom for long time-scales. In MD simulations, we are mostly interested in the time averages of physical properties over the system trajectory. One can describe the instantaneous value of a generic physical property of X at time t

$$X(t) = f(\bar{r}_1(t), \bar{r}_2(t) \ldots \bar{r}_n(t) \; ; \; \bar{v}_1(t), \bar{v}_2(t) \ldots \bar{v}_n(t))$$ (2.35)

The average value is given by

$$\langle X(t) \rangle = f = \frac{1}{N_T} \sum_{t=1}^{N_T} X(t)$$ (2.36)

where t is an index parameter which is used for the time steps from initial condition to the total number of steps N_T. The relevant quantity is calculated for each time-step and averaged over the total number of steps. The averaging in each time-step is generally a preferred way where the quantity is particularly important and simple to compute. However, the averaging can also be achieved for every N time-step, when the quantity to be computed is complex and time-consuming. This does not only save in the computational time but also the amount of data stored. Furthermore, the averaged quantities are generally dumped in some periods while the simulation is still running. This approach allows accessing and analyzing the time-evolution data, but it can be very demanding in terms of disk space. To avoid this drawback, the results may be dumped at once or with a limited number of sampling during the simulation, but the same averaging frequency is used. Total averaging time is also another important factor for enhanced statistics in MD simulations. It must be selected long enough to minimize statistical deviations and errors in the related quantities. To assess the statistics in MD simulations, one can quantify the uncertainties using well-known measurement and error analysis. In

this dissertation, we use standard deviation and standard errors for uncertainty analysis. Standard deviation measures how the data spreads out from the mean value. Mean value is the average of the all data sets, where generally conforming normal distribution.

$$x_{avg} = \frac{\sum_1^N x_i}{N} \tag{2.37}$$

in the above, x_{avg} is the mean value, N is the number of data and the x_i is the i th data. Standard deviation (s) is defined as the square-root of the variance (v) which is the arithmetic mean of the squared differences between each value and the mean value. It is given by

$$s = \sqrt{v} = \sqrt{\frac{\sum_1^N (x_i - x_{avg})^2}{N}} \tag{2.38}$$

Low value of standard deviation implies that the data are close to the mean value, while a high standard deviation implies that the data points are largely spread out as shown in the Fig. 2.8.
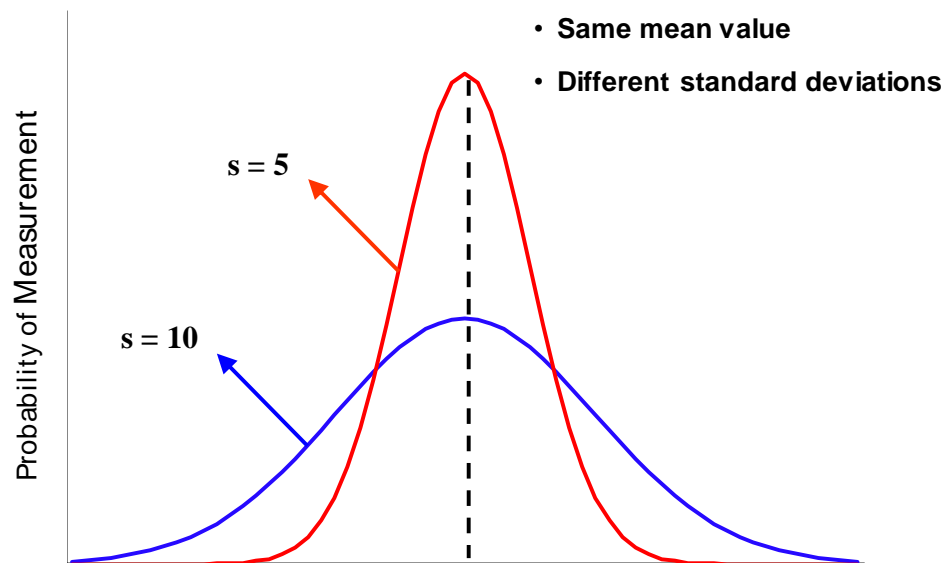
Fig. 2.8 High and low standard deviations.

For quantifying the statistics in large data sets, standard error is a generally used concept, which measures the accuracy of a sampling in a population, calculated by

$$\Delta x_{avg} = \frac{s}{\sqrt{N}} \tag{2.39}$$

where Δx_{avg} is the standard error that reflects how much sampling fluctuation there is in data. As the number of sampling rate increases, the precision in the calculation of statistical uncertainties increases. Following, one can find the final value of measurement as x_m is $x_m = x_{avg} + \Delta x_{avg}$.

Chapter 3

SIZE EFFECT ON HYDRODYNAMIC SLIP LENGTH OF WATER IN CARBON-BASED NANOCONFINEMENTS

3.1 Introduction

Liquid transport in nanochannels is of great importance in the design and fabrication of novel nanofluidic devices for various applications from chemical detection[2] to drug delivery[4], nanofiltration[5] and biosensing[92]. In such applications, the selection of channel material is a key concern in characterization of liquid flow. For instance, carbon-based graphitic nanochannels are exceptionally promising candidates, enabling efficient and superfast water transport owing to their structural properties and hydrophobic nature[93]. Earlier experiments showed that water flow rate through small carbon nanotubes (CNT) is two to five orders-of-magnitudes greater than the predictions of continuum-based no-slip Hagen-Poiseuille's relation[94-95]. Similarly, graphene-based nanochannels also allow fast water flow, which is attributed to smoothness and ultra-low friction of carbon surface[96-97]. Such high flow rates are strongly promoted by the large velocity slip at liquid-wall interface. Thus, an improved understanding of liquid slip behavior can be achieved using molecular level simulations.

High atomic density, smooth surface and weak liquid-solid coupling (low interfacial friction) in carbon-based nanomaterials result in large amount of slip   at the interface. Determination of slip length is critical to gaining of an advanced knowledge of

nano-channel flow characteristics. Multiple computational and experimental studies have been devoted for quantifying the water slip behavior in CNTs and graphene nanochannels. However, there are large variations on the reported slip lengths in the literature both theoretically and experimentally. Several MD simulations predicted the slip length of water in graphene nanochannels about 60 to 80 nm[34, 98-99], while some studies report in the range of 10 to 30 nm [28, 100]. Furthermore, the surface curvature is a prominent factor in determining the slip length of water in carbon nanomaterials, where it leads to discrepancies between reported slip values of CNT and graphene channels at comparable pore sizes[30]. In literature, slip lengths in CNTs were shown to the extent of micrometers to a couple of hundred nanometers, that these results are also significantly dependent to the tube diameter. According to MD simulations[28] and pressure driven water flow experiments in CNTs[101], slip length of water in CNT reduces with the increased tube diameter. However, size-dependency of slip in planar nanochannels is quite controversial. MD-predicted slip lengths in gold nanochannels are found to be constant for channel heights larger than 2 nm[14], while recent experiments showed that slip length of water in graphene nanochannels are scattered in the range of 1-200 nm for different channel heights[102].

Although substantial progress has been made in determination of the slip length in carbon nanochannels, proper characterization of the slip length with a robust calculation method and a meticulous assessment of size-dependency are still required. Our main objective in this study is to systematically examine the nanoconfinement effect in liquid slip flows as well as to acknowledge the limitations of the continuum behavior. Initially, we carry out periodic water domain simulations in the absence of explicit walls to verify

40

the viscosity of adopted water model at a desired thermodynamic state. Then, MD simulations of force driven water flows in planar graphene nanochannels and CNTs are performed at different channel sizes and tube diameters to investigate variations in density distributions, velocity profiles and slip lengths. The slip lengths of water in nanoconfinements are calculated using the average channel velocity profiles between first density peak locations obtained at a fixed thermodynamic state.

3.2 Theoretical Background

Liquid transport in nanochannels can be driven using external means such as pressure[42], electric fields[36], concentration gradients[103] and temperature[104]. In this study, we consider force-driven water flow through uncharged graphene nanochannels and CNTs as illustrated in Fig. 3.1. For incompressible and Newtonian fluid flows, the Navier-Stokes equation is given as

$$\rho\left(\frac{\partial \bar{V}}{\partial t} + (\bar{V} \cdot \nabla)\bar{V}\right) = -\nabla P + \mu\nabla^2\bar{V} + \bar{f}_{ex} \tag{3.1}$$

where $\bar{V}$ is the fluid velocity vector, ∇P is the pressure gradient, μ is the dynamic viscosity of the solution and $\bar{f}_{ex}$ is the external body force. For 1D, steady, incompressible, fully developed and force-driven Newtonian fluid flows, the Navier-Stokes equation is reduced to the following form

$$\frac{d^2u}{dz^2} = -\frac{f}{\mu} \tag{3.2}$$

where $u(z)$, f and μ are the velocity field, driving-force and the fluid viscosity, respectively. First integration of Eq. (3.2) with respect to z gives the velocity gradient,

$$\frac{du}{dz} = -\frac{f}{\mu}(z + C_1) \tag{3.3}$$

Second integration with respect to z gives the velocity profile

$$u(z) = -\frac{f}{\mu}\left(\frac{z^2}{2} + C_1 z + C_2\right) \tag{3.4}$$

We consider a Navier-type slip boundary condition at the liquid solid interface as follows

$$u_s - u_w = \beta \frac{du}{dz} \tag{3.5}$$

where β is the slip length, u_s is the slip velocity and u_w is the wall velocity. Considering constant slip on the walls ($z = 0$ and $z = h$), the velocity profile of an incompressible liquid between two parallel plates with a channel height of h is given by

$$u(z) = \frac{fh^2}{2\mu}\left(-\left(\frac{z}{h}\right)^2 + \left(\frac{z}{h}\right)\right) + \frac{fh\beta}{2\mu} \tag{3.6}$$

For nanotubes, the direction of channel height (z) is replaced by the radial coordinate (r). The velocity profile of an incompressible flow through a cylindrical tube with a radius R is given by

$$u(r) = \frac{fR^2}{4\mu}\left(-\left(\frac{r}{R}\right)^2 + 1\right) + \frac{fR\beta}{2\mu} \tag{3.7}$$

In Eqs (3.6) and (3.7), first term of the right-hand side is related to the parabolic profile of the typical no-slip solution, which is used to determine the liquid viscosity by polynomial curve-fitting[14]. The last term is related to flow enhancement due to slip, which is used to obtain the slip length in parabolic velocity profiles. The slip length normalized by the channel height ($\beta^* = \beta/h$) or CNT radius ($\beta^* = \beta/R$) plays an important role on the shape of the velocity profile. The focal length (distance between the vertex and the focus) of the parabola increases with increased β^*, and results in

increasingly flattened and ultimately "plug like" velocity profiles. For such cases, we relate the wall shear (τ_w) to the total body force applied on liquid molecules using conservation of linear momentum in the flow direction[18, 33]. Then, we combine this relation with the Navier-type slip in Eq. (3.5) and the constitutive equation for shear stress for Newtonian fluids ($\tau_w = \mu \frac{du}{dz}$) to obtain the following relations for slip length

$$\beta = \begin{cases} \dfrac{2\mu u_s}{fh} \approx \dfrac{2\mu \bar{u}}{fh}, & plug-like\ flow\ in\ paralel\ plates \\[2ex] \dfrac{2\mu u_s}{fR} \approx \dfrac{2\mu \bar{u}}{fR}, & plug-like\ flow\ in\ tubes \end{cases} \tag{3.8}$$

in the equations above, u_s is the slip velocity and $\bar{u}$ is the channel averaged velocity. It is important to indicate that the slip velocity is practically equal to the average velocity for plug-like flows[30]. In addition, bulk viscosity of the liquid (μ) is also crucial for defining the slip length.
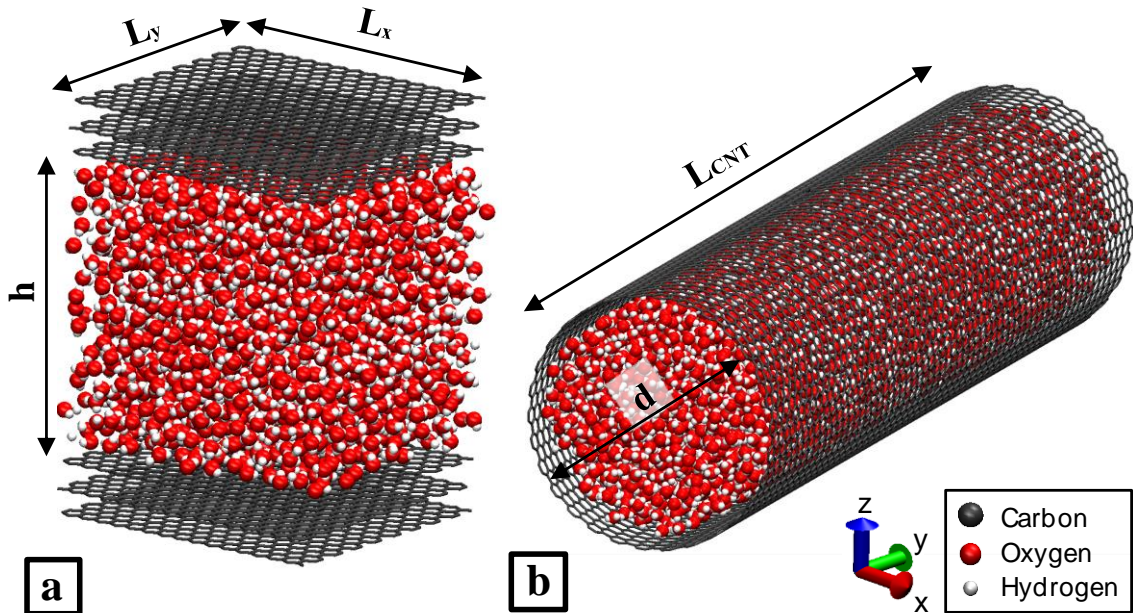
Fig. 3.1 Schematic representation of the simulation domains (a) Planar graphene nanochannel and (b) CNT.

3.3 Molecular Dynamics Simulation Details

Nonequilibrium MD simulations were performed using LAMMPS (Large Scale Atomic/Molecular Massively Parallel Simulator)[105]. Lennard-Jones (LJ) potential was used to model van der Waals forces between the atoms, while Coulomb potential was used for electrostatic interactions of charged sites, given by

$$\emptyset(r_{ij}) = 4\varepsilon \left[\left(\frac{\sigma_{ij}}{r_{ij}} \right)^{12} - \left(\frac{\sigma_{ij}}{r_{ij}} \right)^{6} \right] + \frac{1}{4\pi\epsilon_0} \sum_{i}^{a} \sum_{j}^{b} \frac{q_i q_j}{r_{ij}} \qquad (3.9)$$

where ε and σ are the well-depth and molecular distance, respectively. ϵ_0 is the vacuum permittivity, q_i values are the atomic charges, r_{ij} is the distance between atoms or charged particles. Water interactions were described using rigid, four-site TIP4P/2005 model due to its good predictions of bulk viscosity of water. We carried out force-driven flow simulation of water in a periodic box without any physical boundaries to verify model's performance[53, 106]. Angles and bond length were constrained using SHAKE algorithm[107]. Interactions between carbon atoms and liquid molecules were described based on experimental contact angle study of Werder *et al.*[108] Carbon walls were fixed at their original positions and their interactions were excluded to maintain a cold wall behavior. No charges were assigned on the carbon atoms to represent an electrically neutral wall, but hydrogens and oxygens in water molecules carry partial charges. The long-range electrostatic interactions of charged particles were computed using the particle-particle-particle-mesh (PPPM) algorithm with a root-mean-accuracy of 10^{-5} [109]. The specified accuracy describes the relative root-mean-square error in per-atom force that is explicitly computed by the long-range algorithm. The reference value is selected as representative of the magnitude of electrostatic forces in the simulation domain[110]. An

accuracy value of 10^{-5} indicates that the reference force is 100,000 greater than the root-mean-square error[110]. Short-range interactions were smoothly truncated with a 1 nm cut-off distance. Table 3.1 presents potential parameters of all atomic species. In this study, each simulation begins with a thermal equilibrium using Canonical (NVT) ensemble before subjecting any external driving-force on liquid domain. To establish this, initial velocities of each water molecule were randomly assigned using Gaussian distribution at a specified temperature. The thermodynamic state was fixed by maintaining the temperature of water at 300 K using Nose-Hoover thermostat and keeping the bulk density of water at 997 kg/m^3. The systems were run for 2 ns to reach an equilibrium state. Starting from the equilibrium conditions, force-driven water flow simulations were carried out. The flow was driven by externally applied force on each water molecule in the stream-wise direction. Steady state response was achieved by initially running the system for 1 ns, then an additional 16 ns was performed for data collection and statistical averaging. The time scale to reach steady solution was determined using time for momentum diffusion ($t_D = l^2/v$), where v is the kinematic viscosity and l is either the channel height or CNT radius. All simulations are run with 1 fs time steps using Verlet integration scheme. Periodic boundary conditions were used in the flow direction. Planar and cylindrical binning were applied using 1000 slab-bins to properly resolve the wall-liquid interface. The bin size is fine enough to catch the details at the interface and large enough to prevent losing statistics.

3.4 Force-Driven Water Flow Simulation in Periodic Domain

Fluid viscosity is critical for accurate characterization of slip in nanoscale confinements. Many force-fields have been introduced for molecular simulation of water,

Table 3.1 Potential parameters for atomic species

Atom Pair	σ (nm)	ε (kj/mol)	q (e)
H – H	0	0	0.5564
O - O	0.31589	0.7749	-1.1128 (dummy)
C - O	0.3190	0.3921	0

differing in interaction parameters, the number of charged sites, their flexibility/rigidity and polarizability. Considering the classical water models, TIP4P/2005 offers an impressive performance in reproducing viscosity of bulk water in a wide range of temperatures[47-49]. To verify the viscosity of TIP4P/2005, we perform force-driven flow simulations of periodic water domain in the absence of explicit boundaries for varying domain sizes[53]. First, periodic box is spatially divided into two identical subdomains and equal body forces are applied on each subdomain in opposing directions. This results in two counter flowing parabolic velocity profiles at periodic sides of the domain with zero velocity (i.e., no-slip) at the domain center. Fig 3.2 shows the velocity profiles for two counter flows obtained in a periodic domain of 2h=95.2 Å. Next, velocity the profiles on each subdomain are fitted to a second-order polynomial in the form of $u(z) = Az^2 + Bz + C$, where the viscosity is found by comparing the coefficients of the fitted equations (parameters A and B) with the continuum flow model given by Eq. (3.3) assuming no-slip ($\beta = 0$). We calculate four different viscosity values following the methodology in Ghorbanian and Beskok[14]. Viscosities of μ_1 and μ_2 are calculated using the coefficients of A for each counter flow velocity fit by $\mu = -f/2A$, while μ_3 and μ_4 are calculated using the coefficients of B for each counter flow velocity fit by $\mu = -fh/2B$. Finally,

their average is used for comparison with the thermodynamic viscosity (μ_{TD}=853 μPa.s) of water at T=300 K and ρ=997 kg/m^3.
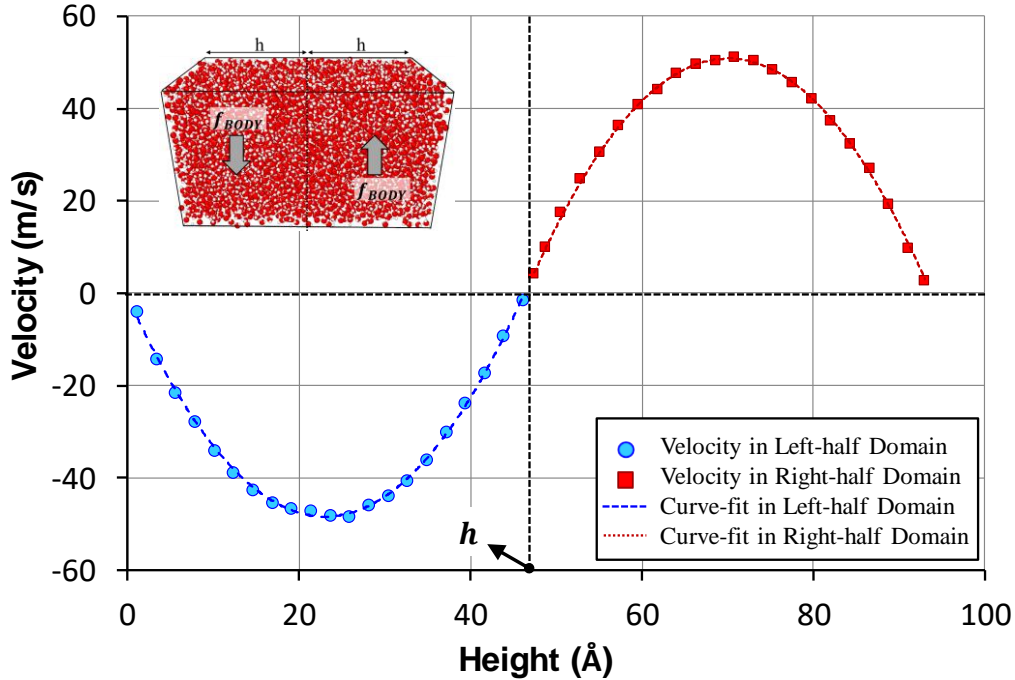
Fig. 3.2 Force-driven counter-flowing of water in a periodic box of 2h=95.2 Å.

In Table 3.2, the viscosity results of counter-flowing force-driven periodic water domain simulations are presented as a function of the domain size. Comparison of the thermodynamic viscosity value and MD-predicted average water viscosity shows a maximum error of 4.4% in the smallest domain, which is consistent with[14]. Our viscosity values are also in good agreement with the values reported for TIP4P/2005 water model in previous MD studies [48]. Clearly, periodic box simulation results assure the reliability of adopted water model for calculating the apparent viscosity in periodic domains as small as 1.7 nm.

Multiple reports showed that bulk properties of liquids in nanoscale confinements are still observable for channel heights of 2-2.5 nm[41, 45, 54, 111]. It should be noted that the

height of graphene nanochannels in our simulations is much larger than these values (approximately 4 nm), so that the confinement effect on apparent viscosity of TIP4P/2005 water model is insignificant. For narrower channel (size smaller than fives molecular diameters), confinement effect becomes very important, where liquid viscosity is significantly larger than the bulk value[44]. Aluru and Suk also demonstrated that the apparent viscosity of water in CNTs is larger at very small CNT diameters, but it approaches to its bulk value with diameters above 2.5 nm[41]. One main reason of this behavior is the wall effect on the atoms near the wall, which results in density layering that affect overall bulk properties of liquid. Wall force field effects vanish sufficiently far away from the surfaces. Using TIP4P/2005 water model, Markestejin *et al.* carried out Poiseuille flow simulations in 4.3 nm height channel, and show that viscosity of TIP4P/2005 water model correctly captures the thermodynamic value for a wide range of temperatures[54]. As a result of these findings in the literature, apparent viscosity in the slip relation given in Eq. (3.8) can be associated with the viscosity generated by the TIP4P/2005 model, which is nearly equal to the thermodynamic viscosity of water at 300K.

Table 3.2. Viscosity results using polynomial curve-fitting method. Thermodynamic viscosity of water is 853 µPa.s at T=300 K and ρ=997 kg/m^3

h (nm)	μ_1(µPa.s)	μ_2(µPa.s)	μ_3(µPa.s)	μ_4(µPa.s)	μ_{AVE}(µPa.s)	Error (%)
1.70	819.7	823.9	809.5	811.8	816.2	4.4
2.72	833.9	830.8	826.2	825.9	829.2	2.7
4.76	838.6	839.4	824.3	821.1	837.5	2.6
6.80	844.1	842.8	836.5	835.8	839.8	1.5
9.52	842.6	842.1	833.3	832.0	837.5	1.8

3.5. Force-Driven Water Flow Simulations in Nanochannels

Next, force-driven water flow simulations are performed in graphene and CNTs at different sizes. The height of the graphene nanochannels are in the range of 1.94 to 9.52 nm while CNT diameters vary between 1.90 to 9.49 nm. Due to their different sizes, different numbers of water molecules are used for each simulation case. Fig. 3.3(a) shows the density profiles of water in graphene channels for different channel heights. Density profiles show a bulk region near the center of the channel and a layering region near the walls due to the wall force-force field effect[112]. To obtain a fixed thermodynamic state for all channel heights in our simulations, the bulk density of water is kept constant at 997 kg/m^3 and temperature is maintained at 300 K. At a fixed thermodynamic state, average density of liquid in nanoscale confinements is always lower than the desired thermodynamic value since the average density within the density layering region is lower than the bulk value. It is also known that the average density increases with increasing the channel heights. In sufficiently large channels, the effect of density layering becomes very small and average density reaches the specified thermodynamic state. We found that liquid density layering in graphene nanoconfinements is effective for channel heights smaller than 70 nm. Above this length scale, the channel averaged density converges to the thermodynamic state value. Such results are also in good agreement with previous reports[14, 21]. As shown in Fig. 3.3(a), water density in carbon confinements presents three distinct density peaks in all cases and the prominent first peak is located approximately 3.15 Å away from the solid walls. The locations and magnitude of the water density peaks are found independent of the channel size as they are independent from the magnitude of applied force. This is important for fixing the

49
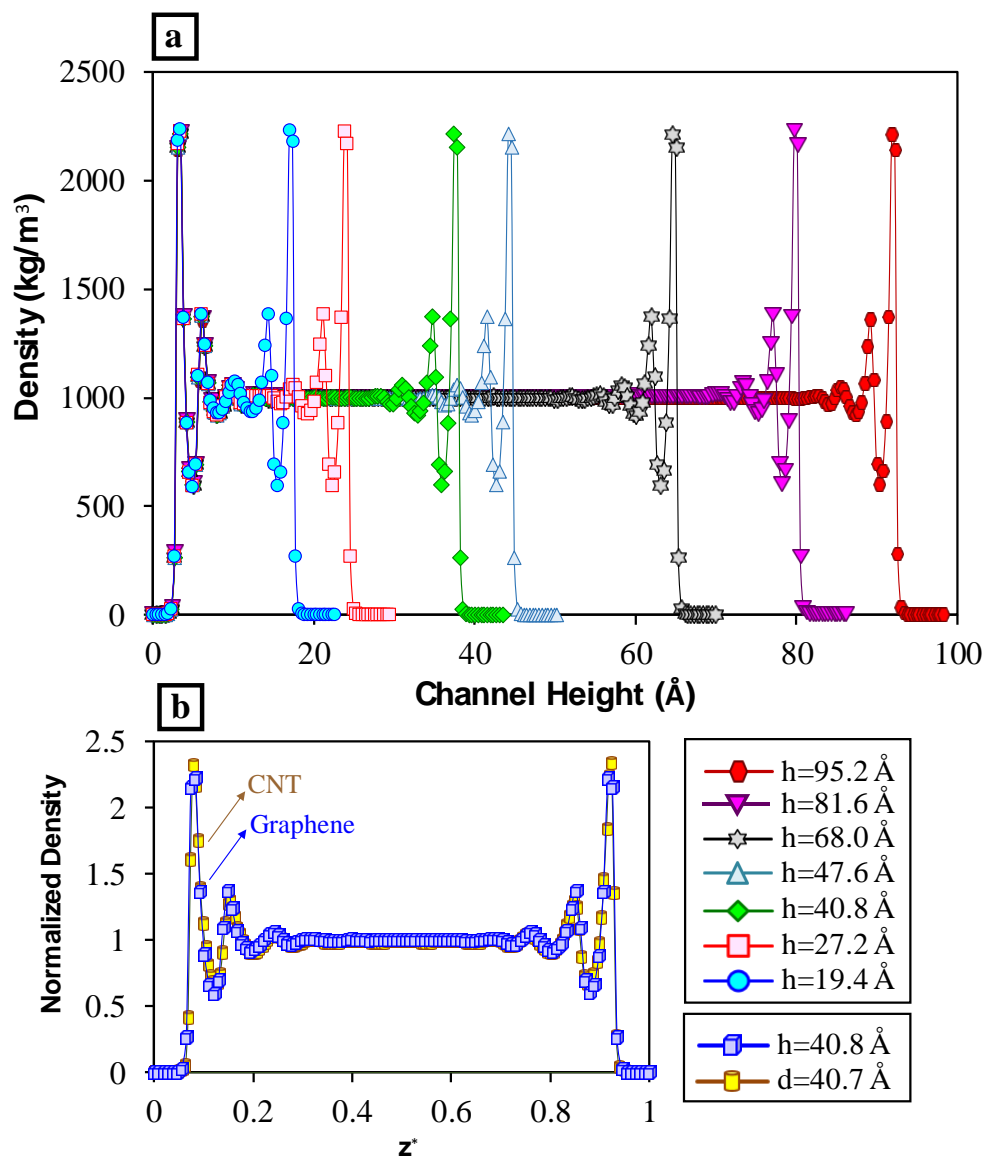
Fig. 3.3 (a) Water density distribution in graphene nanochannels as a function of the channel height (b) Normalized density profiles of water in CNT and Graphene nanoconfinements at similar sizes.

thermodynamic state of very narrow channels, where density fluctuations from both walls interact and make it impossible to observe a bulk region. For such cases, we first explicitly build the density profiles using the layering region of a very large channel at a fixed thermodynamic state. Then, the number of water molecules are estimated based on this explicit density profile. At the end, MD simulations using the specified number of

molecules validates the anticipated density profiles. Current results also agree with the previous studies[23, 113]. In addition, water density profiles in CNTs and graphene nanochannels are similar to each other. In Fig. (3.3b), we compare the density profiles of water in CNT and graphene channels for similar pore size. The density is normalized by the average channel density ($\rho^* = \rho/\rho_{ave}$) while the z-axis is normalized by the channel height and CNT diameter ($z^* = z/h$ or $z^* = z/d$), respectively. The density peaks for both geometries at the same location, but with slight differences in magnitude. This small difference is mainly because planar wall has 3 graphene layers while CNT consist of single layer of carbon surface.

The definition of channel height and the location of the slip plane are critical in quantifying the slip length of water in nanoconfinements. Liquid atoms cannot come close to the solid walls more than a molecular radius[11]. This results in a finite gap (approximately one molecular diameter) between the first water density peak and the wall center locations as shown in Fig. 3.3. Water molecules are concentrated at the first density peak due to the prescribed wall force-field. Therefore, significant variations in velocity profiles and flow rates are observed since this distance is comparable with the nanochannel dimensions. Addressing this, we introduced the concept of an *effective channel height* as $h_e = h - 2L_0$, where L_O is the distance between the wall and the first density peak[18] (Note: effective channel diameter in case of CNT). Most of the liquid molecules are located within this distance. Furthermore, liquid molecules slip on a plane of the first density peak where an apparent fluid region develops, exhibiting finite speed rather than a discrete molecular motion. Therefore, the slip plane is defined at the first mobile density layer near the surface, relating slip lengths on this slip plane (β_{SP}) to that

on the channel wall (β_W) by $\beta_{SP} = \beta_W + L_O$ [18, 23]. In addition, all other physical parameters in Eqs (3.6)-(3.8) are well defined since local thermodynamic state is fixed at prescribed density and temperature[18].

Liquid flows in nanochannels are induced by applying external forces on water molecules. Applied forces are chosen to ensure a linear response between the applied force and the resulting flowrate[114-115]. To establish the linear response regime, we systematically increased the total force and examined the channel averaged velocities. Fig. 3.4 shows variations in the average water velocity in graphene nanochannel (for channel height of 4.76 nm) as a function of the applied force per water molecule. Clearly, non-linear variations in the flowrate begin when the average channel velocities become larger than 50 m/s. It is important to avoid non-linear effects in computations, because it may ultimately result in unphysical and inaccurate transport properties. Kannam *et al.* showed how slip length of an LJ liquid in graphene nanochannels diverges at increased external force fields (or shear rates for Couette flow) while it is constant at lower fields[12]. Furthermore, the minimum flow velocities were selected 25 m/s to reduce thermal noise, that may result in large statistical uncertainties.

In Fig. 3.5a, we present the velocity profiles of water in graphene nanochannels normalized by their average channel velocities at various heights. Independent from the channel heights, all velocity profiles show plug-like flow behavior with large slip velocity at the liquid-solid interface. This is a fundamental result of low friction nature of water flow on graphene surface. Weak interactions between wall atoms and water molecules result in non-wetted liquid system on carbon surfaces, implying large slip lengths[116]. In addition, water velocity profiles in CNTs also present plug-flow behavior
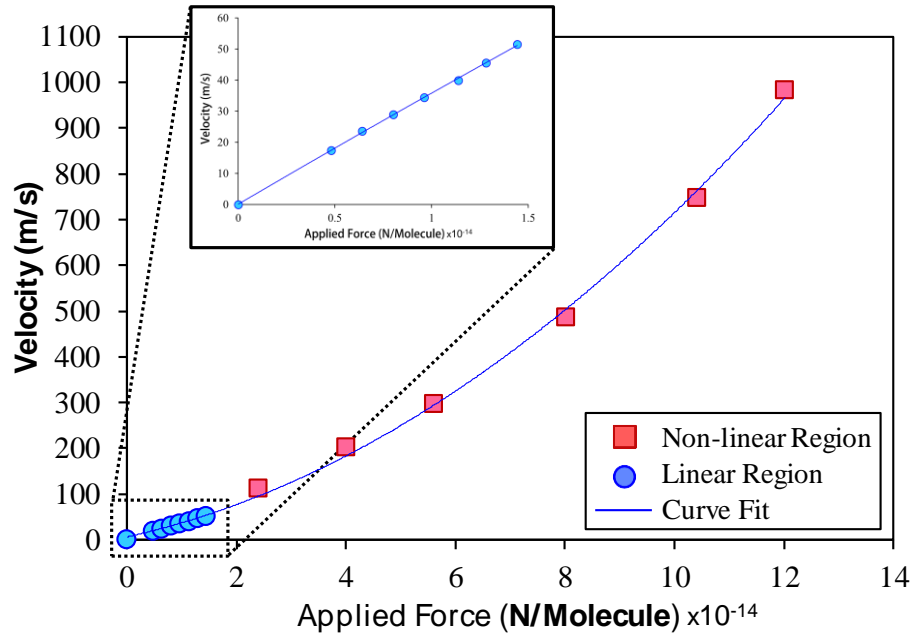
Fig. 3.4 Variations in the average water velocity in graphene nanochannel of 4.76 nm height as a function of the applied driving force.

similar to the flow in graphene channels with large slip near the walls as shown Fig. 3.5b. The plug velocity behavior implies that the average velocity difference is small from the channel center and slip plane, which allows us to use Eq. (3.8) for slip length calculations. A maximum of 2.9% difference is observed between the average velocity and channel center velocity. Although a weak quadratic parabola can be still observable in the velocity profiles, this is mainly deception of scale and statistically insignificant. Kannam *et al*. extensively studied the weak parabolic component in velocity profiles and concluded that polynomial fitting leads to large errors in slip length[34]. Furthermore, a substantial increase in the driving force inverts the velocity profiles much strong quadratic form which is mainly because of the nonlinear effects[12, 34].

Next, we present the results of slip lengths as a function of the channel height and CNT diameter in Table 3.3. To evaluate the slip lengths of water on hydrophobic carbon nanochannels, we used plug-like flow method given in Eq. (3.5), which requires apparent
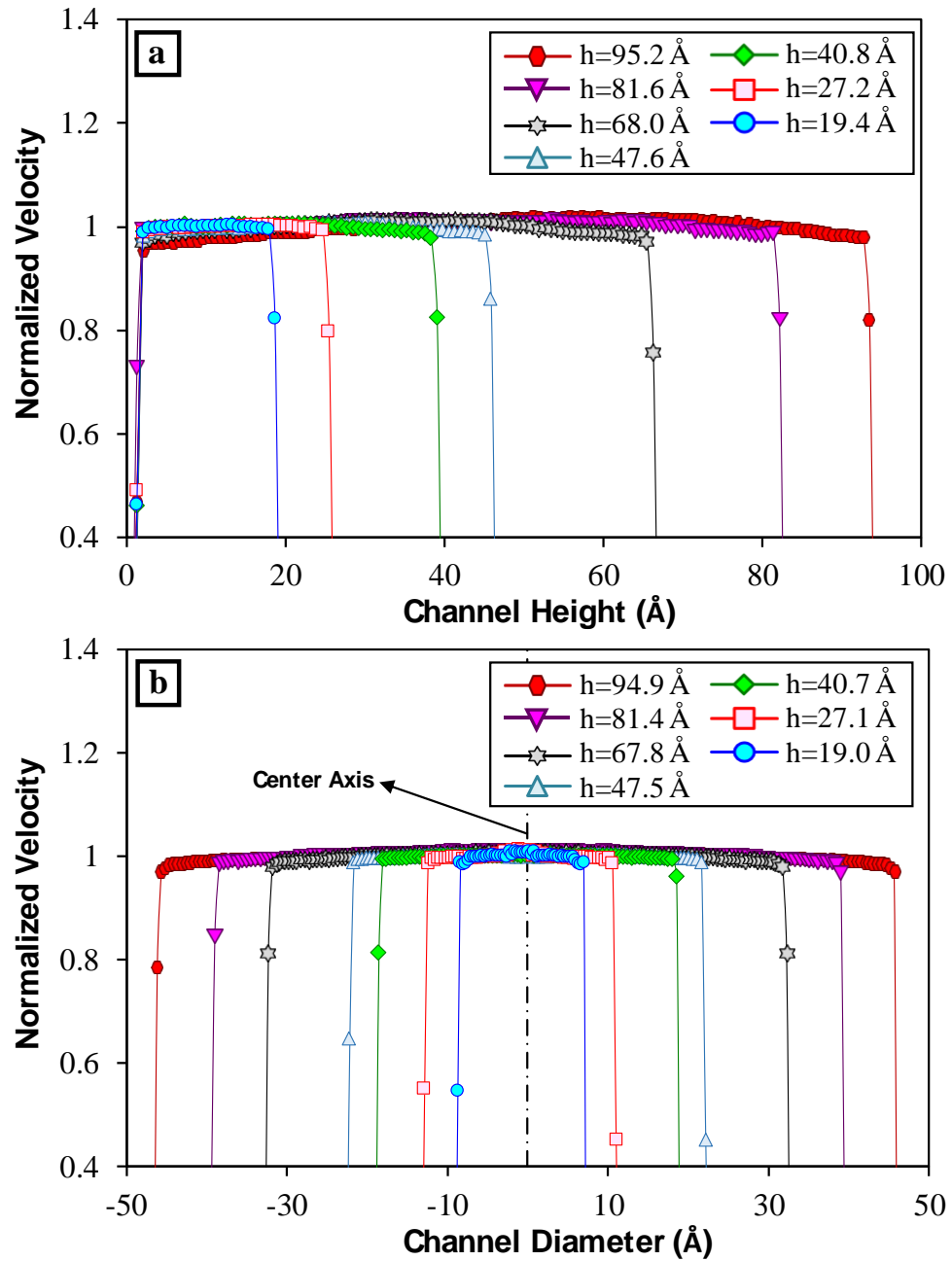
Fig. 3.5 Water velocity profiles normalized by average channel velocities (a) as a function of the graphene nanochannel height and (b) CNT diameter.

viscosity of water when calculating the slip length. We used thermodynamic viscosity of water (μ_{TD}=853 µPa.s), since it is verified by the periodic box simulations as extensively explained earlier. In addition, we used a slip plane located on the first density peak (L_0)

because the velocity profile within L_0 is not well defined due to low liquid density and rapidly reduces to zero. Our MD results show that the slip-behavior is size-independent in graphene nanochannels as small as 2 nm height. We predict the slip length of water on planar graphene walls approximately as 64 nm. This result is consistent with several slip length values previously reported in the literature[12, 34, 98-99]. One can notice that the slip length at the smallest channel height (1.94 nm) was found to be 76 nm using Eq. (3.5). Similarly, several studies in the literature also showed significantly larger slip lengths at narrow channels comparing to larger counterparts[28, 101]. This is mainly related to the definition of the physical variables, such as viscosity at this scale deviates from its thermodynamic value and changes the slip behavior. As pointed out in earlier studies in the literature, the description of the thermodynamic state and bulk properties of liquids like density, velocity and viscosity becomes inaccurate for channels as small as 2-2.5 nm, and liquid molecules present a discrete molecular transport[14, 45, 111]. Therefore, applicability of constitutive equations can be challenged at such scale. Accordingly, the calculation of the slip length based on constitutive equations given in Eq. (3.5) becomes irrelevant. Velocity-slip of water in CNTs present a different behavior compared to that in graphene nanochannels. Curvature effect results in variations in the slip length as a function of the pore size[30]. The slip length values vary between 204.0 and 68.7 for CNTs with diameters of 1.90 to 9.49 nm. A very large slip of water at the interface develops at small diameters while it reduces with increased CNT size. This curvature dependence of slip vanishes for channel diameters beyond 6 nm, which is consistent with the results by Thomas *et* al.[28]. For such cases, the slip length values converge to approximately 68 nm, agreeing with the slip length of water in graphene nanochannels. This behavior is

explained by the weaker solid/liquid coupling strength with increased CNT diameter[28, 117]. At sufficiently large scales, effect of surface curvature on the potential energy landscape becomes insignificant, resulting in smaller slip lengths at interface [28, 117]. A slip value of 204 nm for 2 nm minimum diameter is found using Eq. (3.5) and bulk viscosity, but one must know that apparent viscosity is not well defined at this scale, due to the previously explained reasons.

Table 3.3. Slip length values of water in graphene nanochannels and CNTs at various sizes.

Graphene Channels		Carbon Nanotubes	
h (nm)	β (nm)	d (nm)	β (nm)
9.52	64.2	9.49	68.7
8.16	63.8	8.14	70.8
6.80	63.0	6.78	76.6
4.76	63.1	4.75	90.6
4.08	64.1	4.07	109.5
2.72	65.8	2.71	134.9
1.94	76.4	1.90	204.0

Slip length values of water in Graphene and CNT channels in the present study are within the comparable range of multiple MD studies in the literature[28, 30, 34, 98-101, 118-124]. In Fig 3.6, we summarized the slip length values of water obtained in graphene/CNT membranes for different channel sizes and compared our results with the previously reported MD values. Although similar slip characteristics were observed, there are also important quantitative differences on the slip length values. These significant differences between MD studies are mainly due to the intrinsic algorithmic details such as use of different water models and interaction parameters, neglecting nonlinear flow contribution as well as not properly fixing the thermodynamic state of the simulations. However,
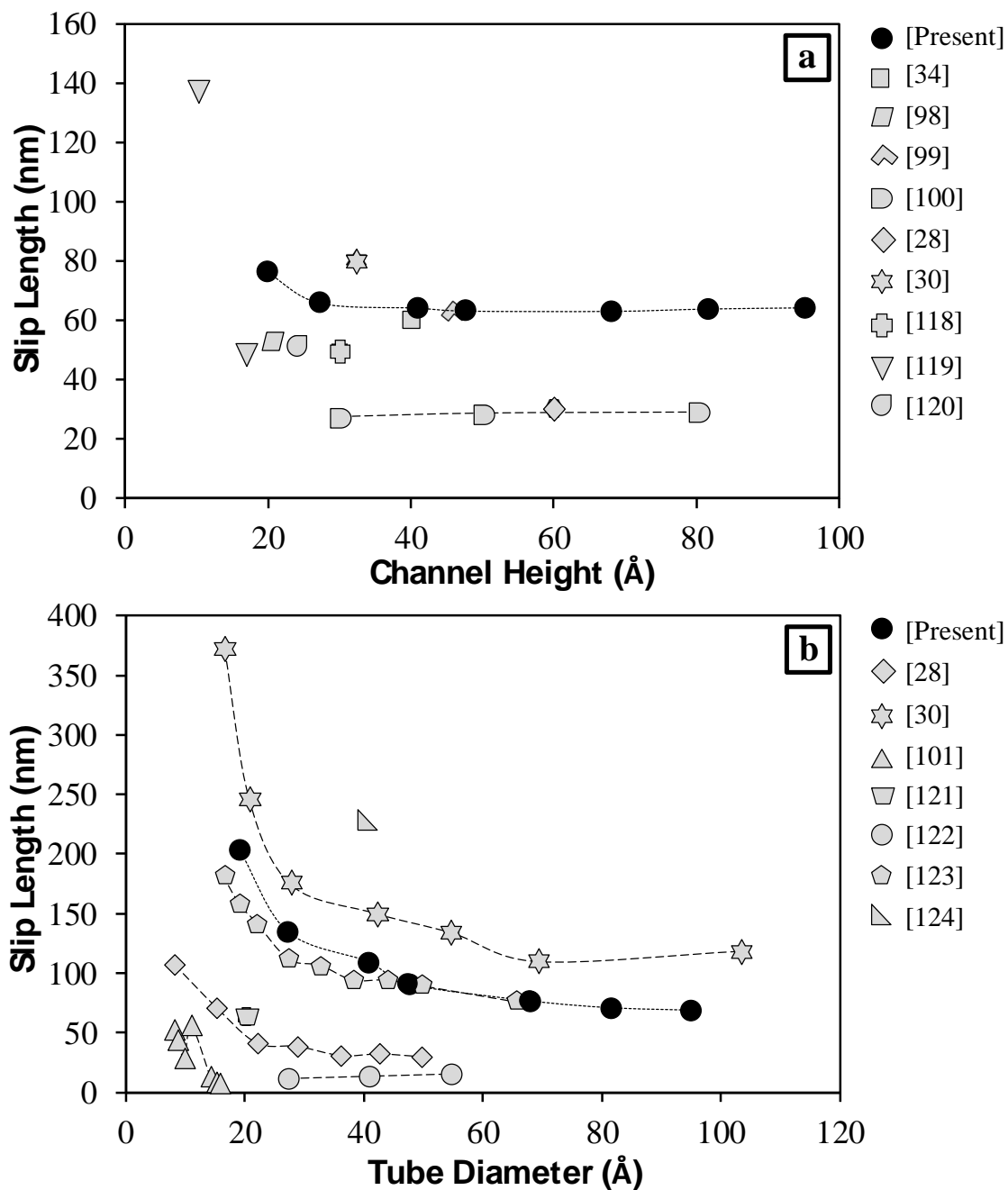
Fig. 3.6 Slip length of water in (a) graphene nanochannels and (b) CNTs as a function of the channel height and tube diameter. Our results (yellow circle) are compared with MD data in the literature.

slip length values based on experiments are much more widely scattered. In earlier

experiments, larger slip of water in CNTs were reported in the range of 1.4 to 54 μm for

different tube diameters, where slip-modified continuum equations (See Eq. (3.6)) are used to reproduce the measured flow rate[94-95, 125]. In a recent study, slip lengths of water in CNTs were found between 300 nm to 15 nm for different tube diameters varying in the range of 15-50 nm, which follows the trend of slip reduction with increased diameter[126]. Their results are comparable with our MD simulations. In graphene nanochannels, latest experiments show a scattered slip data between 0 to 200 nm at various channel heights without any distinct dependence but follows a log normal distribution. Thus, the authors report a median of the slip length as a single value of 16 nm after further statistical analysis[102]. In another study, slip length of water on graphite surface was measured 8 nm[127]. Numerous factors in experiments such as measurement uncertainties, possible imperfections on the graphitic surface, impurities in water, charges on the carbon surface, entrance/exit effects should be considered in comparing experimental data with MD results. However, MD data also have inherent limitations such as accuracy of the used potential energy function, effects of thermostats, and periodic boundary conditions.

3.6. Conclusion

Force-driven water flow through different sized graphene nanochannels and CNTs are investigated using MD simulations. Periodic domain simulations verify the viscosity of water at the adopted thermodynamic state with a maximum error of 4.4%. Liquid viscosity is important on the slip length calculation of the "plug-like" hydrophobic flows, where it is an integral part of the constitutive equation for shear stress for Newtonian fluids. Nanochannel flow simulations are performed at a fixed thermodynamic state in a linear flow regime, which is achieved using force field that create channel averaged

velocities lower than 50 m/s. Obtained by the plug-like velocity profiles, all simulations show large velocity-slip at the interface.

Slip length of water in graphene nanochannels shows size-independency for channel heights larger than 2 nm and it is estimated approximately to be 64 nm. At smaller scales, slip length calculations becomes ambiguous due to discrete molecular liquid flow. In CNTs, a curvature dependent slip behavior is observed. A very large velocity-slip at the interface is developed for CNTs of small diameters, while it drops significantly with increased pore size. Weak liquid-wall coupling strength at small diameters is the main reason of this large slip behavior. For CNTs with diameters larger than 5 nm, slip length converges to 68 nm, showing a good agreement with flat graphene assumption. A slip length of 200 nm is found for the smallest CNT diameter (1.9 nm). For sub-4 nm diameter, MD predicted slip lengths in CNT shows significant differences from that in graphene nanochannels. Current MD slip length results are extensively compared with previous experimental and simulation values and the major reasons of the differences on the slip values are highlighted.

Chapter 4

ELECTRIC FIELD CONTROLLED TRANSPORT OF WATER IN GRAPHENE
NANOCHANNELS

4.1 Introduction

Development of complex nanofluidic systems with pumps, valves and other flow
control elements require enhanced understandings of the structure, dynamics and
transport of nanoscale confined liquids under externally and locally applied fields.
Previous experiences from microfluidic systems can help conceptualize nanofluidic
components. For example, electrowetting has been used in microfluidic systems to guide
and mix droplets using locally applied electric fields[128-129]. Controlling surface wettability
of nanochannels by locally applied electric fields can be used to regulate the flows.
Graphene can be used as local electrodes and varying the electric charges on each
electrode can generate the desired electric field[130-131]. However, such developments
require a good knowledge of nanoconfined liquid flows, which can be achieved using
atomistic simulations.

Liquid transport in nanoscale systems deviates from their micron and larger
counterparts due to the scale and force-field effects[55]. Scale effects become prominent
when the molecular diameter becomes comparable to the dimensions of the flow conduit
so that fluid molecules can no longer be considered as point particles. For example, the
well-known density layering of liquids near the walls is a result of the liquid-wall force

field interactions and the finite size of liquid molecules[112]. These local effects confined to the near-wall region subside within several molecular diameters, and the fluid density reaches a constant bulk value away from the walls[132]. The channel averaged fluid density and apparent-viscosity increasingly deviate from their thermodynamic values with scale reduction[14]. In addition, depending on the surface-liquid interaction strength, liquid may exhibit velocity slip, no-slip or adsorption that greatly affect transport[55]. However, these behaviors must be defined at the first liquid density layer rather than the walls, since the liquid molecules cannot get closer to the walls more than a molecular diameter. For example, fluid slip-plane is at the first mobile density layer near the wall, which affects the apparent channel height[18]. As a result of these effects, predictions of the continuum transport models become inaccurate with decreasing system dimensions, and eventually discrete transport of liquid molecules under the influence of wall force field effects dominates the flow[133].

Molecular dynamics has been used to investigate electro-wetting behavior of nanodroplets on different surfaces. Zhang *et al.*[134] reported enhanced wettability of water molecules on platinum surfaces with increased electric field strengths. Song *et al.*[135] investigated spreading of nanodroplets under electric fields applied parallel to the solid surfaces, and reported decrease of the contact angle and formation of asymmetric droplet shapes. Giovambatistta *et al.*[136] investigated variation of liquid contact angle as a function of locally induced surface charges, and showed reduction in the contact angle with increased electrical charge density. A general trend in the simulations is the enhancement of surface wettability with increased electric fields, where the wetting angle decreases, and the surface becomes more hydrophilic corresponding to stronger liquid-solid

interactions. Polarizable water molecules reorient themselves in the electric field direction[113, 137]. Increasing the electric field magnitude aligns the dipole moments of the water molecules in the system and restricts their degree of freedom, which eventually results in electro-freezing, where the water molecules exhibit high-ordered crystalline structures[138-139]. Svishchev and Kusalik[140] reported a study focusing on crystallization of liquid water on different types of surfaces under applied electric fields. Xia and Berkowitz[141] investigated structural behavior of water molecules confined between oppositely charged platinum walls. At sufficiently high electric fields, water molecules undergo a drastic change and form ice-like ordered structures.

To the best of our knowledge, there is no study investigating the effects of electric field on transport properties of nanoconfined water such as viscosity, density and slip-length. In this study, non-equilibrium molecular dynamics (NEMD) simulations are performed for force-driven water flow through electrically charged graphene nanochannels. The main objective of this study is to elucidate the effect of electric field imposed by oppositely charged surfaces on the structural and transport properties of water confined in graphene nanochannels at a length scale, where the continuum behavior is still observed. We particularly focus on the behavior of deionized water and present results of density profiles, molecular orientations, velocity profiles, viscosities and slip lengths after carefully fixing the thermodynamic state.

4.2 Theoretical Background

Water transport in charged graphene nanochannels may exhibit variations in the slip length and viscosity. To assess such effects, we concentrate on force driven flow between two parallel plates, and review liquid transport using continuum fluid

mechanics. Simplified form of Navier-Stokes equation for a steady, incompressible, fully developed, force-driven Newtonian fluid flow is given in Eq (3.2). In the consideration of constant slip length on the uncharged walls ($\beta = 0 \ at \ z = 0$ and $z = h$), the liquid velocity profile between two parallel plates with a channel height of h was found as in Eq (3.6). However, for channel walls with different charges and signs, the slip length on each wall may be unequal. Slip lengths of β_L on the bottom wall ($z = 0$) and β_R on the top wall ($z = h$) can be rearranged by Navier-type slip condition as follows

$$u(0) = \beta_L \frac{du}{dz}\bigg|_{z=0} \tag{4.1}$$

and (Note that the direction of velocity gradient becomes negative at $z=h$ for a parabolic velocity profile)

$$u(h) = -\beta_R \frac{du}{dz}\bigg|_{z=h} \tag{4.2}$$

At $z=0$, velocity is found using Eqs. (3.3), (3.4) and (4.1) as

$$u(0) = -\frac{f}{\mu} C_2 = \beta_L \left(-\frac{f}{\mu} C_1 \right) \rightarrow C_2 = \beta_L C_1 \tag{4.3}$$

Similarly, velocity at $z=h$ is found using Eqs. (3.3), (3.4) and (4.2) as

$$u(h) = -\beta_R(h + C_1) = \frac{h^2}{2} + C_1 h + C_2 \tag{4.4}$$

Substituting $C_2 = \beta_L C_1$ into Eq. (4.4), a relation between β_L and β_R is obtained as follows

$$-\beta_R h - \frac{h^2}{2} = C_1(h + \beta_L + \beta_R) \tag{4.5}$$

The coefficients of C_1 and C_2 are

$$C_1 = -\frac{h\left(\beta_R + \frac{h}{2}\right)}{h + \beta_L + \beta_R} \quad \text{and} \quad C_2 = -\beta_L \frac{h(\beta_R + \frac{h}{2})}{h + \beta_L + \beta_R} \tag{4.6}$$

Using slip lengths of β_L on the bottom wall ($z = 0$) and β_R on the top wall ($z = h$), the final form of the velocity distribution in the channel is given by

$$u(z) = \frac{f}{\mu}\left(-\frac{z^2}{2} + \frac{h\left(\beta_R + \frac{h}{2}\right)}{h + \beta_L + \beta_R}z + \beta_L\frac{h\left(\beta_R + \frac{h}{2}\right)}{h + \beta_L + \beta_R} \right) \tag{4.7}$$

To calculate the slip lengths and fluid viscosity, a curve fitting method using the velocity profiles obtained from MD simulations are utilized[14, 53]. First a parabolic velocity profile in the form of $u(z) = Az^2 + Bz + C$ is fitted to the MD simulation data, then the A, B and C coefficients are compared with the analytical solution given in Eq. (4.7). Accordingly, fluid viscosity is extracted using

$$\mu = -\frac{f}{2A} \tag{4.8}$$

which is followed by solving for the slip lengths of β_L and β_R analytically using the coefficients B and C.

The polynomial-fit approach provides a good approximation when calculating viscosity and slip-lengths from a parabolic velocity profile. For plug flow, we used conservation of linear momentum in the flow direction as previously explained in Chapter 3, where the slip length is calculated using $\beta = 2\mu\bar{u}/fh$.

4.3 Molecular Dynamics Simulation Details

We carried out molecular dynamics simulations on a three-dimensional model system consisting of water molecules confined between graphitic solid walls. A schematic illustration of the simulation domain is shown in Fig. 4.1. Total dimensions of the domain in the lateral (x and y) and vertical (z) directions were set as 38.13, 36.93 and 54.4 Å, respectively. In the current study, the channel height is h=40.8Å. This dimension

is specifically chosen so that both the continuum behavior and the graphene-water interface phenomena are still observable. Therefore, the simulation domain is large enough to show density layering due to the wall force-field effect as well as a significant bulk region in the middle of channel. For much narrower channels, definition of the thermodynamic state and derivation of continuum variables like density, velocity and viscosity becomes irrelevant and water molecules exhibit discrete molecular transport as previously shown in the literature[28, 45, 111].

Each solid wall contains three defect-free graphene sheets separated by 3.4 Å distance. Graphene wall layers in the walls were organized based on Bernal (ABA) stacking arrangement on XY plane[142]. Wall atoms were constrained at their initial positions representing a cold wall behavior, while remaining particles in the system were free to move. Opposite but equal surface charges were taken into consideration on the bottom and top walls to satisfy the neutrality of the simulation box. Charged surfaces in an electrolyte solution, act as electrodes that attract counter ions, creating electrical double layer (EDL) to shield the surface charge. This phenomenon becomes dominant at high ionic concentration and substantially affects the structure and dynamics of water in nanoscale confinements. Wang *et al.*[143] showed significant differences on the ion and liquid density distributions for a LiClO4-acetonitrile/graphite EDL capacitor at various surface charges. Unlike their study, we focus on the limit of deionized water and neglect any EDL formation on the electrodes.

Intermolecular (van der Waals and electrostatic) forces for all atomic species were described using Lennard-Jones (LJ) and long-range Coulombic as given in Eq. (3.9). Interactions between water molecules were calculated using a rigid four-site TIP4P/2005
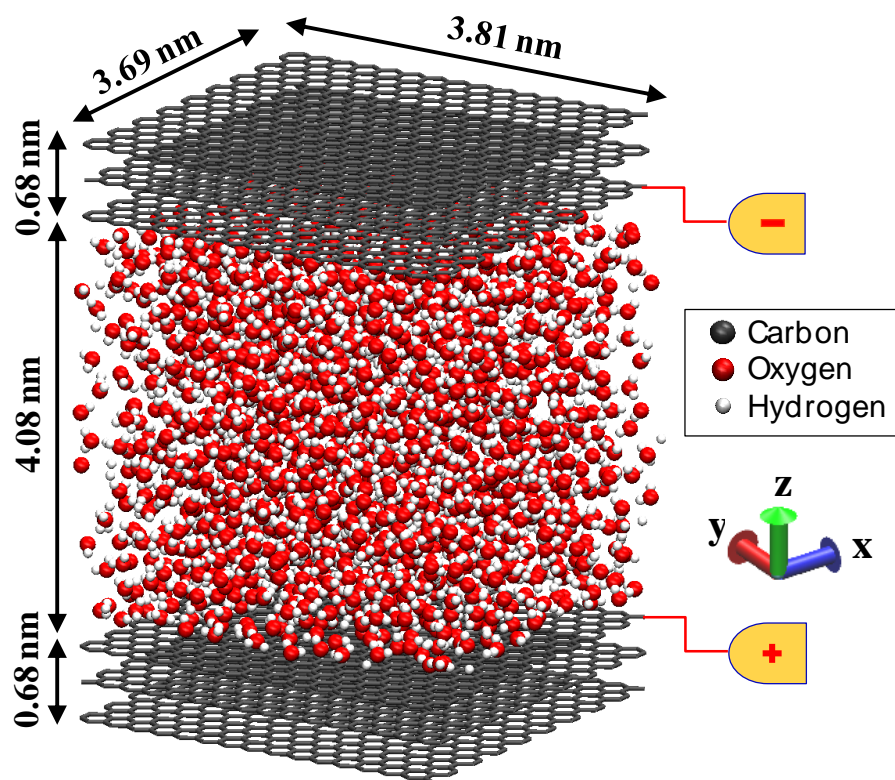
Fig. 4.1 Schematic and dimensions of the simulation domain.

model, which provides a good approximation to reproduce structural and hydrodynamic properties of liquid water in a wide range of temperatures[106, 144]. For this water model, oxygen atoms don't carry partial charges. Instead, a massless negatively charged dummy atom is added along the bisector of the H-O-H bond angle. But neutrality of a water molecule is satisfied by positively charged hydrogen atoms. Bond lengths and angles in water molecules were constrained by SHAKE algorithm in order to make the water molecules rigid[107]. Only oxygen atoms were taken into considerations in our LJ calculations between water-water and water-graphene. Oxygen-carbon interactions were computed using an LJ potential accurately parameterized by experimental observation of water/graphene contact angle by Werder *et al.*[108] Although covalent bonds between carbon atoms can be modeled using interatomic potentials such as AIREBO[88] ,we

excluded these interactions due to the use of the cold-wall model, which eliminates all forces exerted on the carbon atoms. Keeping carbon atoms stationary does not substantially change the structure or dynamics of confined water, but it drastically reduces the computational cost[42, 108]. In addition, electrical charges are imposed on the carbon atoms at the water-graphene interface, while no charge is assigned to the rest. Coulombic interactions between all charged particles are taken into consideration. These long-range electrostatic interactions were handled by engaging particle-particle-particle mesh (P3M) method with a root-mean-accuracy of 10^{-5} [109]. PPPM maps atomic charges to a 3D mesh and enables 3D fast Fourier transform (FFT) to solve Poisson's equation on the mesh. Then, it interpolates electric fields on the mesh points back to the atoms.[90] All short range LJ and Coulombic potentials were smoothly truncated at a cut-off distance of 1 nm. Table 3.1 lists molecular parameters for all atomic pairs used in MD simulations[145].

Large-Scale Atomic/Molecular Massively Parallel Simulator (LAMMPS) was employed in this study[105]. Periodic boundary conditions were used in x- and y-directions. A slab modification in z-direction was activated to calculate the electrostatic interaction for the reduced periodicity[146]. This study simulates well-known Poiseuille flow model between two electrically charged parallel plates to find the transport properties of nanoconfined water. Before we applied any driving-force, we first thermally equilibrated each system in a Canonical (NVT) ensemble. For this purpose, initial velocities on each water molecule were randomly assigned using a Gaussian distribution corresponding to the specified temperature. Initially, the MD system was run for 2 ns using 1 fs time steps for achieving an equilibrium state without any external forces. The thermodynamic state was fixed by maintaining the temperature at 300 K using Nose-Hoover thermostat and

keeping the bulk density of water away from the two graphitic surfaces at 997 kg/m^3. The temperature was calculated from the total kinetic energy, verifying the equilibrium state. Starting from these equilibrium conditions, an external force was applied to conduct the flow simulations. For the flow cases, Nose-Hoover thermostat was applied only to the degrees of freedoms perpendicular to the flow direction. The flow was driven by a constant force in y-direction applied to each atom of the water molecule with respect to their masses. The force for each surface charge density case was carefully chosen to generate velocities lower than 50 m/s. This is important to avoid any non-linear response due to high flow velocity and its dependence on the temperature[114-115]. The linear response regime was verified by comparing the average channel velocities obtained by systematically increasing the driving force (Not shown for brevity). The time scale for momentum diffusion was determined using $t_d \approx h^2/v$, where v is the kinematic viscosity and h is the channel height[14]. We ensured reaching the steady state by initially running the system for 2 ns, which corresponds to $12.5 t_d$. Afterwards we ran and time averaged results for an additional 16 ns for data collection and statistical averaging, creating 1600 independent time-averaged data sets. In order to calculate the standard deviation and standard error, we used 20 independent samples obtained from averaging of 80 consecutive data sets. The domain was divided into 1200 bins in the z-direction to monitor the results. This number of slab-bins was determined, so that the density distribution did not display any qualitative and quantitative differences, enabling proper resolution of the wall-liquid interface.

4.4 Results

In this section, we first examine the density profiles and molecular orientations obtained in MD simulations under zero and varying electric charges. This is followed by investigations of the velocity profiles, slip lengths and viscosity variations for force-driven flows under applied electric charges.

In Fig. 4.2, we present the variation of density profiles for different surface charge densities (σ). The surface charges are introduced as uniformly distributed partial charges to the carbon atoms at the graphite-water interface. Positive charges on the bottom wall represent anode, while negative charges on the top wall represent cathode. This configuration induces an electric field from bottom wall to the top. Herein, surface charge densities of 0, 6.56, 13.12, 19.68 and 26.24 $\mu C/cm^2$ were taken into consideration, which are similar to the values used in previous MD studies[131, 141]. Resulting electric field strengths produced by these charges are 0, 0.0925, 0.185, 0.2775 and 0.37 V/nm, respectively, which are also in the range of electric field strengths used in earlier MD studies[45, 61, 65]. Although applying such high electric fields is difficult in experimental studies due to the dielectric breakdown of water, it is not totally impractical[147]. For example, pulse discharge method engages pulse voltages through two electrodes in an aqueous environment to generate an electric field on the order of 1 V/nm[147-149].

All density profiles present well-known layering phenomena due to the wall-liquid attraction and volume-exclusions as shown by Koplik *et al.*[112]. Three distinguishable density-layering near each wall and a bulk region in the middle of the channel are observed. The bulk density is maintained at 997 kg/m^3 and the temperature is fixed at 300 K, which fixes the thermodynamic state for all cases. Although the bulk densities are held

constant, near wall region exhibits different behavior for different surface charge densities. Dominated by increasing surface charges, wetting behavior of surfaces increases, and locations and magnitudes of the density peaks differ.
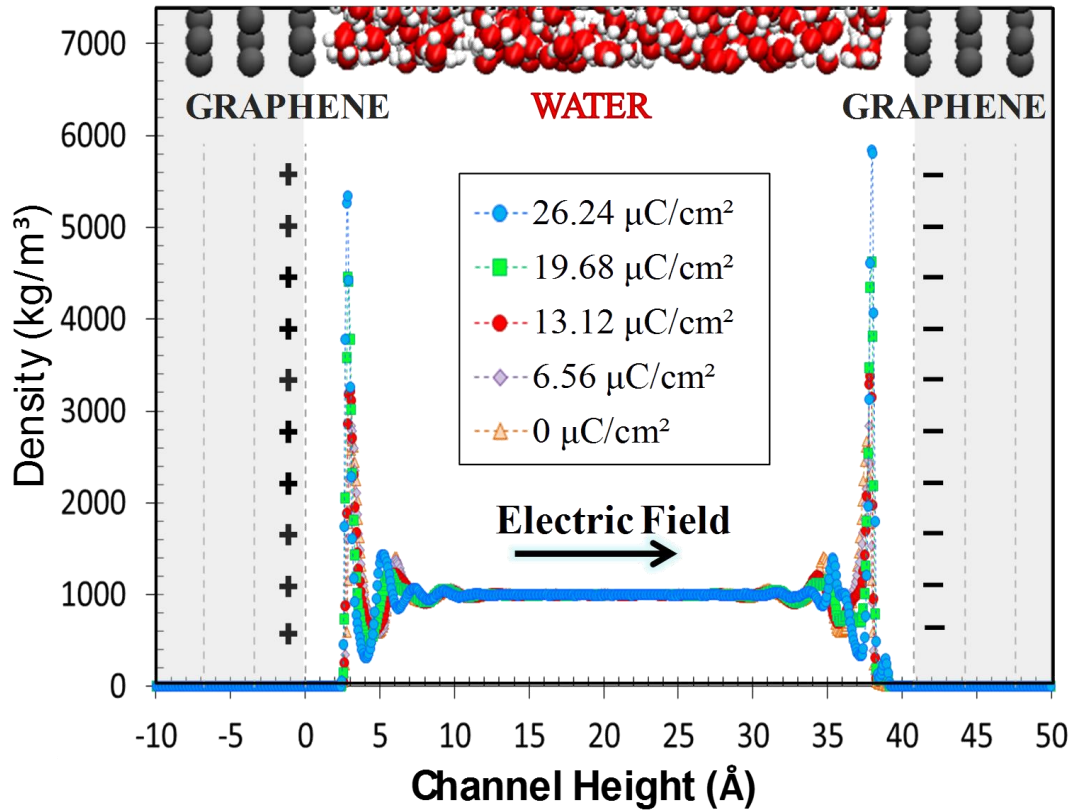
Fig. 4.2 Density distribution under different electric field strengths.

In Fig. 4.3, we show the density profiles within 1 nm distance from bottom and top walls to better investigate the liquid-solid behavior at the interface. An increase on the surface charge increases the number of molecules at the first hydration layer due to higher interfacial energy and stronger wall-fluid interactions. Therefore, magnitude of the first density peaks for each case increases with the surface charge. However, the second density peaks do not show any distinct trends. The third density peaks do not present any
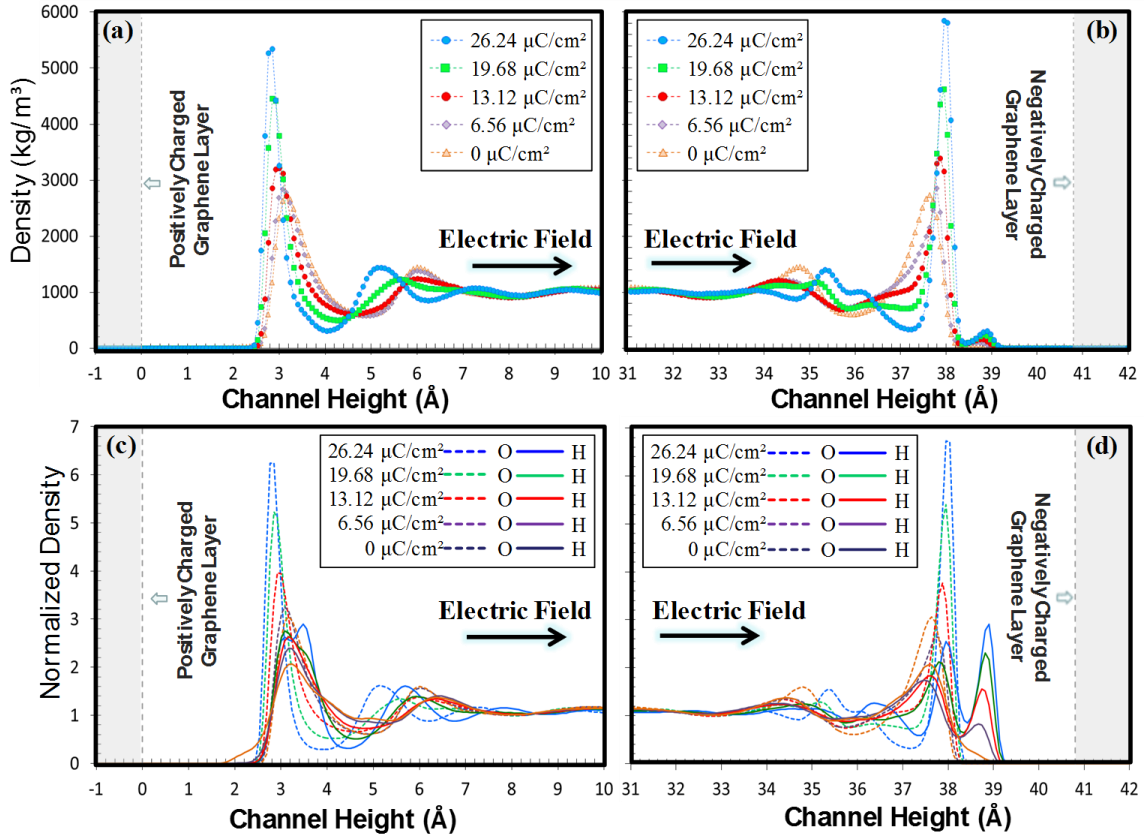
Fig. 4.3 Water density near positively charged bottom wall (a) and negatively charged top wall (b). Normalized oxygen and hydrogen densities near positively charged bottom wall (c) and negatively charged top wall (d).

qualitative or quantitative differences for the given surface charges, because the effect of van der Waals forces from the walls almost diminishes at this location. In addition to the density magnitudes, locations of the density peaks move closer to the wall with increased surface charges. For example, the first density peak is 3.16 Å away from the walls (defined at the center of first graphene wall layer) in the absence of surface charges, while it is located 2.84 Å way from the wall for the largest surface charge. Current results are in good agreement with literature[113]. Density profiles in Figs. 4.3(a) and 4.3(b) are asymmetric under applied electric fields. One can notice a small density peak near the top wall in Fig. 4.3(b), caused by the hydrogen atoms pointing towards negatively charged

surface. Figs. 4.3(c) and 4.3(d) shows oxygen and hydrogen densities normalized by their average values. Density behavior mentioned above can be better understood by the normalized hydrogen densities, which displays and extra hydrogen density peak near the top wall. These peaks occur due to molecular orientations of water molecules, which change by increased electric field. Overall, we observe oxygen density peaks closer to the positive (bottom) wall, while hydrogen density peaks are closer to the negative (top) wall.

The density results show influence of electric field on the orientation of water molecules. To quantify molecular orientations, we computed the probability distribution of water molecules using prescribed angle calculations. An angle of θ is described between the wall surface normal vector and the dipole moment vector of a water molecule as illustrated in Fig. 4.4 [150]. Accordingly, dipole vector of a water molecule points towards the surface when the angle is 180°, and it points away from the surface when the angle is 0°. Similar to the previous works in literature[151-152], only the water molecules in the first hydration shell (within 5 Å distance from the wall) were taken into consideration as the interface region. Angle cosines and probability distribution curves of interfacial water with respect to positively charged bottom wall are shown in Fig. 4.4. Probabilities are expected to change depending on the magnitude and direction of the applied electric field. In absence of surface charge, there is no distinct orientational preference, and the probability distribution shows nearly symmetric behavior. Under applied electric field, more water molecules rotate their dipole moments towards the electric field direction. In other words, number of dipole moments pointing away from the bottom surface increases with increasing electric field. For the largest electric field, almost no water molecules are oriented towards the bottom surface. Two important

factors determine the molecular orientations here. First, positive wall attracts negative oxygen atoms and repels positive hydrogen atoms through Coulombic interactions. Therefore, water molecules at the interface rotate towards the negatively charged top wall with increased electrostatic interactions. Second, the resulting electric field between charged surfaces produces additional force on each water molecule in the electric field direction, which dominates the orientation of water molecules through the entire channel. Probability distribution of water molecules at different z-locations in the channel exhibit very similar results to the orientations shown in Fig. 4.4.
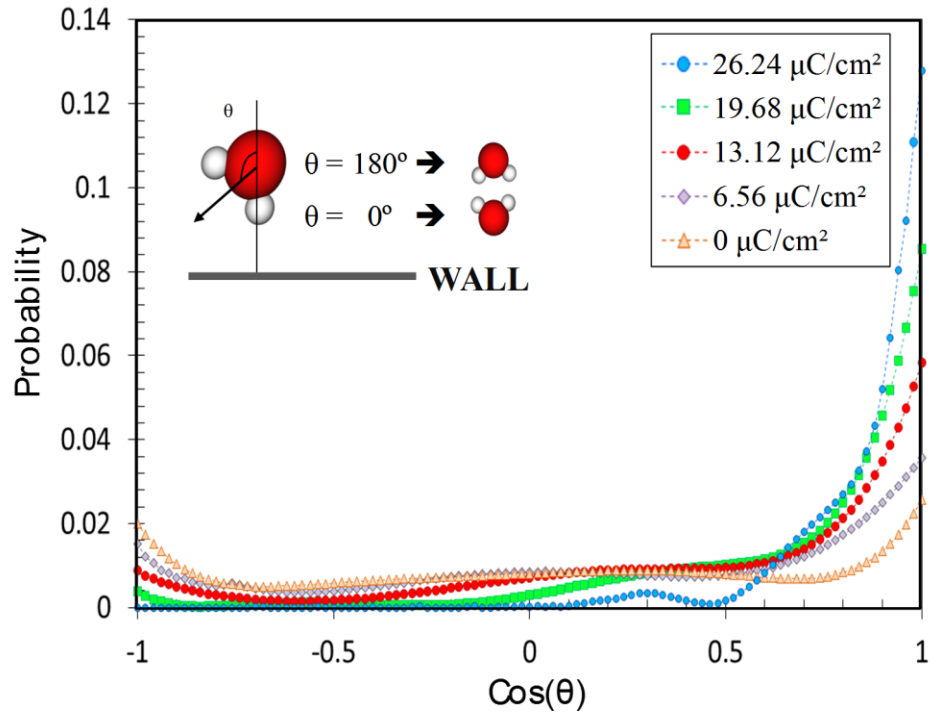
Fig. 4.4 Probability distribution of water molecules adjacent to the positively charged bottom wall.

Next, we present the results of force-driven water flow between oppositely charged graphene nanochannels. Fig. 4.5 shows the velocity profiles normalized with their average values for different surface charge densities. For zero surface charge, plug-like

velocity profile is obtained owing to hydrophobic nature of graphene. This plug behavior originates from weak interfacial resistance at the water-graphene interface, and results in large slip lengths. However, the velocity profiles assume different shapes with variation of the surface charges. With increased surface charge densities, the velocity profiles become parabolic with reduced slip-lengths. This is due to the increasing liquid-wall coupling strength at the interface. Stronger wall-fluid interaction promotes formation of parabolic velocity profiles. At surface charge magnitude of 6.56 $\mu C/cm^2$, a very small parabolic component is observed on the velocity profile, and hence, this case still exhibits plug-like velocity profile. However, distinguishable parabolic velocity profiles with reduced slip-lengths are formed above 13.12 $\mu C/cm^2$. These results not only show control of the surface wetting behavior, but also alteration of nanochannel flow characteristics based on the applied electric field. Velocity profiles show asymmetry, which indicate that the slip length on the negatively charged top-wall is lower than that on the positively charged bottom-wall. This physical behavior can be explained by the density profiles in Fig. 4.3, where hydrogen atoms get closer to the negatively charged bottom-wall, which induce stronger coupling at the interface and reduced velocity slip, compared with the bottom-wall.

In Fig. 4.6, we show variations in viscosity and slip length under different surface charge densities. It is crucial to understand how to actively control transport properties with variation of electric field, and at the same time, assess deviation of the results from continuum predictions. Viscosity and slip lengths in this study were calculated comparing the streaming velocity profiles obtained from NEMD simulations with continuum flow models such as Poiseuille flow (see section 4.2). One can also calculate these transport
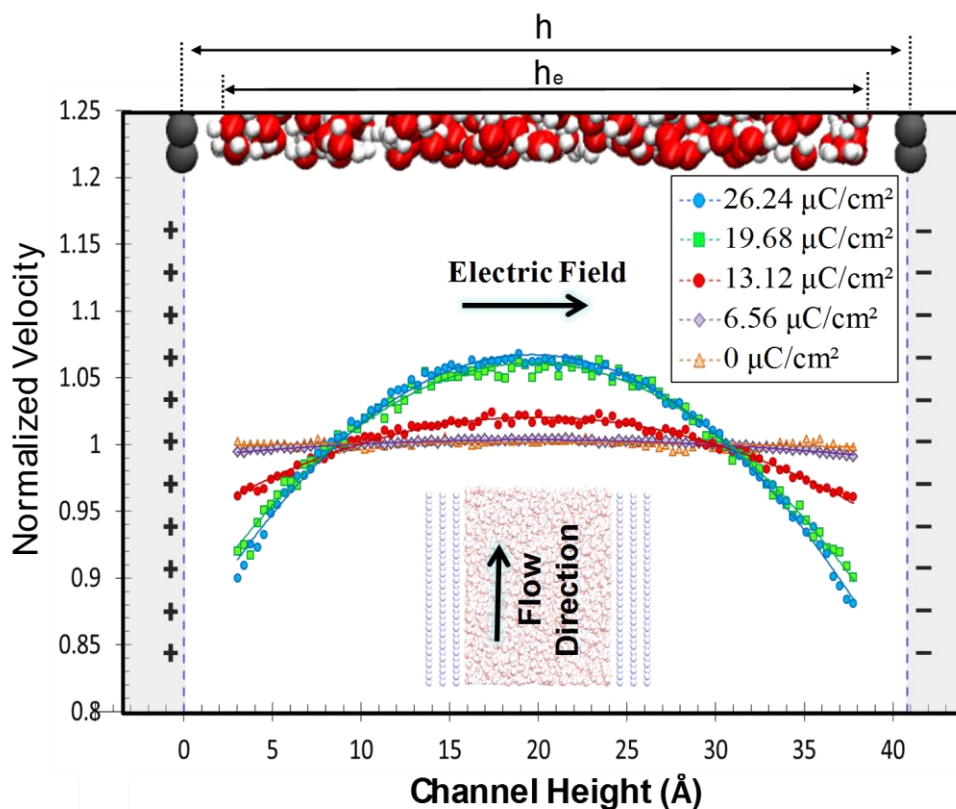
Fig. 4.5 Velocity profiles for different surface charges.

properties using Green-Kubo relations in equilibrium MD (EMD) simulations, which integrates time correlation functions at equilibrium state[41]. Using Green-Kubo relations, shear viscosities of different water models were calculated in several studies in the literature[47-49]. They found the viscosity of TIP4P/2005 model in the range of 820-855 μPa.s which is in good agreement with the thermodynamic viscosity ($\mu_{td} = 858\ \mu Pa.s$) of *w*ater at 300 K and 997 kg/m^3. For zero surface charge, we utilized this thermodynamic viscosity to predict the slip length using Eq. (4.9). Our previous studies suggest that the continuum predictions of the properties of bulk water at known thermodynamic state still hold in nanoscale up to channel heights of 2-3 nm[14, 18]. The velocity profile shows plug-like behavior on the neutral graphene surface with a very

large slip. Applying polynomial fit method to this velocity profile produces large statistical uncertainties in the calculation of the slip length as previously discussed in the study by Kannam *et al.*[34] Here, we used an alternative approach similar to Falk *et al.*[30], where we used Eq. (4.9) assuming that the slip velocity is equal to the average velocity, and predicted slip length at the first water density peak as 64 nm. This value is in good agreement with the values reported in the literature. Kannam *et al.*[34] estimated the slip length of water on a planar graphene surface as 60±6 nm using EMD simulations. Xiong *et al.*[98] applied Green-Kubo relation and calculated the slip length approximately as 54 nm. Koumoutsakos *et al.*[99] calculated the water/graphene slip length as large as 63 nm by Couette flow MD calculations. Variations in the slip lengths reported in the literature could be a result of different potential parameters used in water-water and graphene-water interactions, and also the location of the slip plane. Based on our previous studies we define the slip plane at the first water density peak near the surface. Slip lengths on the wall (β_W) and the slip plane (β_{SP}) are related to each other by $\beta_{SP} = \beta_W + L_O$, where L_O *is* the distance between the wall plane and the location of the first density peak. In this study, we present all slip lengths at the slip plane (i.e. $\beta = \beta_{SP}$) and $L_O = 0.31$ nm.

For surface charges equal to 13.12 $\mu C/cm^2$ or larger, we calculated the viscosities and the slip lengths using the polynomial fit approach. For 6.56 $\mu C/cm^2$ surface charge, there is a weak parabolic behavior, while the velocity profile is mostly plug-like. We used both polynomial fit and plug-like methods together to determine the viscosity and the slip lengths. Fig. 4.6 shows a nonlinear increase in fluid viscosity with increased surface charge and electric field. Absolute viscosity of 1330 $\mu Pa.s$ is obtained for the largest surface charge density, while $\mu=863$ $\mu Pa.s$ for uncharged surfaces. Fig. 4.6 also shows

decreasing slip-length with increased surface charge density for each wall. Slip length for uncharged water-graphene surface is 64 nm, and it decreases to values lower than 4 nm for the largest surface charge density case. Combined effects of increased viscosity and decreased slip for the largest surface charge density case exhibit 20 times reduction the volumetric flowrate between the two cases.
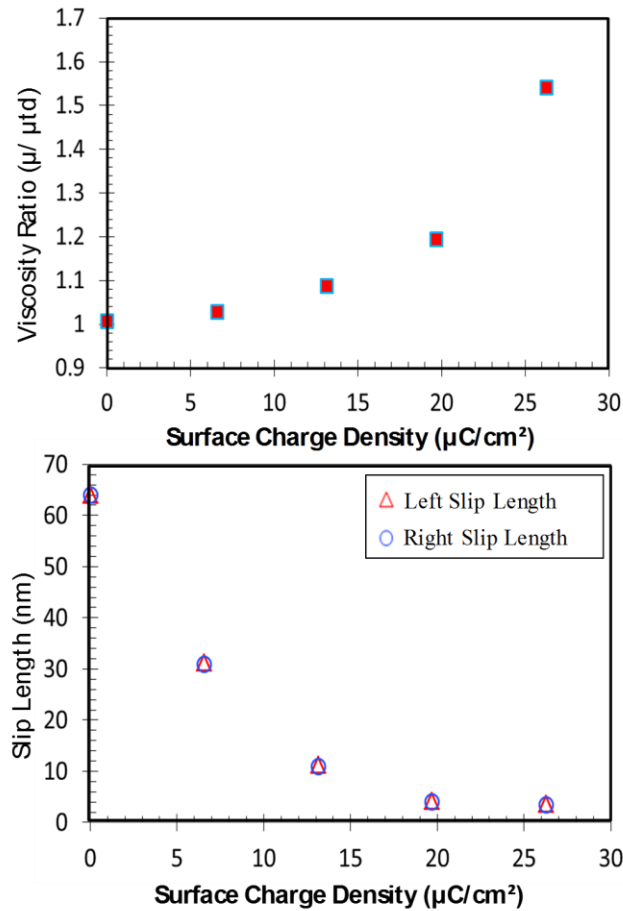
Fig. 4.6 Viscosity ratios and slip length variations with the surface charge.

Table 4.1 shows the viscosity, bottom and top slip lengths as well as the applied force per molecule. Slip length magnitudes on the bottom and top walls exhibit small but non-ignorable differences. As the electric field is increased, asymmetry in the slip lengths becomes more pronounced. This is mainly because of the increased differences in water

Table 4.1 Viscosity and slip-length results for different surface charges

Surface Charge (μC/cm^2)	Viscosity (μPa.s)	Bottom Slip Length (nm)	Top Slip Length (nm)	Normalized Shift Distance	Driving Force (N/Molecule)	p-value
26.24	1330.3	3.91 ± 0.05	3.46 ± 0.06	0.019	1.92x10^{-13}	0.0001
19.68	1028.9	4.54 ± 0.09	4.11 ± 0.09	0.017	1.04x10^{-13}	0.003
13.12	937.5	11.7 ± 0.2	11.1 ± 0.2	0.013	6.09x10^{-14}	0.09
6.56	890.4	31.8 ± 0.5	31.0 ± 0.5	0.010	2.08x10^{-14}	0.5
0	863.4	64.1 ± 0.6	64.1 ± 0.6	-	1.44x10^{-14}	-

density between the two walls. More water molecules assemble near the top wall due to the electric field and rotate their dipoles towards the top wall, creating a small hydrogen density peak (See Fig. 4.3b) that affects the slip velocity. Consequently, the slip lengths on the positively charged bottom wall are larger than the negatively charged top wall. Fig. 4.7 shows MD calculated velocity distribution at σ=26.24 μC/cm^2 with asymmetric curve fit to MD data using Eq. (4.7). We also present a symmetric parabolic velocity fit using constant slip length (β_{Ave}) as an average of the top and bottom wall slip lengths. MD based velocity profile is clearly asymmetric, overshooting the symmetric velocity profile on bottom half of the domain and undershooting it on top half of the domain. Furthermore, the symmetry axis of the MD velocity profile is shifted towards bottom wall by a distance l. In Table 4.1, we present the location of maximum velocity magnitudes, measured from the channel center as the normalized shift distance l/h towards the cathode. This shift distance decreases with reduced surface charge. In order to prove that the reported asymmetries are due to different slip behaviors on the bottom and top walls, we provide statistical uncertainties in the reported slip lengths in Table 4.1. Standard error (SE) in the bottom and top slip lengths are calculated using the slip lengths obtained
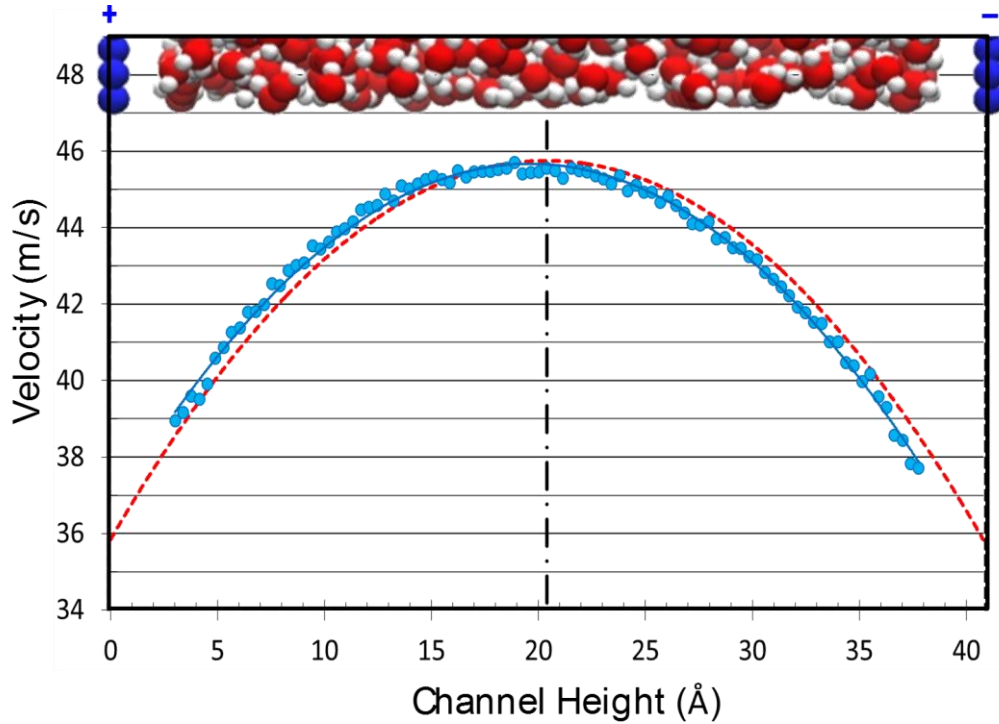
Fig. 4.7 Velocity distributions at σ=26.24 μC/cm². Blue dots are MD data, blue line is asymmetric velocity fit to MD data, red line is the symmetric parabolic fit with β_{Ave} and, the channel center is shown with black dashed line.

from asymmetric velocity fits made to 20 independent samples (*n*) by $SE = S/\sqrt{n}$, where *S* is the standard deviation. Each independent sample was obtained from averaging of 80 consecutive time-averaged data sets. As can be seen, *SE* is below the differences in the reported bottom and top wall slip lengths. It is a fact that the difference in slip lengths of the positively and negatively charged walls are small, but it is not negligible. To understand the significance, one must evaluate the slip difference between bottom and top wall by comparing the actual slip values. For example, for the low surface charge cases (i.e. σ=6.56 μC/cm² and σ=13.12 μC/cm²), this difference yields only 2.5% to 5% variation in the slip lengths. However, 0.5 nm slip length difference results in 15% variation for the σ=26.24 μC/cm² case. In Table 4.1, we also present the p-values (probability of obtaining t-values) using Student's t-Test to compare the slip lengths on

the positively and negatively charged surfaces. It is used to compare two small sets of quantitative data when samples are collected independently and it is based on the sample means difference between two groups. In the Student's t-Test, p-values lower than 0.05 indicate significant difference[153]. Accordingly, the reported slip lengths for σ=26.24 and σ=19.68 $\mu C/cm^2$ cases are statistically different.

The behavior of water in slit nanopores is very sensitive to the confinement (pore size) as well as other parameters such as pressure, temperature, surface physical and chemical properties. Hence, characterization of transport properties of liquids as a function of the scale is crucial for the discovery of the limitations of well-known continuum models in engineering applications. The continuum flow theory can be used to predict the properties of bulk water at a known thermodynamic state for channel heights as small as 2-3 nm[14, 28, 45, 111]. Therefore, we used a fixed channel size of 4.08 nm in the current study to obtain a continuum flow behavior, while the interface phenomenon is still important. However, the results must be consistent under same simulation conditions for larger channel sizes. For this purpose, we selected a larger channel height of h=68 Å for the surface charge density of 26.24 $\mu C/cm^2$. First, we fixed the thermodynamic state following same procedure what we do for smaller channel sizes by keeping the bulk density at 997.2 kg/m^3 and temperature at 300 K. In Fig. 4.8, we compare the water density profiles for two different channel heights but using same surface charge densities. Interfacial density distributions near bottom and top walls present a very good agreement for each channel size. First density peak near bottom wall were found in the value around 5350 kg/m^3 while this is 5900 kg/m^3 near top (negatively charged) wall, showing that

asymmetry in density distribution due to the electric field is still observed in the larger channel.
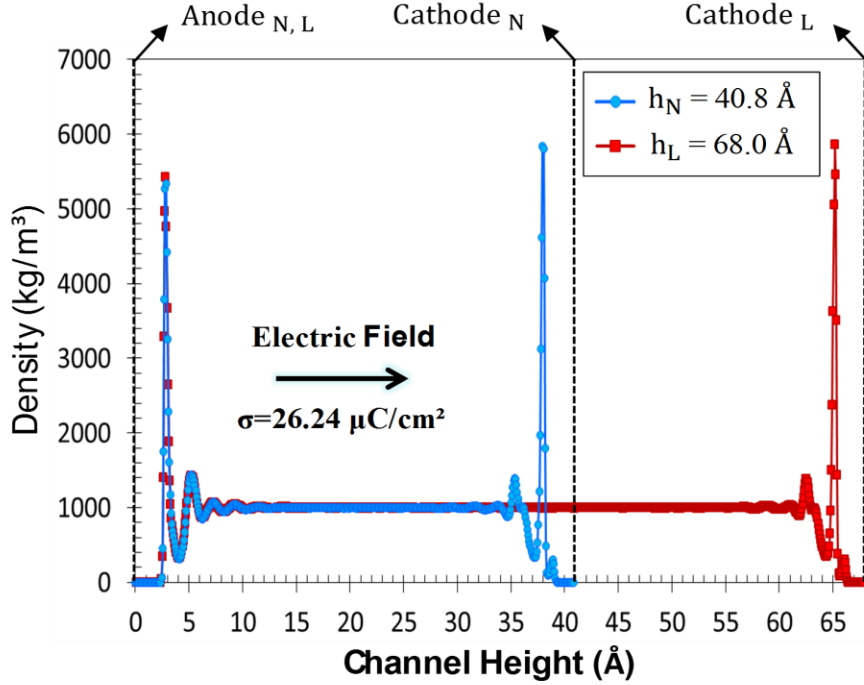
Fig. 4.8 Density distributions at h=40.8 Å and h= 68Å.

In Fig. 4.9, we show the velocity distribution between first density peaks on the bottom and top walls for the channel height of h=68 Å, where the slip planes are located. Similar to the results in the narrower channel, we observed an apparent asymmetry in the velocity profile, resulting in a larger slip length on the positively charged bottom wall in comparison with the negatively charge top wall. To obtain the viscosity and slip lengths values, we applied the polynomial fitting method on the MD velocity profile. It is important to note that simulations conducted in $h = 68$ Å channel at surface charge density of 26.24 μC/cm^2 resulted in nearly identical density profiles, viscosity and slip lengths, verifying that the presented transport phenomenon is scale independent for large enough channels that maintain continuum behavior.
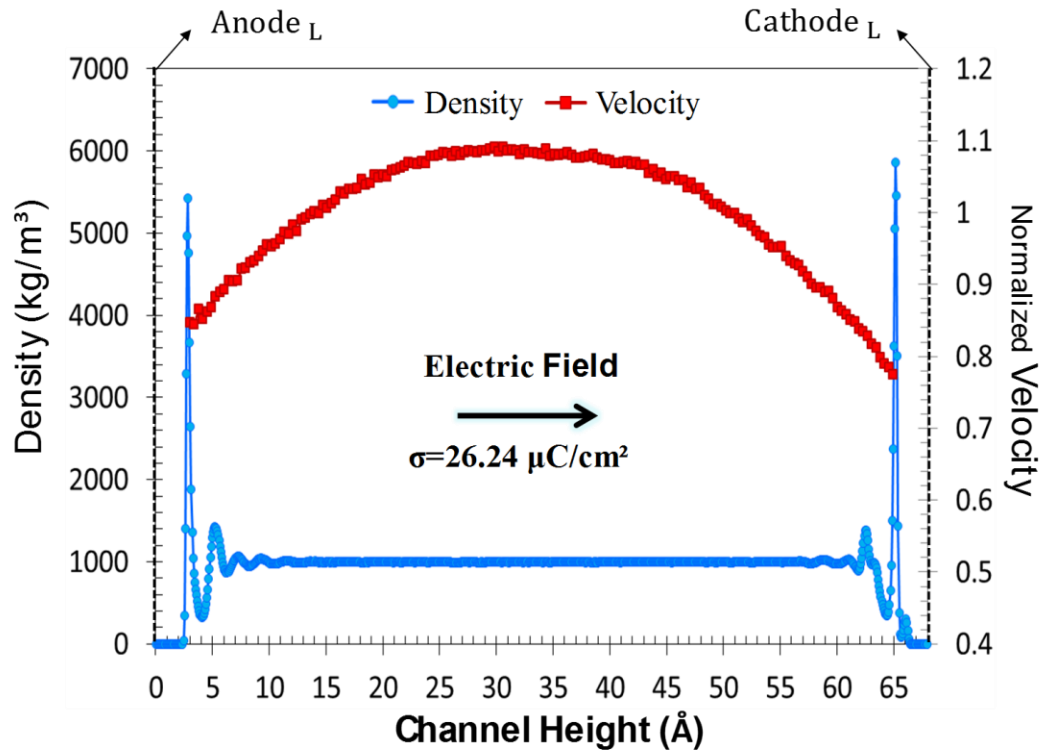
Fig. 4.9 Density and velocity distribution at h= 68Å.

In Table 4.2, we compare our results of viscosity and slip lengths on the bottom and top walls for h=68Å and h=40.8Å channels. The viscosity of water at larger channel height is approximately 1322 µPa.s, which is in a very good agreement with the viscosity for h=40.8Å case. In addition, we found the slip length values on the bottom and top wall as 4.06 nm and 3.56 nm, respectively. These values are also within 4% of the reported results in the narrow channel of h=40.8Å.

Table 4.2. Viscosity and slip-length results for two different channel height

Channel Height (Å)	Viscosity (µPa.s)	Bottom Slip Length (nm)	Top Slip Length (nm)
40.8	1330.33	3.91	3.46
68	1321.71	4.06	3.56
Error (%)	0.6	3.7	2.9

So far, we investigated the variation of structure and dynamics of water due to the resulting electric field by oppositely charged surfaces with surface charges smaller than 30 µC/cm². As the surface charge is increased to a value more than 30.81 µC/cm², density profiles experience a drastic change. For such a case, constant bulk region in the center of channel is replaced by a regular density layering, which implies that water transitions to a highly ordered crystalline structure. This threshold value was determined by systematically increasing the surface charge, so that there is no more constant bulk density in the middle of channel. Starting at σ=30.15 µC/cm², we gradually increased the surface charge density and observed the density distributions. As the threshold value is overcome, water molecules change their arrangements and the bulk density in the center replaced by a density layering[154]. Fig. 4.10 shows variation of density profiles with increasing surface charge. At σ=30.81 µC/cm², density starts fluctuating through the channel height.
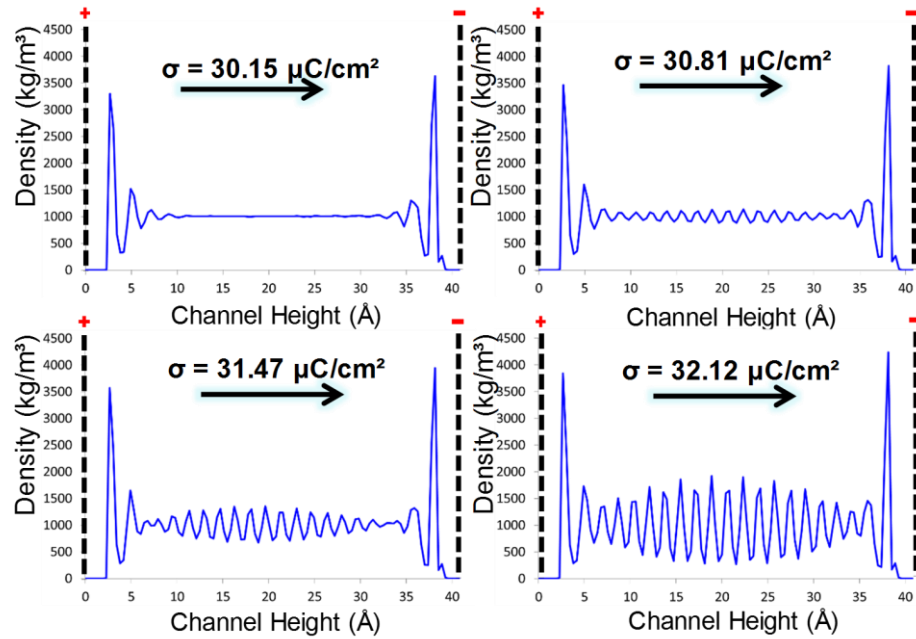
Fig. 4.10 The threshold value of surface charge density for freezing

Fig. 4.11(a) shows normalized hydrogen and oxygen density profiles and the normalized velocity distribution for a surface charge of 32.78 $\mu C/cm^2$. Unlike the previous cases, a distinguishable density layering dominates the bulk region, while density peaks in the near-wall region are still observed due to strong wall force-field effects. These two behaviors elucidate the distinct alignment in the center of channel forming the crystallized phase but still liquid water remains in the near-wall region, as observed in Fig. 4.11(b). Due to crystallization of water, the velocity profile is plug-like in the bulk of the channel. Sharp velocity gradients are observed in the near wall region due to the presence of liquid water near the walls. This crystalline phase arranges water molecules in a hexagonal configuration displaying the characteristics of a solid state like hexagonal ice in the center of the channel[141, 155]. In addition, the nonlinear increase in the viscosity diverges to infinity, which supports solidification (see Fig. 4.6). This phenomenon, known as electro-freezing, was previously reported in multiple computational[138-139, 141] and experimental[156-157] studies in the literature. If the crystallization is thermodynamically and kinetically favorable, a stable heterogeneous nucleation suddenly appears on a solid substrate when the activation energy (free-energy barrier) is overcome[139, 157-158]. Therefore water can crystallize even at room temperature[159]. A strong electric field facilitates ice nucleation by increasing the rate of formation of stable nuclei. An electric field aligns the dipoles of water molecules and restricts their degree-of-freedom normal to the resulting electric field, where the entropy of the liquid phase substantially drops[138]. If the electric field is strong enough, the amount of reduced entropy closes the entropy difference between liquid and solid state, leading to formation of stable, crystalline ice-like structures[138, 160]. It should be noted that freezing

84

of water in nanoconfinements also depends on several other variables such as model size[161], surface geometry and chemistry[140], water model[154], temperature and etc. as well as applied electric field strength. Yan and Patey[161] showed that ice nucleation and growth can only proceed when a certain size threshold is overcome. In addition, crystallization time and geometry shows significant variations on different crystallographic planes in different model sizes[140, 161]. This study only investigates the effect of electric field strength on the estimation of electro-freezing with a fixed model size and geometry.
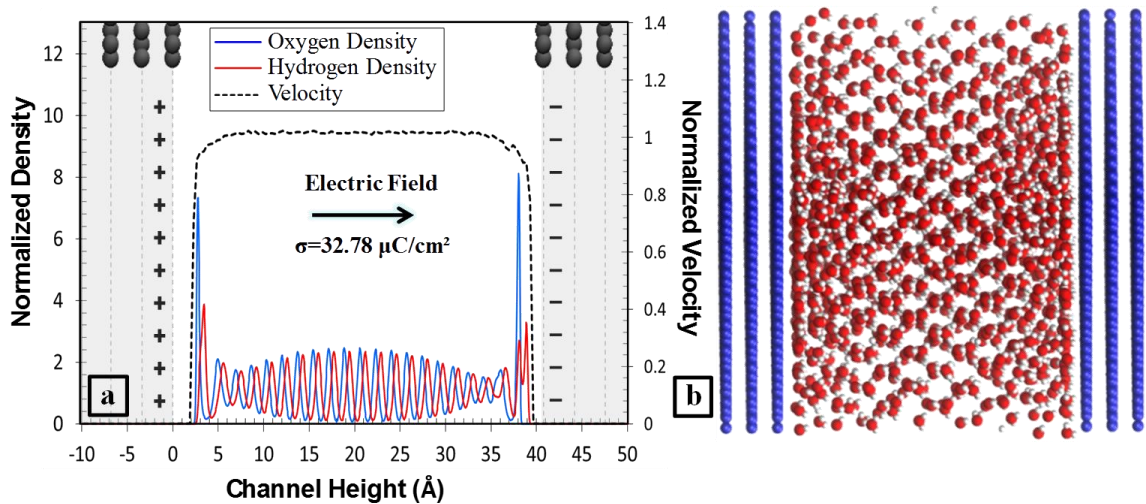
Fig. 4.11 Crystallization of water molecules (a) Normalized hydrogen and oxygen density and velocity profiles; (b) Schematic representation from MD simulations.

From Fig. 4.11, we can conclude that electric field is not strong enough to produce a perfect complete crystalline structure through the entire channel. Therefore, we applied an extreme electric field using a surface charge density of 98.40 $\mu C/cm^2$. Fig. 4.12 illustrates the fully crystallized simulation domain and multiple views from different angles to clarify ice formation. In this case, a perfect hexagonal configuration of water molecules dominates the channel height, except in the near-wall region. Density distribution at the interface is mainly originated from local pressure buildup due to the

constant simulation volume. The density of water reduces during freezing and ice density becomes approximately 920 kg/m^3 after the phase transition. However, constant volume and total number of molecules due to the used NVT ensemble prevent uniformly achieving this density value. Dominated by strong intermolecular forces between the wall and water molecules, the surplus molecules assemble near the walls and increase local pressure. This results in a liquid-like distribution at the interface. Addressing this issue, we calculated the density of the domain by excluding the irregular water molecule aggregation in the near-wall region. We found the density as 917 kg/m^3, which is in good agreement with density of hexagonal ice at 0 $^{\circ}$C [162].

This solid-like ordering is an overall result of the alterations in hydrogen bonding networks due to the electric field. In liquid form, water molecules move randomly through the space, constantly breaking and reforming hydrogen bonds between the molecules[163]. With very strong electric field, the orientation of the molecules drastically changes, resulting fully aligned dipole moments through electric field direction as shown in Fig. 4.12. Consequently, the random motion of liquid water diminishes, and the molecules become relatively locked at their positions. For such cases, the hydrogen bonds forms more frequently without breaking, creating a stable and energetically more favorable regular pattern. In reality, a water molecule in ice hydrogen bonds with four other neighboring molecules to create a tetrahedral crystal lattice, while the number of hydrogen bonds per molecule in the liquid phase is lower than this value[163]. We analyzed the liquid water and resulted solid-like phase by quantifying the number of hydrogen bonds per molecule in the bulk region of the channel following the geometric criteria in the study by Marti[164]. For uncharged case, the average number of hydrogen bonds per

water molecule in the bulk region was 3.41, which reasonably agrees with the experimental value of 3.3 reported by Smith et al.[165] and numerical result of 3.50 by Ho and Striolo[113]. This value increases with an increased electric field in the system. Ritos et al.[166] also showed that electric field increased the average number of hydrogen bonds per water molecule in a carbon nanotube from 3.50 to 3.95, where they pointed out solidification at large field strengths. We calculated the average number of hydrogen bonds in the fully crystallized region in Fig. 4.12 as 3.97, which is similar to ice[167].
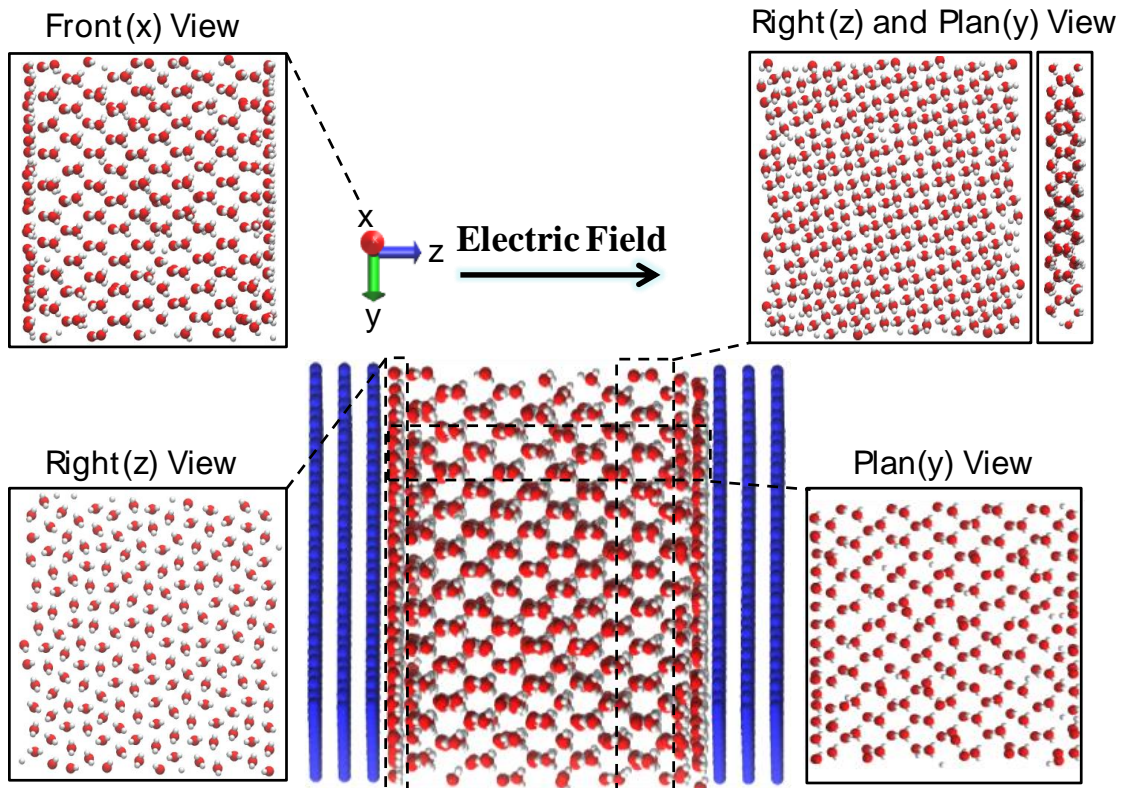
Fig. 4.12 Fully crystallized water domain.

4.5 Conclusion

Using MD simulations, we investigated force-driven water flow in graphene nanochannels with opposing surface charges. Varying the surface charge density changes

the applied electric field, which significantly alters the surface wetting and flow characteristics. With increased electric field, the first water-density peaks get closer to the electrodes and the magnitudes of the density peaks increase; and asymmetric density distributions are observed due to water molecules orienting their dipoles towards the electric field direction. Force-driven flows under applied electric fields exhibit increased water viscosity and decreased slip lengths. For example, the slip-length of water on graphene surfaces at 26.24 $\mu C/cm^2$ charge density is 16 times smaller than that on electrically neutral surfaces, and the water viscosity increases nearly 54% from its thermodynamic value. Furthermore, asymmetric velocity profiles are observed with increased electric fields, resulting in smaller slip lengths on the cathodes than the anodes. This is due to positively charged hydrogen molecules getting closer to the cathode compared to the position of negatively charged oxygen molecules near the anode. Above 31 $\mu C/cm^2$ charge density, electro-freezing is observed, where water crystallizes in hexagonal configuration in the middle of the channel and liquid water is observed near the electrodes. Force-driven flow of this system shows transition from parabolic velocity profile to plug like motion of ice with large velocity gradients near the walls. Further increases in the electric field enables better transition to solid state by providing more populated hexagonal configuration of water molecules. Overall, results show the possibility of flow control using charged graphitic surfaces, where applied electric fields can substantially decrease the flow rate by reducing the slip length and increasing the water viscosity; eventually stopping the flow due to ice formation. These findings are also relevant in further miniaturization of electro-wetting-based droplet microfluidic

systems, where slip length differences on the anodes and cathodes may lead to variations in the droplet wetting angle on the electrode surfaces.

Chapter 5

SURFACE CHARGE DEPENDENT TRANSPORT OF WATER IN GRAPHENE NANOCHANNELS

5.1 Introduction

Nanofluidic systems can provide significant advantages in addressing our industrial, agricultural and drinking water needs. For example, "tunable nanomembranes" can be developed to provide cost effective water deionization and desalination techniques where the membrane surface charge can be modified to remove specific ionic species from pressure-driven water flows, either by chemical alteration of the surface functional groups or using gated electrodes[5, 168]. However, the surface charges may significantly alter water flow inside the nanoconfinements. Proper assessment of the "tunable nanomembrane" technology requires enhanced understanding of water transport as a function of the surface charge.

Molecular surface force-fields and confinement affect liquid transport in nanoscale systems[55]. The major mechanism induced by surface forces is density layering of liquids near the walls that extends several molecular diameters in the near-surface region[112]. Liquid molecules undergo solid like ordering near the walls which ultimately determines the liquid/solid momentum exchange at the interface[169]. Depending on the liquid/solid interaction strength, liquid may exhibit velocity-slip, no-slip or adsorption[26]. Also the channel averaged fluid density and apparent-viscosity deviate from their thermodynamic

bulk values[14, 55]. The fluid density and flow exhibit continuum behavior only sufficiently far away from the surfaces[132]. As a result, predictions of the continuum transport models become inaccurate with reduced channel size, and ultimately discrete transport of liquid molecules under the influence of wall force field dominates the transport[133].

The influences of velocity slip and apparent viscosity on nanoscale water transport has been studied extensively[24, 34, 170]. Water flow through graphene nanochannels and CNTs exhibit ultra-fast transport due to the large slip lengths and increased structural order of water in nanoconfinements[30, 171-172]. These behaviors promoted use of graphene based materials for nanomembrane applications[119, 173-174]. However, a breakdown of flow rate enhancement was observed in the cases of chemical functionalization or oxidation of the surfaces[175-177]. Many desalination applications use Coulomb forces to repel ions by adjusting the surface charges inside or at the entrance of the nanomembranes[178]. Unfortunately, the surface charges required for selective ion passage decreases the flow rate of purified water and increases the pressure drop required to maintain the desired flow rate[179].

The effects of surface charge on liquid/surface interactions were investigated in terms of surface wetting. Variation of both static wettability and wetting kinetics were observed as a function of surface charge density[180]. Molecular dynamics studies of nanodroplets on charged surfaces showed enhancement of surface wettability with increased charge density, where the wetting angle decreased and the surface became more hydrophilic, corresponding to stronger liquid-solid interactions[136]. Polarizable water molecules reorient themselves on a charged surface. Increasing the surface charge magnitude aligns the dipole moments of water molecules and restricts their degree of

freedom[113, 137]. This effect can be crucial in nanoscale confinements and significantly alter the momentum exchange of liquid molecules.

Recently, we investigated deionized water flow through graphene nanochannels subjected to opposing surface charges, and have shown that the resulting electric field induced asymmetric density distribution and velocity profiles in the channels. With increased electric fields, slip length decreased and the apparent viscosity increased, while electro-freezing of water was observed above a certain threshold value. Results indicated the possibility of using oppositely charged graphene nanochannels for flow control applications[23]. Current study distinguishes itself due to use of graphene nanochannels subjected to identical positive electric charges. For such a case, charged graphene surfaces act as gated electrodes, which might significantly alter the flow. In this study, we do not include O^+ and OH^- ions to avoid electric double layer formation. Furthermore, the number of free ions in nanochannels is often very small, and their presence do not greatly affect force-driven flows. Therefore, the current study closely mimics water desalination or deionization processes using graphene nanochannel surfaces as gated electrodes, while avoiding additional complexities of modeling ionized fluids.

To the best of our knowledge, the effects of surface electric charge on the structure and dynamics of water have not been previously reported in the literature. Thus, we carried out non-equilibrium molecular dynamics (NEMD) simulations for force-driven water flow through identically charged planar graphene surfaces. The primary objective of the present study is to investigate the effect of surface charge density on the structural and transport properties of water in graphene nanoconfinements at a length scale, where the continuum behavior is still valid. We principally focus on the density distributions,

molecular orientations, velocity profiles, viscosities, slip lengths and flow rates after ensuring a fixed thermodynamic state. A unique computational aspect of this work is the use of large cutoff distances to model Coulomb interactions between charged molecules, since Ewald summation algorithm is inapplicable for simulation systems with a net electric charge.

5.2 Theoretical Background

In this study, we consider force driven water flow in positively charged graphene nanochannels illustrated in Fig. (5.1). For a 1D, steady, incompressible, fully developed and force-driven Newtonian fluid flows between parallel plates with a Navier-type slip on the walls, the velocity equation is given in Eq. (3.6), which could also be represented as in the following form

$$u(z) = \frac{fh^2}{2\mu}\left(-\left(\frac{z}{h}\right)^2 + \left(\frac{z}{h}\right) + \left(\frac{\beta}{h}\right)\right) \tag{5.1}$$

where β, $u(z)$, f and μ are the slip length, velocity field, driving-force and the fluid viscosity, respectively. One can notice that there are equal finite charges on opposing graphene walls, so that we define a single β rather than distinct slip values on bottom and top wall. For parabolic profiles, we apply a polynomial fit approach using the velocity profiles obtained from MD simulations in order to find the slip length ($\beta = 2C\mu/fh$) while we utilize plug-flow method to find the slip length ($\beta = 2\mu\bar{u}/fh$) for flat velocity profiles[18, 53]. The details of these two methods are discussed in Chapter 3.

5.3 Molecular Dynamics Simulation Details

The three-dimensional model consists of liquid water molecules confined between two solid graphitic walls as shown in Fig. 5.1. Each wall is made of three graphene layers

which were placed 3.4 Å apart from each other. Graphene sheets were oriented on the XY plane with a Bernal (ABA) stacking arrangement[142]. Dimensions of the simulation domain were set as 3.69×3.81×5.44 nm in the, lateral (x) and longitudinal (y) and vertical (z) directions, respectively. In this study, we specifically picked a channel height of h=4.08 nm, which is large enough to exhibit a substantial bulk region around the channel center and density layering near the walls due to wall-force field effects. In much narrower channels, description of the thermodynamic state breaks down and water molecules experience discrete molecular transport. Hence, derivation of continuum properties such as density, velocity and viscosity becomes irrelevant[111]. Our previous studies have shown that the continuum flow theory can be used to predict the properties of bulk water at a known thermodynamic state for channel heights as small as 2-3 nm[14, 18]. Qiao and Aluru [45] also presented that continuum predictions can still hold up to the channel heights of 2.2 nm.

Intermolecular interactions between all atomic pairs were modeled using Lennard-Jones (LJ) and Coulomb potentials as given in Eq. (3.9). We used a cut-off distance of 1nm for all LJ calculations (r_{C-LJ}=1 nm). Water molecules were modeled using a rigid four-site TIP4P/2005 model[106]. We only considered the LJ interactions of oxygen atom in a water molecule, assuming hydrogen's contribution is negligible due to its much smaller mass and size. Interactions between carbon and oxygen atoms were calculated based on the parameters obtained by experimental study of Werder *et al.*[108] We excluded the interaction between carbon atoms to attain a rigid (cold) wall behavior, which provides substantial enhancement in the computational efficiency[42]. Only the carbon atoms at the

94

innermost layers of graphene channels were modeled as charged particles, while the remaining carbon atoms were neutral.
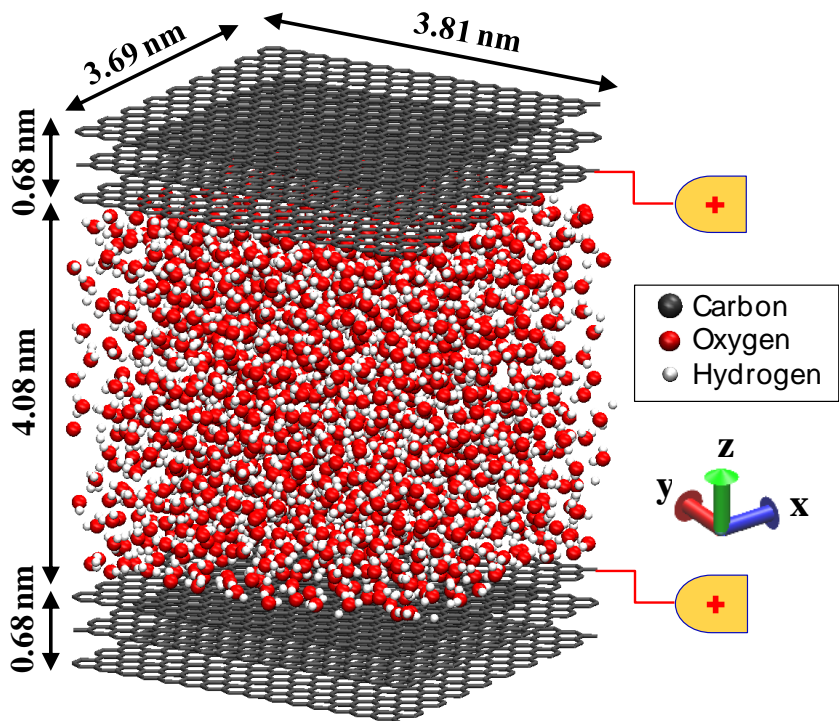
Fig. 5.1 Schematic representation of simulation domain.

One of the main challenges we faced during this study was the calculation of long range Coulomb intermolecular forces. Our system consists of water molecules carrying equal amounts of positive and negative charges, and carbon molecules having positive charges only. This results in a system with a positive net charge. Ewald summation algorithm is frequently used to calculate the long range part of Coulomb forces beyond the cut-off distance (r_{C-Coul})[181]. However, this algorithm was developed with the assumption that the net charge of the system is zero. For systems with a net electric charge, the Ewald summation algorithms, such as PPPM[182] add additional phantom-charges to make the system neutral in order to bring the simulation to a state at which

algorithm is applicable[109]. This creates an artificial force on simulated molecules and develops unphysical behaviors[183-185]. In order to simulate a system with a net electric charge, we systematically increased the cut-off distance employed at different surface charge density cases and examined the resulting water density profiles, as shown in Fig. 5.2(a). Systematically increasing the cut-off distance, density distribution of water converged to a unified profile when the cut-off distance became equal to or higher than the simulated channel height of 4.08 nm. Results obtained using PPPM with 1nm cut-off distance is also shown in the figure and exhibits wrong density profile due to electro neutrality induced by the Ewald summation algorithm. As the cut-off length reached the domain size, force interactions of any molecule with every other molecule in the domain and its own image on the periodic surfaces could be calculated properly. In order to validate the results obtained using r_{C-Coul}=4 nm, we performed further simulations, where the net system charge was neutralized by adding ions with opposite charges to the imposed surface charge. For such cases, the well-known PPPM algorithm with r_{C-Coul}=1 nm was appropriately employed for calculating the Coulomb forces. Since the number of ions added for neutralization of low surface charge cases were small and had negligible effects, water densities for low surface charge cases showed good agreement between r_{C-Coul}=4 nm without PPPM and r_{C-Coul}=1 nm using PPPM (Fig. 5.2(b)). However, high surface charges required addition of large number of ions, which started affecting the water density profiles, and comparisons with the density profiles of water with no ions became unreasonable. Overall, we validated the results of r_{C-Coul}=4 nm using a cut-off distance dependence study and an agreement is obtained with the results of PPPM at low-surface charge systems neutralized by addition of ions. Therefore, Coulomb

interactions between all charged particles were calculated properly using 4nm cut-off distance.
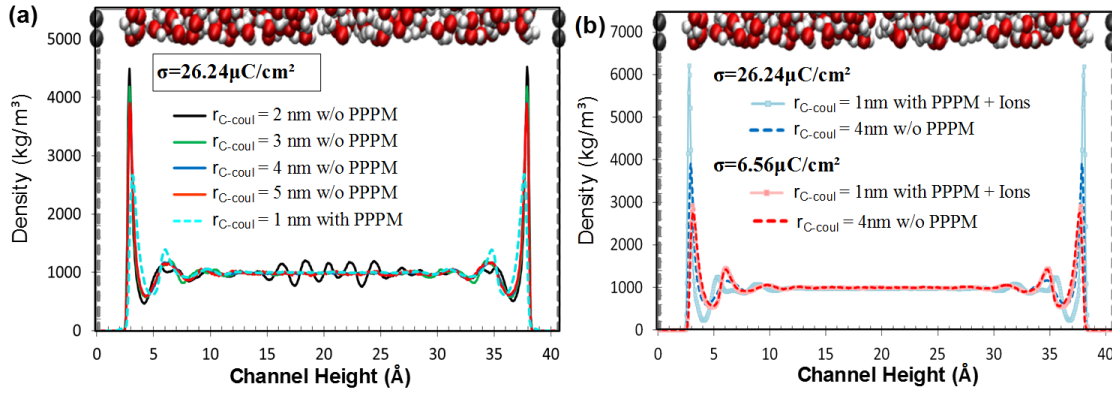
Fig. 5.2 (a) Density distribution in a charged channel calculated using PPPM with r_{C-Coul}=1 nm, compared to distributions of r_{C-Coul}=2, 3, 4 and 5 nm cases without PPPM. (b) Density distributions at different surface charges obtained by r_{C-Coul}=4 nm and using PPPM with r_{C-Coul}=1 nm and ion addition.

This study uses Large-Scale Atomic/Molecular Massively Parallel Simulator (LAMMPS)[105]. Periodic boundary conditions were applied in x and y directions. Initially, each system achieved thermal equilibrium in a Canonical (NVT) ensemble before being subjected to any driving-forces. For this purpose, initial velocities of each water molecule were randomly assigned by imposing a Gaussian distribution based on the specified temperature. Then, the MD system was run for 1ns using 1fs time steps to reach an equilibrium state in absence of external forces. The thermodynamic state was fixed by maintaining the temperature of water at 300K using Nose-Hoover thermostat and keeping the bulk density of water at 997kg/m^3. Temperature was computed from the total kinetic energy and the equilibrium state was verified.

Next, force-driven water flow simulations were performed starting from the equilibrium conditions. Flow simulations employ Nose-Hoover thermostat on the degrees

of freedom perpendicular to the flow direction. The flow was driven by an external force in y-direction imposed on each atom of the water molecule based on their mass. In order to avoid the nonlinear effects, the magnitude of the body force for each surface charge density case was selected to limit the maximum water velocities under 60m/s [114-115]. We determined this linear response regime by systematically investigating the average channel velocity as a function of the driving-force (Not shown for brevity). Time scale for momentum diffusion was estimated using $t_d \approx h^2/v$, where h and v are the channel height and kinematic viscosity, respectively[18]. Steady flow was ensured by initially running the system for 1ns, which corresponds to $6t_d$. Subsequently, an additional 6ns was performed for data collection and statistical averaging, which creates 800 independent time-averaged data sets. In order to obtain better resolution at the graphene-water interface, we divided the simulation box into 1200 bins in the direction of the channel height.

5.4 Results

We first investigate the density distributions of water between positively charged graphene nanochannels. To generate uniform surface charge density (σ), we assigned single point charges to each carbon atom in the innermost layer of each graphitic wall. In the current study, we used surface charge densities of 0, 6.56, 13.12, 19.68 and 26.24 $\mu C/cm^2$ based on the values reported in similar MD studies[131, 141]. Such surface charge densities are relatively high, but not totally impractical[64-65]. Fig. 5.3 shows water density profiles obtained under five different surface charges. A constant density region is observed in the middle of channel with three apparent density layering near each wall due to the wall-liquid attraction and volume-exclusion effects[112]. The thermodynamic state
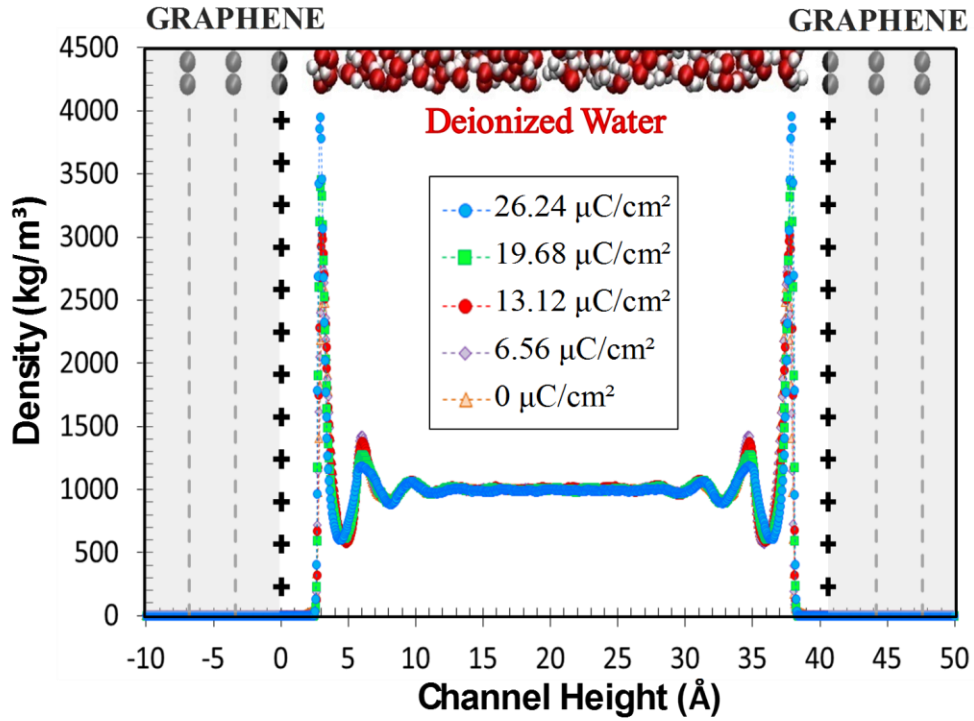
Fig. 5.3 Water density profiles obtained for different surface charge densities.

for all five cases is identical since the water reaches a constant density of 997 kg/m^3 in the bulk region and the system is kept at T=300 K. Results show increased water density in the near wall region with increased surface charge, indicating enhanced surface wetting. Density profiles show an empty region between the first water density peak and the wall center. This region is about $L_O \approx 0.3$ nm thick, which is not negligible compared to the channel height of h=4.08 nm. Since water molecules concentrate at the first density peak, L_O also defines the slip-plane for flow studies. In Ghorbanian *et* al.[18], we defined an effective channel height as $h_e = h - 2L_O$, and base all continuum calculations on the effective channel height.

To elucidate the interfacial density behavior, we examine the density profiles within 1 nm distance from the wall in Fig. 5.4. We only present the results near one wall because the density distributions near both walls are the same. Magnitude of the first

density peak increases with increased surface charge. This is a result of higher interfacial energy and stronger wall-fluid interactions that increase the number of molecules at the first hydration layer. On the other hand, the second density peaks are reduced as the surface charge increases while the third density peaks do not show any variation as a function of the surface charge. Furthermore, surface charge also alters the location of the density peaks. At σ=26.24 $\mu C/cm^2$, the first density peak is formed approximately at $L_O = 2.94$ Å, while the peak was at $L_O = 3.16$ Å for the uncharged case. Current findings agree with the results reported earlier[113]. Fig. 5.4(b) shows oxygen and hydrogen densities normalized by their average values. Due to the Coulomb forces from the positive surface charges, oxygen molecules are located closer to the surface within the first two density peaks.
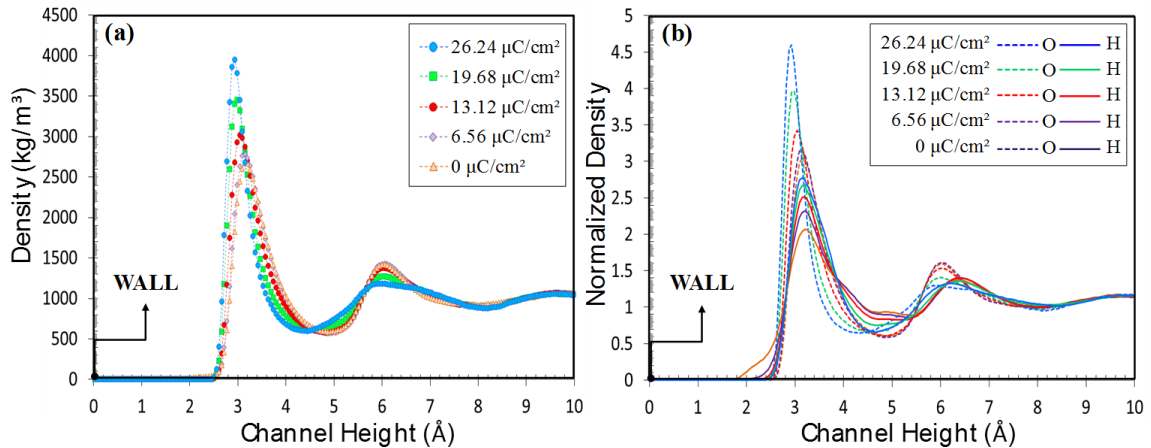
Fig. 5.4 (a) Water density distribution within 1 nm of the positively charged surface; (b) Distribution of normalized oxygen and hydrogen densities within 1 nm of the surface.

Oxygen and hydrogen density distributions suggest that applied surface charges have substantial effect on the orientation of water molecules. We calculated the probability distribution of water molecules using a prescribed angle approximation in order to quantify these molecular orientations. We defined angle θ between dipole vector

of a water molecule and the surface normal vector as shown in Fig. 5.5 [150]. The angle becomes 0° when the molecular dipole vector points away from the wall, while it becomes 180° when the molecular dipole vector points towards the surface. Therefore, the probability distribution varies between +1 and -1 depending on the angle. In Fig. 5.5, we present the probability distribution and angle cosines of interfacial water molecules at different surface charge densities. Similar to the earlier studies in the literature[151-152], we only considered water molecules within the first hydration layer, which is 0.5 nm distance from the wall. The probability of water molecules on a neutral surface shows almost a symmetric distribution where no specific orientations are observed. However, molecular orientations are altered with the surface charge. Positive wall attracts negative oxygen atoms and repels positive hydrogen atoms due to Coulomb forces. Therefore, water molecules at the interface rotate their dipole vectors away from the positively charged surfaces with increased electrical charge. As a result, the $cos(\theta)=1$ probability increases, corresponding to negatively charged oxygen orienting towards the surface and positively charged hydrogen orienting away from the surface.

Probability distribution of water molecules at different z-locations in the channel is shown in Fig. 5.6. Water orientations were measured inside every 0.3 nm thick slabs starting from interfacial water hydration layer of each surface towards the channel center. Results are for the surface charge of 19.68 $\mu C/cm^2$. The water dipole moments become more equally distributed by moving away from the surface. Dipole distribution near the channel center is nearly symmetrical even for this high surface charge case. The orientations of interfacial water molecules near both walls are similar due to the identical electrical charges imposed on each surface.
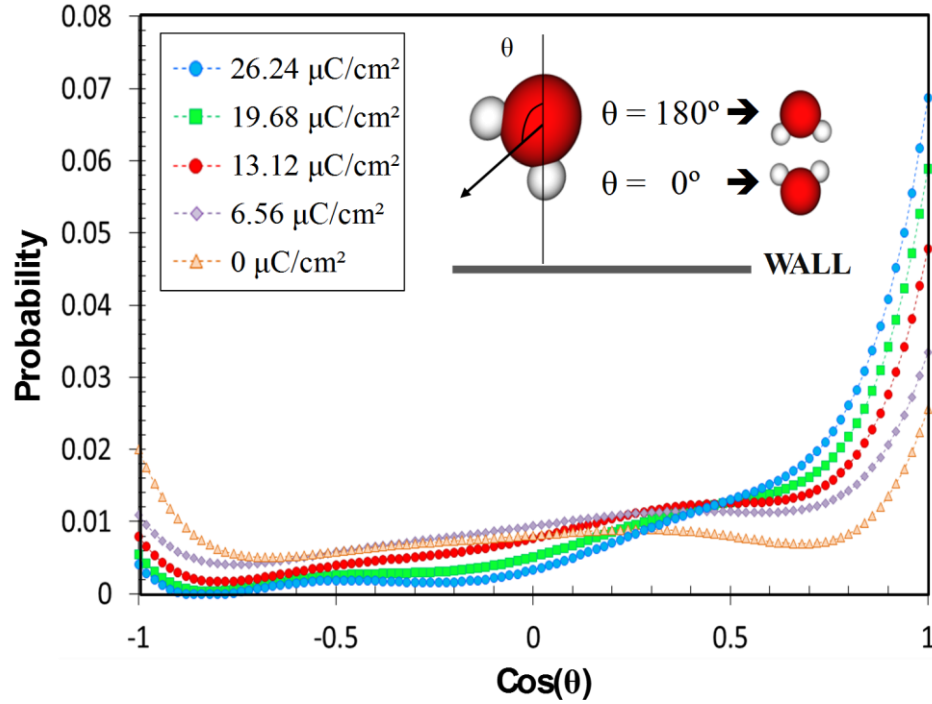
Fig. 5.5 Probability distribution of water molecules at the interface for different wall charges.

Fig. 5.7 shows the velocity profiles normalized with their channel averaged values for different surface charge densities. For zero surface charge, plug-like velocity profile is obtained due to weak interfacial resistance at the water-graphene interface that results in large slip lengths. Slip length normalized with the effective channel height ($\beta^* = \beta/h_e$) determines the shape of the velocity profile in a given channel. Focal length of the parabola increases with increased β^*, exhibiting plug flow behavior for $\beta^* >> 1$.[18] For the zero surface charge case, $\beta^* = 18.4$, and hence, the velocity profile is nearly uniform. Imposing surface electric charges alter the water-graphene interactions and the resulting velocity profiles. Electrical charges on the surface increase the liquid-wall interaction strength, forming parabolic velocity profiles with reduced slip-lengths. This effect becomes more prominent with increased surface charge. In addition, the velocity profiles

are symmetric with respect to the channel center, implying equal slip lengths on the walls. Using two negatively charged walls also created similar effects (not shown for brevity). The velocity profiles show that surface charges can induce active control of surface wetting and fluid flow in nanochannels.
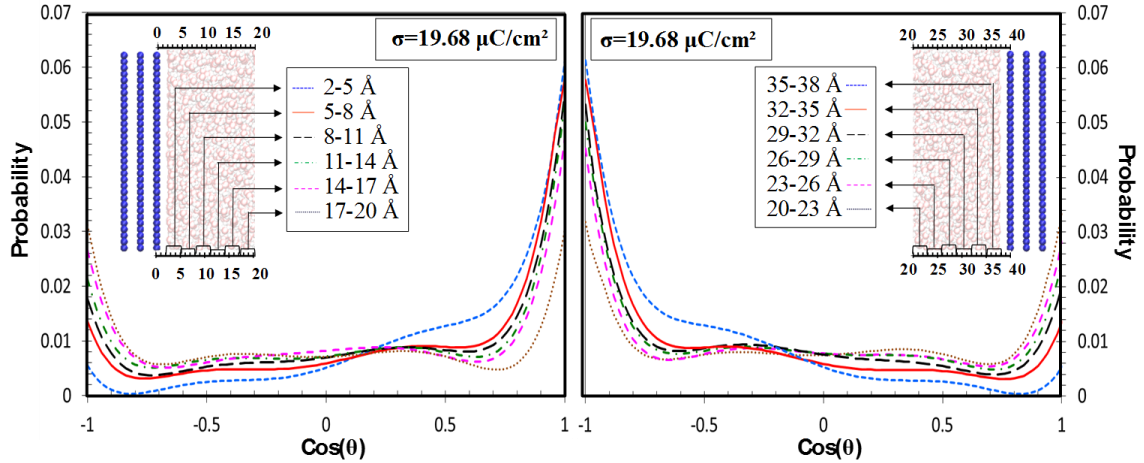
Fig. 5.6 Probability distribution at different locations.

Fig. 5.8 presents MD computed viscosity normalized by water viscosity at the given thermodynamic state (μ/μ_{td}), and the MD computed slip lengths for different surface charge densities. We targeted for a better understanding of surface charge effects on the transport properties, and at the same time, assess deviations of the results from continuum predictions. We calculated viscosity and slip length of each case comparing the velocity profiles obtained from NEMD simulations with well-known continuum Poiseuille flow model. We particularly describe the slip-plane at the first water density peak adjacent to the wall. The slip length (β_{SP}) at the slip-plane is related to the slip length on the wall (β_W) by $\beta_{SP} = \beta_W + L_O$, where L_O is the distance between the location of the first density peak and the wall. All slip lengths reported in this study are

calculated at the slip-plane (i.e. $\beta = \beta_{SP}$), where $L_O = 2.94$ Å and $L_O = 3.16$ Å for the $\sigma=26.24$ µC/cm^2 and $\sigma=0$ µC/cm^2 cases, respectively.
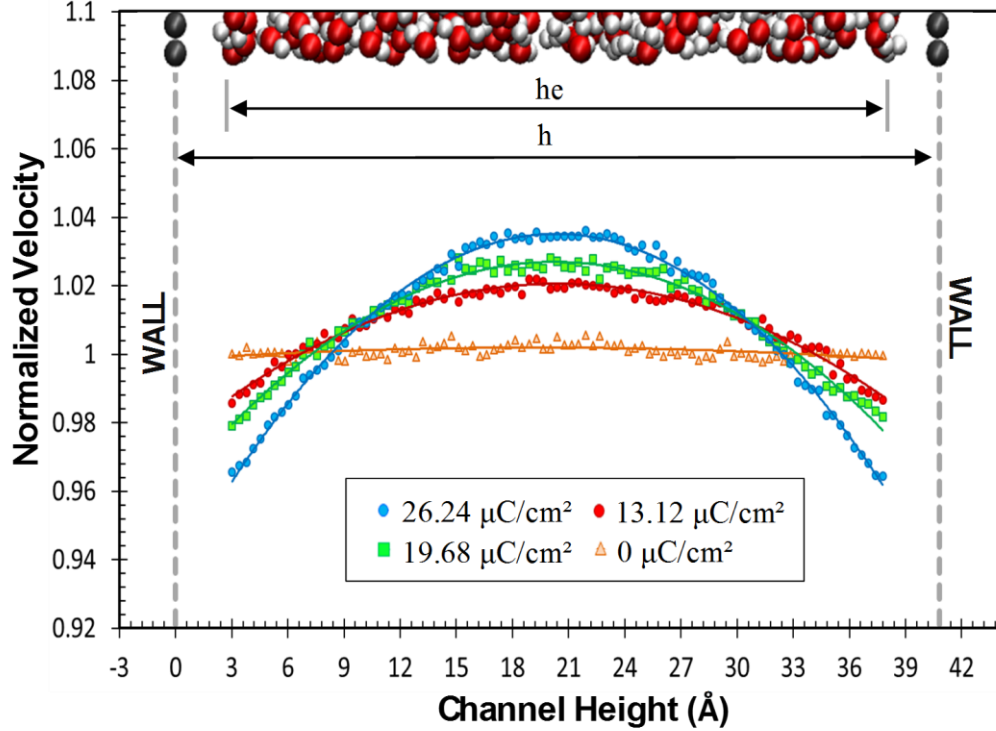
Fig. 5.7 Velocity profiles for different surface charges.

Increasing the surface charge promotes parabolic velocity distribution due to increasing water-graphene interfacial strength. For $\sigma =13.12$ µC/cm^2 or larger, velocity profiles exhibit parabolic shapes, where we can easily use the polynomial fit approach in order to predict the viscosities and slip lengths. For $\sigma = 6.56$ µC/cm^2, we applied the plug-like method and polynomial fit approach together to verify our results since the velocity profile presents a small parabolic component. Fig. 5.8 shows viscosity and slip length variations under different surface charge densities. Results exhibit non-linear increase in water viscosity with increased surface charge density. The absolute viscosity for the largest surface charge density is approximately 1103 µPa.s, while it is 863 µPa.s

for the uncharged surface. Results show drastic reduction in the slip length with increased electrical surface charge. The slip length decreases to 9.7 nm for the largest surface charge density case, exhibiting 6.6 folds reduction. Calculated viscosities and slip lengths are given in Table 5.1. Viscosity and slip length results for the uncharged case match well with the data presented in the literature obtained using NEMD and Green-Kubo calculations[34, 47-49, 98-99]. Also calculated viscosity for the uncharged case matches well with the thermodynamic viscosity of water at 300 K (μ_{td} = 855 µPa.s). In Table 5.1, we also present the standard error (SE) values of the slip lengths obtained from 10 independent samples (n) using $SE = S/\sqrt{n}$, where S is the standard deviation. We used 80 consecutive time-averaged data sets to obtain each independent sample. The standard errors in the slip lengths were found in the range of 0.09 to 0.6 for varied surface charge densities.
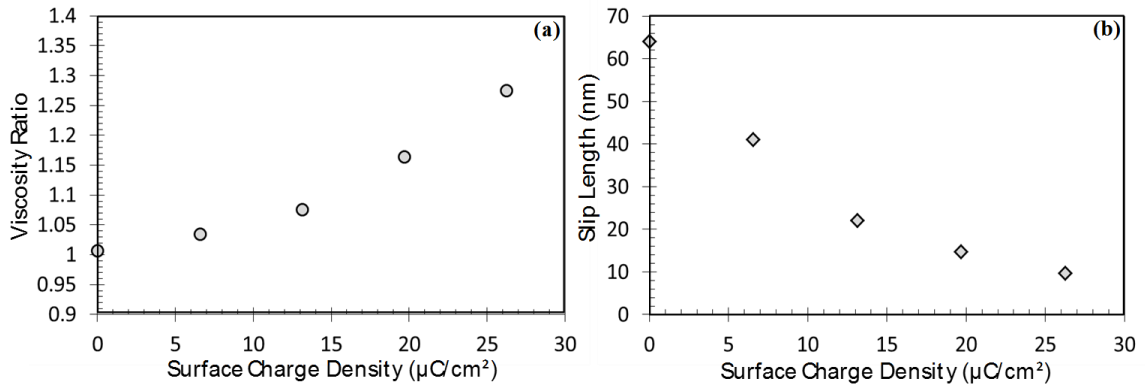
Fig. 5.8 Variation of the viscosity ratio (µ/µtd) and the slip length as a function of the surface charge density.

Decreased slip lengths and increased viscosity due to the surface charge greatly reduces the volumetric flow rate in the channel. In order to obtain speeds suitable for statistical analysis we increased the driving force applied on each atom for the increased

surface charge cases. The driving forces (f) and the resulting volumetric flow rates ($\dot{Q}_{MD}$) are also presented in Table 5.1. Since the volumetric flow rate is linearly dependent on the driving force, different surface charge cases can be compared with each other using normalized flow rate. First, we divide volumetric flow rate by the driving force to obtain $\dot{q}_{MD} = \dot{Q}_{MD}/f$. Normalizing $\dot{q}_{MD}$ data with the value of the electrically neutral case, we obtained $\dot{q}_{MD}^*$. Fig. 5.9 shows variation of $\dot{q}_{MD}^*$ as a function of the surface charge density. As can be seen in the figure, the normalized volumetric flow rate is reduced to 13.2% of the neutral graphene channel for the 26.24 µC/cm^2 case. Theoretical prediction of the volumetric flow rate based on continuum equations is given by

$$\dot{Q}_T = \frac{f h_e^3 w}{12 \mu} (1 + 6 \beta^*) \tag{5.2}$$

Volumetric flow rates predicted by Eq. (5.2) are also given in Table 5.1 using the MD calculated slip lengths and viscosities. Normalizing the flow rate for all charged surface cases ($\dot{Q}_{T\sigma}$) with the electrically neutral case $\dot{Q}_{Tn}$ under constant driving force f gives

$$\dot{q}_T^* = \frac{\dot{Q}_{T\sigma}}{\dot{Q}_{Tn}} = \left(\frac{\mu_n}{\mu_\sigma}\right)\left(\frac{1 + 6\beta_\sigma^*}{1 + 6\beta_n^*}\right) \tag{5.3}$$

where the subscripts σ and n show the electrically charged and neutral cases, respectively. Using the slip length and viscosity data reported in Table 5.1, we present in Fig. 5.9 the predictions of Eq.(5.3) using dashed line. Good match between the normalized MD data and Eq. (5.3) are observed. It is important to indicate that this match does not imply the validity of continuum equations for 4nm height graphene channel. Comparison of the continuum predicted, and MD calculated volumetric flow rates in

Table 5.1 show up to 5.5% difference due to the scale effects. The reasons of these deviations and a phenomenological continuum model appropriate for these length-scales were previously described in [18].

Table 5.1. Transport parameters at different surface charges. MD measured volumetric flowrate ($\dot{Q}_{MD}$) compared with theoretical predictions from Eq. (5.2) using the viscosity and slip lengths calculated by MD ($\dot{Q}_T$); and normalized MD flowrate ($\dot{q}^*_{MD}$) and theoretical flowrate ($\dot{q}^*_T$) from Eq. (5.3).

Surface Charge (μC/cm^2)	Viscosity (μPa.s)	Slip Length (nm)	Driving Force (N)	β^*	$\dot{Q}_{MD}$ (m^3/s)	$\dot{Q}_T$ (m^3/s)	$\dot{q}^*_{MD}$	$\dot{q}^*_T$
26.24	1103.1	9.68±0.09	2.07×10^{-10}	2.79	8.86×10^{-16}	8.41×10^{-16}	0.132	0.126
19.68	1001.7	14.8±0.2	1.25×10^{-10}	4.26	8.77×10^{-16}	8.29×10^{-16}	0.217	0.211
13.12	926.7	22.1±0.4	6.70×10^{-11}	6.35	7.44×10^{-16}	7.06×10^{-16}	0.342	0.338
6.56	886.3	41.5±0.6	3.05×10^{-11}	11.9	6.23×10^{-16}	6.18×10^{-16}	0.631	0.627
0	863.4	64.1±0.6	2.74×10^{-11}	18.4	8.88×10^{-16}	8.66×10^{-16}	1	1

5.5 Conclusion

Force-driven water flows in graphene nanochannels with positive surface charges are investigated using MD simulations. Frequently-used Ewald summation algorithms exhibit non-physical behavior due to the finite electric charge in the simulations. We overcome this difficulty by using a Coulomb force cut-off length equal to the simulated system size. Surface charge alters the surface wetting and transport characteristics of water in the channel. Basically, electrostatic forces contribute to water layering near the surface and further develop a preferred alignment of dipolar water molecules in the near surface region. An increase in charge density increases the water-density peaks and brings them closer to the interface, while more water molecules orient their dipoles
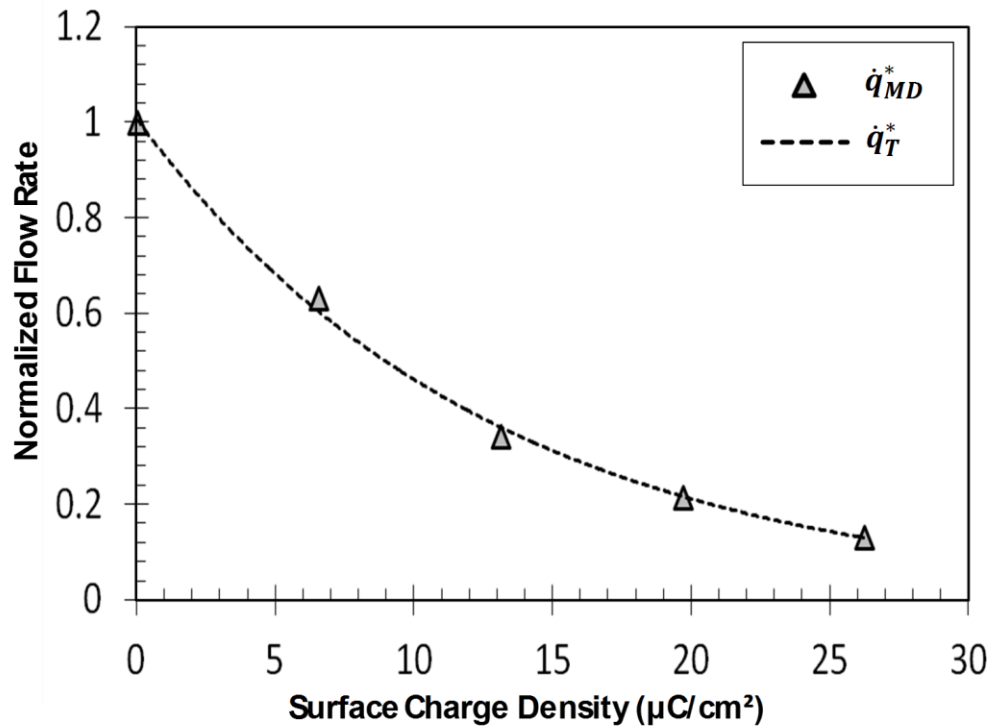
Fig. 5.9 Normalized MD volumetric flow rate and normalized theoretical flow rate Eq. (5.4) as a function of the surface charge density.

opposite to the surface in case of a positive surface charge. As a result, force-driven flows exhibit increased water viscosity and decreased slip lengths. For example, the slip-length of water on graphene surfaces at $\sigma=26.24$ $\mu C/cm^2$ is 6.6 times smaller than that of the electrically neutral surfaces, and the water viscosity increases nearly 29% from its thermodynamic value. Volumetric flow rates present the overall influence of surface charge on the water transport. With the increase in surface charge, flow rate is reduced to almost 13.2% of the neutral graphene channel for the $\sigma=26.24$ $\mu C/cm^2$ case. We theoretically predict flow rates using MD calculated viscosity and slip values and a continuum model based on the effective channel height with 0.8-5.5% error. Overall, the results show reduced transport inside charged graphitic surfaces, which is an undesired outcome for charged surface nanomembrane applications. For example, the applied

electric charge used to separate ionic species can substantially decrease the flow rate. These findings are important for optimization of selective ion transport nanochannels and membranes.

Chapter 6

MOLECULAR AND CONTINUUM TRANSPORT PERSPECTIVES ON
ELECTROOSMOTIC SLIP FLOWS

6.1 Introduction

Liquid transport in micro/nanoscale systems is of fundamental importance and have

a vast array of applications spanning from water desalination[5] to drug delivery[4]

micro/nanopumping[186] and energy storage[187]. Transport in these scales can be induced

using external means such as electric fields, pressure, temperature and concentration

gradients. Electroosmotic flow is the motion of ionized fluids under externally applied

electric fields. It is caused by the ionic charge distribution within the electric double layer

(EDL), where the counter-ions that dominate the diffuse-layer move due to the external

electric field and drag fluid molecules with them. For most practical purposes, EDL

thickness varies between 100 nm for deionized water to ~1nm in high conductivity

solutions. Therefore, electroosmosis is a nanoscale-induced transport phenomenon that

creates EOF in nano and micro-channels. The volumetric flow rate for EOF between two

parallel plates varies linearly with the channel height, while the flow rate in pressure-

driven flows scale with cube of the channel height. This behavior allows practical flow

rates in micro- and nanoscale applications using relatively low electric fields instead of

unrealistically large pressure drops[56]. EOF imposed by locally applied

electric fields also eliminates the need of pumping and valving with moving mechanical components[188].

Presence of charged surfaces and salt ions in EOF may significantly alter the transport properties such as viscosity and slip length in nanochannels, and predictions based on the continuum transport theory may become inaccurate with reduced channel dimensions. The effects of surface charge were previously investigated in terms of surface wettability and wetting kinetics[180]. With increased surface charge, the number of molecules at the interface increases due to the stronger wall force field effect, which enhances the surface wettability[136]. Increase of surface charge also significantly changes the orientation of water molecules and the dynamics of hydrogen bonding. For such cases, hydrogen bonds form more frequently without breaking, restricting the degree of freedom of water molecules near the charged surface. This results in enhancement of water viscosity in nanoscale confinements[38]. In multiple studies, Qiao and Aluru[37, 189] showed local viscosity variations of water through nanochannels on positively and negatively charged surfaces. Accordingly, slip length reduces with increased surface charge due to the stronger liquid-solid coupling at the interface, which implies a larger interfacial resistance[190]. In our previous studies, we investigated deionized water flow through charged graphene nanochannels, and have shown that slip length is decreased, while the apparent viscosity is increased with surface charge[23, 33]. Furthermore, hydration of salt ions in an electrolyte may affect the liquid transport[191]. As the number of water molecules bound to an ion increases, the hydrogen bond population increases and the number of surrounding free water molecules reduces[192]. This inhibits the motion of liquid molecules relative to each other, and results in increased viscosity[40]. In a recent study,

Bhadauria and Aluru[59] presented a multi-scale transport model for EOF in nanoscale channels. In this model, they investigated the effects of interfacial friction coefficient and spatially varying solvent viscosity due to the charged wall and ion distributions in EOF.

Analytical models of EOF are based on the solution of Poisson-Boltzmann (PB) and Stokes (S) equations. Continuum approaches assume ionic solution as continuous media with constant viscosity, and mostly impose no-slip condition on the walls. Density layering at the solid-water interface, finite sizes of the molecules, exact location of the wall and the hydrodynamic slip-plane are usually neglected. Joly *et al.*[58] solved EOF using Navier-type slip condition within linearized PB description and have defined a slip-enhanced zeta potential. Tendon and Kirby[193] also discussed the role of hydrodynamic slip on the zeta-potential for hydrophobic microfluidic systems, where they provided a similar analytical solution. Furthermore, Ren and Stein[194] analytically showed the impact of slip length in nanochannels for both pressure-driven flow and EOF using non-linear PB model. In an experimental study, Bouzigues *et al.*[195] measured EOF in both hydrophilic glass and hydrophobic octadecyl-trichloro-silane (OTS) coated glass channels using nanoscale particle velocimetry (nanoPIV) technique, and have shown slip-enhanced velocity profiles in the hydrophobic system. They also compared the experimental results with slip-modified analytical predictions. Another experimental study focused on flow rate measurements in hydrophilic silica and hydrophobic OTS-silanized glass channels, where flowrate enhancement in the hydrophobic case was shown[196].

Dielectric materials in contact with an electrolyte solution naturally acquire surface charges that depend on the ionic concentration, pH of the solution, and surface

112

chemistry[132]. Behavior of the EDL and the resulting EOF can be greatly affected by the surface charge density (σ). The PB-S model gives reasonable predictions of the EDL structure and the resulting EOF for $\sigma < 0.15$ C/m^2 [62]. Experimental studies[197-198] in silica channels conducted using multivalent ionic solutions at high concentrations exhibited higher surface charge densities and resulted in charge inversion phenomenon, which cannot be predicted using the PB theory[199]. Using molecular dynamics, Qiao and Aluru[45] investigated EOF in silicon nanochannels and have shown discrepancies in the ion-distribution between MD results and PB equations. Lorenz *et al.*[63] investigated salt concentration effects on EOF using MD simulations in silica nanochannels with properly modeled silanol groups. Several MD studies in the literature show charge inversion and electroosmotic flow reversal at large surface charge densities[62, 65, 200]. The charge inversion phenomenon is induced by excessive adsorption of counter-ions at Stern layer, where it exceeds the value of the surface charge. This leads to a larger co-ion charge density than the counter-ion charge density in the diffuse layer[199]. As a result of sign inversion in the charge distribution of the diffuse layer, a reversed EOF develops in the channel under an applied electric field. This reversed EOF velocity increases with increased surface charge density[62]. Although it is important to acknowledge the limitations of the PB-S model, many practical applications of EOF occur in low surface charge density regime, where the PB-S model is still valid.

Very limited number of studies in the literature focuses on the nanoscale electrokinetic transport phenomenon from continuum point of view. In this study, we systematically investigate the effects of slip length and viscosity enhancements on nanoscale EOF. Our main objective is to show that well-known continuum transport

model accurately predicts the electroosmotic velocity profiles in nanochannels using the slip length and viscosity values obtained from force-driven nanochannel flow simulations performed at various liquid-wall interaction strengths. In this regard, we first present the distribution of surface charge density and corresponding zeta potential as a function of ionic conditions, solution pH and surface reactions. We particularly used electro-chemical conditions where PB-S equations are still applicable. Then, we present the results of density profiles and ion distributions by equilibrium MD simulations, ensuring that the desired thermodynamic state and ionic conditions are reached. Next, we perform force-driven flow simulations to determine the viscosity and slip length for ionic fluids in charged channels. Using these results, we finally predict electroosmotic velocity profiles based on continuum theory and compare these velocity profiles with the results of MD simulations. We also develop a relation between the ion mobilities and diffusivities, and verify MD results using known ion diffusivities.

6.2 Theoretical Background: Governing Equations in Electrokinetic Theory

A good description of an electrokinetic system requires governing equations for the electrokinetic potential (ψ), local bulk fluid velocity (u) and ionic concentrations (c_i). The mean field approximation of the electrokinetic potential is described by the Poisson's equation, which relates the electrokinetic potential to the net charge density. Fluid motion is described by the Navier-Stokes equations which are well-known formulations derived from conservation of linear momentum. In electrokinetic theory, the fluid flow is driven due to the electrical force in the system, adding a body force term to the momentum equation. Finally, local ionic species concentration is introduced by Nernst-Planck equation, where it fundamentally describes the influence of an ionic concentration

gradient by conservation of mass equation. These continuum equations are strongly coupled to each other as illustrated in Fig. 6.1. In this study, we are interested in electroosmotic slip flows through nanoscale confinements. As a result, our considerations in this study mainly focus on velocity slip in electroosmotic flow by using analytical solution of the Poisson-Boltzmann and Stokes equations with slip correction.
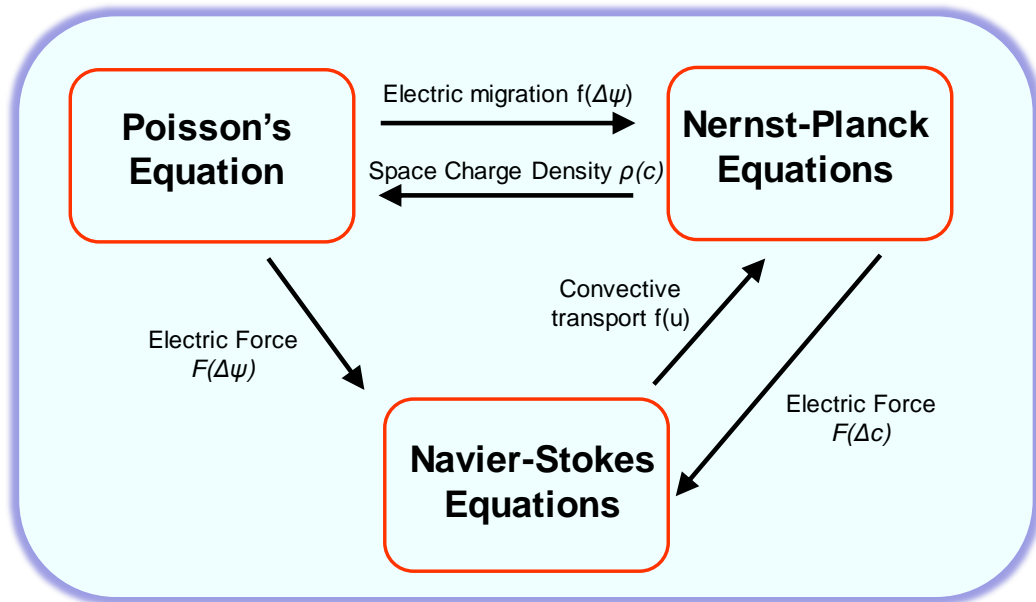
Fig. 6.1 Governing equations in electrokinetic theory.

6.2.1 Poisson's Equation

Electrical or electrokinetic potential (ψ) is defined as the work required moving a unit point charge (q) from a reference point to another point in the space, where this work is done by an electrical force ($\bar{F}_{el}$). The electrical force on a point charge is given by

$$\bar{F}_{el} = q\bar{E} \tag{6.1}$$

where $\bar{E}$ is the electric field caused by the point charge. The electric field is the gradient of the electric potential as

$$\bar{E} = -\nabla\psi \tag{6.2}$$

Based on Gauss's law for electrostatics, the electric field flux due to the point charges can be integrated over a closed surface (S)

$$\int_S \varepsilon\bar{E} \cdot \hat{n}\, dA = \sum q \tag{6.3}$$

where ε is the permittivity of the surface, $\sum q$ is the sum of the charges, $\hat{n}$ is the unit normal vector along the surface and dA is the differential area along this surface. Applying the divergence theorem, this integral can be given in differential form as follows

$$\nabla \cdot \varepsilon\bar{E} = \rho_e \tag{6.4}$$

where ρ_e is the net electrical charge density in the unit of C/m^3. Relating the Gauss's law of electrostatics to the gradient of electrical potential, we obtain Poisson's equation which is given by

$$\nabla \cdot \varepsilon(-\nabla\psi) = \rho_e \tag{6.5}$$

Considering a uniform, linear, homogenous and isotropic medium with electrical permittivity (ε), which can be represented by product of the relative permittivity of the medium (ε_r) and the vacuum permittivity (ε_0). Final form of the Poisson's equation for the electric potential is given by

$$\nabla^2\psi = -\frac{\rho_e}{\varepsilon_0\varepsilon_r} \tag{6.6}$$

In the assumption of net electrical charge is equal to zero (i.e. dielectric material), Poisson's equation becomes Laplace equation

$$\nabla^2\psi = 0 \tag{6.7}$$

116

Electrokinetic theory defines the net charge density of electrolyte solutions in diffuse layer, which is expressed by Faraday equation as follows

$$\rho_e = F \sum_i v_i c_i \tag{6.8}$$

where v is the valance, c is the molar concentration, the subscript i indicates the ith species, and F is the Faraday's constant. Eq. (6.8) shows that the net electrical charge density is a function of ionic concentration ($\rho_e(c_i)$), explaining how Poisson's equation is coupled with the Nernst-Planck equations for charged species transport.

➢ **Poisson-Boltzmann Equation**

In statistical mechanics, Boltzmann Distribution predicts the probability of a particular state of a system for a given temperature and energy. The ion concentration can be described by the Boltzmann distribution as

$$c_i = c_{i0} e^{-\frac{\Delta E}{RT}} \tag{6.9}$$

where c_{i0} is the bulk ionic concentration, T is the absolute temperature, R is the universal gas constant, and ΔE is the required work to move an ion to the surface from an infinite distance ($\Delta E = F v_i \psi$). Net electrical charge density inside the diffuse layer is

$$\rho_e = \sum_i v_i c_{i0} F exp\left(-\frac{v_i F \psi}{RT}\right) \tag{6.10}$$

Combining this equation with Poisson equation given in Eq. (6.6), we obtain the Poisson-Boltzmann equation for electrokinetic potential given by

$$\nabla^2 \psi = -\frac{F}{\varepsilon_0 \varepsilon_r}\left[\sum_{i=1}^{N} v_i c_{i0} exp\left(-\frac{v_i F \psi}{RT}\right)\right] \tag{6.11}$$

Poisson–Boltzmann equation is a nonlinear equation which is difficult to solve analytically due to the summation of the charge density terms and due to their strongly nonlinear character[201]. Considering a symmetric electrolyte with equal valence ($v_1 = v_2 = v$) in equilibrium on charged surface, PB equation can be expressed as

$$\nabla^2\psi = \frac{Fvc_0}{\varepsilon_0\varepsilon_r}sinh\left(\frac{Fv\psi}{RT}\right) \tag{6.12}$$

For simplification, electrokinetic potential is normalized by the zeta potential (ζ) as $\psi^* = \psi/\zeta$ and an ionic energy parameter (α) is defined as $\alpha = Fv\zeta/RT$. A variable Ω relates the ionic energy parameter and the characteristic half channel length h to the Debye-Hückel parameter (ω).

$$\Omega = \frac{(\omega h)^2}{\alpha} \tag{6.13}$$

The EDL thickness of an ionic solution on a charged surface is determined by Debye-Hückel parameter or Debye length (λ_D) given by

$$\omega = \frac{1}{\lambda_D} = \sqrt{\frac{\sum_{i=1}^{N}v_i^2F^2c_{i0}}{\varepsilon_0\varepsilon_rRT}} \tag{6.14}$$

A simplified non-dimensional hyperbolic sinusoidal form of Poisson-Boltzmann equation in 1D can be obtained as follows

$$\frac{d^2\psi^*}{d\eta^2} = \Omega sinh(\alpha\psi^*) \tag{6.15}$$

where $\eta = z/h$ is the distance from the channel center. Boundary conditions are

At $z = 0 \rightarrow \eta = 0$

$$\psi = 0 \text{ and } \psi^*{}_c = 0$$

At $z = h \rightarrow \eta = 1$

$$\psi = \zeta \text{ and } \psi^*_w = 1$$

First integration of the Poisson-Boltzmann equation between channel center and an arbitrary point gives

$$\frac{d\psi^*}{d\eta} = \sqrt{\frac{\Omega}{\alpha}} \, [2\cosh(\alpha\psi^*) - 2\cosh(\alpha\psi^*_c)]^{1/2} = \sqrt{\frac{\Omega}{\alpha}} \, [2\cosh(\alpha\psi^*) - 2]^{1/2} \quad (6.16)$$

Using half argument formulas for $\cosh(x) = 2\sinh^2\left(\frac{x}{2}\right) + 1$, spatial derivative of electrokinetic potential becomes

$$\frac{d\psi^*}{d\eta} = 2\sqrt{\frac{\Omega}{\alpha}} \, \sinh\left(\frac{\alpha\psi^*}{2}\right) \quad (6.17)$$

Reconfiguring Eq. (6.17) gives

$$d\eta = \frac{1}{2}\sqrt{\frac{\alpha}{\Omega}} \, \frac{d\psi^*}{\sinh\left(\frac{\alpha\psi^*}{2}\right)} \quad (6.18)$$

Integrating this equation, we obtain

$$\eta = \frac{1}{\sqrt{\alpha\Omega}} \ln\left[\tanh\left(\frac{\alpha\psi^*}{4}\right)\right] + C_1 \quad (6.19)$$

Using the boundary conditions $\psi^* = 1$ at the wall, the coefficient C_1 becomes

$$C_1 = 1 - \frac{1}{\sqrt{\alpha\Omega}} \ln\left[\tanh\left(\frac{\alpha}{4}\right)\right] \quad (6.20)$$

and

$$\eta = \frac{1}{\sqrt{\alpha\Omega}} \ln\left[\tanh\left(\frac{\alpha\psi^*}{4}\right)\right] + 1 - \frac{1}{\sqrt{\alpha\Omega}} \ln\left[\tanh\left(\frac{\alpha}{4}\right)\right] \quad (6.21)$$

Using $\eta^* = 1 - \eta$ is the distance from the wall

$$\eta^* = -\frac{1}{\sqrt{\alpha\Omega}} \ln\left[\frac{\tanh\left(\frac{\alpha\psi^*}{4}\right)}{\tanh\left(\frac{\alpha}{4}\right)}\right] \quad (6.22)$$

Using this equation, electrokinetic potential in non-dimensional form is

$$\psi^*(\eta^*) = \frac{4}{\alpha}\left[tanh^{-1}\left[tanh\left(\frac{\alpha}{4}\right)exp(-\sqrt{\alpha\Omega}\eta^*)\right]\right] \qquad (6.23)$$

Fist derivative of the electrokinetic potential in non-dimensional form is given by

$$\frac{d\psi^*}{d\eta^*} = \frac{4}{\alpha}\left[\frac{\sqrt{\alpha\Omega}\,tanh\left(\frac{\alpha}{4}\right)exp(-\sqrt{\alpha\Omega}\eta^*)}{tanh^2\left(\frac{\alpha}{4}\right)exp(-2\sqrt{\alpha\Omega}\eta^*) - 1}\right] \qquad (6.24)$$

In dimensional form, first derivative of the electrokinetic potential becomes

$$\frac{d\psi}{dz} = \frac{4\zeta}{\alpha}\left[\frac{\omega\,tanh\left(\frac{\zeta}{\alpha}\right)exp(-\omega z)}{tanh^2\left(\frac{4\zeta}{\alpha}\right)exp(-2\omega z) - 1}\right] \qquad (6.25)$$

Electrokinetic potential in dimensional form is given as

$$\psi = \frac{4\zeta}{\alpha}\left[tanh^{-1}\left[tanh\left(\frac{\zeta}{\alpha}\right)exp(-\omega z)\right]\right] \qquad (6.26)$$

Using inverse hyperbolic tangent formulation as $tanh^{-1}(x) = \frac{1}{2}ln\left(\frac{1+x}{1-x}\right)$, the final

form of the electrokinetic potential can also be reconfigured as

$$\psi = \frac{2RT}{Fv}ln\left[\frac{1 + exp(-\omega z)\,tanh(\frac{Fv\zeta}{4RT})}{1 - exp(-\omega z)\,tanh(\frac{Fv\zeta}{4RT})}\right] \qquad (6.27)$$

6.2.2 Navier-Stokes Equations

Electroosmotic velocity profiles require solution of PB equation at a specified zeta

potential on the walls. Navier-Stokes equation for an incompressible and Newtonian fluid

is given by

$$\rho\left(\frac{\partial\bar{V}}{\partial t} + (\bar{V}\cdot\nabla)\bar{V}\right) = -\nabla P + \mu\nabla^2\bar{V} + \overline{fe} \qquad (6.28)$$

where $\bar{V}$ is the fluid velocity vector, ∇P is the pressure gradient, μ is the dynamic

viscosity of the solution and $\overline{fe}$ is the external body force by electric field. For a steady,

fully developed and electroosmotic flow in absence of pressure gradients, momentum

equation in the stream-wise direction is reduced to

$$\frac{d^2 u}{dz^2} = -\frac{\rho_e}{\mu} E_x \tag{6.29}$$

where u is the stream-wise velocity and E_x is the applied electric field in x-direction.

Herein, the fluid motion is a function of net charge density which is determined by the

species concentration. Therefore, Navier-Stokes equation is coupled with both Poisson's

equation and Nernst-Planck equations. For 1D case, this coupling is trivial. Furthermore,

Navier-Stokes equation in the absence of convection term and pressure gradient become

Poisson's equation itself and can be reorganized as follows

$$\frac{d^2 u}{dz^2} = \frac{\varepsilon_0 \varepsilon_r}{\mu} E_x \frac{d\psi^2}{dz^2} \tag{6.30}$$

First integration of this equation with respect to z gives the velocity gradient,

$$\frac{du}{dz} = \frac{\varepsilon_0 \varepsilon_r}{\mu} E_x \frac{d\psi}{dz} + C_1 \tag{6.31}$$

Second integration with respect to z gives the velocity profile

$$u(z) = \frac{\varepsilon_0 \varepsilon_r}{\mu} E_x \psi(z) + C_1 z + C_2 \tag{6.32}$$

Boundary conditions for EOF in a nanochannel considers velocity slip at the liquid-

solid interface ($z=0$ and $z=h$) described by the following Navier-type slip condition

$$u_l - u_w = \beta \frac{du}{dz} \tag{6.33}$$

where β, u_l and u_w are the slip length, liquid and wall velocities, respectively. Additionally, symmetry can be imposed at the channel center ($du/dz = d\psi/dz = 0$).

At $z = h/2$

$$\psi = 0 \text{ and } \frac{du}{dz} = 0 \ \rightarrow \ C_1 = 0$$

At $z = 0$

$$u(0) = \beta \frac{du}{dz}\bigg|_{z=0} \ \rightarrow \ C_2 = \frac{\varepsilon_0 \varepsilon_r}{\mu} E_x \left(\beta \frac{d\psi}{dz}\bigg|_{z=0} - \zeta \right)$$

Solution of Eq. (6.32) with a Navier-type slip condition results in the following velocity profile

$$u(z) = \frac{\varepsilon_0 \varepsilon_r}{\mu} E_x \left[\psi(z) - \zeta + \beta \frac{d\psi}{dz}\bigg|_{z=0} \right] \tag{6.34}$$

where the above equation is reconfigured by substituting electrokinetic potential equation given in Eq. (6.27) and its first derivative on the walls ($z=0$) given in Eq. (6.25), the velocity distribution between $z=0$ and $z=h/2$ becomes

$$u(z) = u_{HS} \left\{ 1 - \frac{4}{\alpha} \left[tanh^{-1}\left(tanh\left(\frac{\alpha}{4}\right) exp(-\omega z) \right) - \frac{\beta}{\lambda_D}\left(\frac{tanh\left(\frac{\alpha}{4}\right)}{1 - tanh^2\left(\frac{\alpha}{4}\right)} \right) \right] \right\} \tag{6.35}$$

where u_{HS} is the Helmholtz Smoluchowski velocity given by

$$u_{HS} = -\frac{\varepsilon_0 \varepsilon_r \zeta}{\mu} E_x \tag{6.36}$$

Velocity profile in the entire channel is obtained by combining Eq. (6.35) with its symmetric extension from the channel center, and it is valid for non-overlapping EDL cases. In absence of slip, velocity profile starts from zero at the wall and rapidly increases to 99% of u_{HS} approximately $4.5\lambda_D$ from the surface[202]. However, velocity slip amplifies the final velocity attained after the EDL region significantly. Ratio of the bulk flow

velocity with slip ($u_{HS\,Slip}$) normalized with the no-slip Helmholtz Smoluchowski velocity is given by

$$\frac{u_{HS\,Slip}}{u_{HS}} = 1 + \frac{4}{\alpha}\frac{\beta}{\lambda_D}\left(\frac{tanh\left(\frac{\alpha}{4}\right)}{1 - tanh^2\left(\frac{\alpha}{4}\right)}\right) \tag{6.37}$$

The most important aspect of this behavior is that the slip length β is normalized by the Debye length λ_D. Therefore, the slip contributions are *independent* of the channel height and determined by α, β and λ_D. This is a fundamentally different behavior from force-driven flows, where slip contributions are normalized by the channel height, whose effects diminish in larger channels[55]. In Eq. (6.37), $\alpha = 1$ is obtained for $|\zeta|$=25.4 mV and T=20°C, and $\alpha \le 6$ for most practical applications; therefore, $tanh$ term in the denominator does not create any singularities. Electroosmotic slip flows were investigated before by mostly using Debye-Hückel linearization, leading to simplified versions of Eqs. (6.35) and (6.37), strictly valid for $\alpha \le 1$ cases[190]. Slip length β is a function of the liquid-wall interactions, which is maximized for hydrophobic surfaces or by using polymeric coating[195]. Meanwhile, the Debye length is a function of the ionic conductivity. For example, λ_D≈100 nm for deionized water, while $\lambda_D = 0.3$ nm for 1M NaCl solution. It is theoretically possible to observe slip enhanced EOF in nano and micro-channels by first choosing a hydrophobic channel with large β, and then by increasing the ionic concentration to reduce λ_D. However, regulating the normalized slip length by reducing λ_D requires using high conductivity solutions, which exhibit overwhelming Joule heating[203], electrode polarization effects[204] and strong Faradaic reactions[205].

6.2.3 Prediction of Surface Charge Density and Zeta Potential

For a given electrolyte and surface pair, electro-chemical properties, such as the surface charge and zeta potential are related to each other as a function of the ionic concentration, pH of the solution and physiochemistry of the surface[132]. These electrochemical properties must be specified either based on the actual conditions observed in experiments or determined using the Poisson-Boltzmann-Nernst-Planck (PBNP) equations. Comprehensive studies in formulating these complex relations using PBNP equations were reported in the literature[206-207].

The surface charge naturally occurs at the boundary when a dielectric material is in contact with an electrolyte solution. It is mainly due to the protonation/deprotonation mechanisms of the functional group at the liquid-wall interface, introducing a charge regulated nature of dielectric material[132, 208]. Thus, surface charge is regulated depending on the solution properties such as pH and ionic concentration as well as geometry and physicochemical properties of the dielectric surface[206]. It is imperative to know that the number of protonation/deprotonation reactions (so the number of equilibrium constants) vary for different dielectric materials. For a semi-infinite flat dielectric substrate made of silica as shown in Fig. 6.2 , two chemical reactions in silanol functional groups[206] are given by

$$SiOH \leftrightarrow SiO^- + H^+ \tag{6.38}$$

and

$$SiOH + H^+ \leftrightarrow SiOH_2{}^+ \tag{6.39}$$

The reaction equilibrium constants (K_A and K_B) are

$$K_A = \frac{N_{SiO^-}[H^+]_S}{N_{SiOH}} \quad \text{and} \quad K_B = \frac{N_{SiOH_2{}^+}}{N_{SiOH}[H^+]_S} \tag{6.40}$$

where N_{SiOH}, N_{SiO^-}, and $N_{SiOH_2^+}$ are surface site densities of SiOH, SiO$^-$ and SiOH$_2^+$, respectively. Here, $[H^+]_S$ refers to the concentration of H$^+$ ions at liquid-solid interface and is governed by the Boltzmann distribution as $[H^+]_S = [H^+]_0 exp\left(-\frac{F\zeta}{RT}\right)$. Note that $[H^+]_0$ is related to the pH of the bulk liquid by $pH = log([H^+]_0)$. The total number site density of silanol groups are expressed as

$$N_{Total} = N_{SiOH} + N_{SiO^-} + N_{SiOH_2^+} \tag{6.41}$$

The surface charge density is the difference between positive and negative functional groups at the interface given by $\sigma_s = -F(N_{SiO^-} - N_{SiOH_2^+})$, related to Eqs. (6.40) and (6.41) which gives following formulation

$$\sigma_s = -FN_{tot}\left[\frac{K_A - K_B\left[[H^+]_0 exp\left(-\frac{F\zeta}{RT}\right)\right]^2}{K_A + [H^+]_0 exp\left(-\frac{F\zeta}{RT}\right) + K_B\left[[H^+]_0 exp\left(-\frac{F\zeta}{RT}\right)\right]^2}\right] \tag{6.42}$$

The surface charge density is determined by the electrical potential difference between the electrolyte solution and dielectric substance with a thickness of d and dielectric constant of ε_d, which is given by

$$\varepsilon_0\varepsilon_r \frac{d\psi}{dz} - \varepsilon_0\varepsilon_d \frac{d\phi}{dz} = -\sigma_s \tag{6.43}$$

in the above equation, electric potential within the ionic aqueous solution (ψ) is described by the Poisson-Boltzmann equation given in Eq. (6.27). Electric potential inside flat dielectric wall (ϕ) connected to a constant gate potential (V_g) is given by Laplace equation as follows

$$\frac{d\phi^2}{dz^2} = 0 \rightarrow \phi = Az + B \tag{6.45}$$

Boundary conditions are $\phi = V_g$ at the gate electrode ($z = d$) and $\phi = \zeta$ at the interface ($z = 0$).

$$\phi = (\zeta - V_g)\left(\frac{z}{d}\right) \tag{6.45}$$

Combining Eqs. (6.42), (6.43) and (6.45), following implicit equation is used to determine the zeta potential

$$\frac{2\varepsilon_0\varepsilon_r\omega RT}{Fv}\sinh\left(\frac{Fv\zeta}{2RT}\right) + \varepsilon_0\varepsilon_d\left(\frac{\zeta - V_g}{d}\right)$$

$$= -FN_{tot}\left[\frac{K_A - K_B\left[[H^+]_0 exp\left(-\frac{F\zeta}{RT}\right)\right]^2}{K_A + [H^+]_0 exp\left(-\frac{F\zeta}{RT}\right) + K_B\left[[H^+]_0 exp\left(-\frac{F\zeta}{RT}\right)\right]^2}\right] \tag{6.46}$$

In triple layer model, the liquid is treated as incompressible and flow is considered in creeping regime which typically refers to Reynolds numbers smaller than 1. Secondly, effect of the Stern layer near the wall is ignored so that the electric potential at the interface is associated with the zeta potential of the planar surface. In addition, no EDL overlapping is observed across the channel. The solutions are simplified to one-dimension, which is perpendicular to the channel wall.

The analytical calculations of surface charge density and corresponding zeta potential are also verified using a commercial finite element package, COMSOL Multiphysics (COMSOL AB, Stockholm, Sweden). Physical constants used in analytical calculations and numerical simulations are $\varepsilon_0 = 8.854 \times 10^{-12}$ F/m, $\varepsilon_r = 78$, $R = 8.314$ J/(mol K), $T = 300$ K, $F = 96490$ C/mol. Monovalent NaCl electrolyte solution with $v = 1$. Total surface group concentrations and surface reaction constants of silica surface for $V_g = 0$ are $N_{Total} = 1.3266 \times 10^{-5}$ and $pK_A = -logK_A = 7.6$ and $pK_B = -logK_B = 1.9$, respectively[207]. The diffusion coefficients of ions in this solutions for

Na$^+$, Cl$^-$, H$^+$ and OH$^-$ are 13.3 x 10^{-6}, 20.1 x 10^{-6}, 93.1 x 10^{-6} and 52.7 x 10^{-6} cm^2/s, respectively[209].
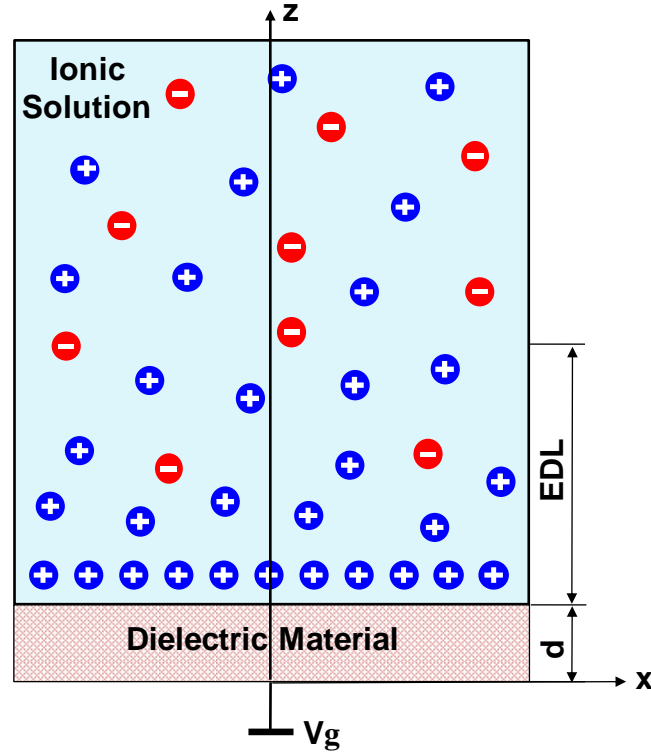
Fig. 6.2 Schematic representation of semi-infinite silica wall in contact to ionic solution.

6.3 Molecular Dynamics Simulation Details

We perform MD simulations on a three-dimensional system consisting of aqueous NaCl solution confined between two parallel silicon walls. Fig. 6.3 shows an illustration of the simulation domain. The total dimensions of the simulation domain in x- and y-directions are 4.66×4.61 nm, respectively. The channel height is h=3.49 nm. We specifically picked this channel height so that continuum transport theory with a bulk flow region is still applicable. For much narrower channels, definitions of the thermodynamic state and continuum variables such as density, velocity and viscosity may become irrelevant. Previous studies showed that continuum predictions can hold up to

channel heights of 2-3 nm[14, 18, 45]. In addition, this channel height avoids EDL overlap at the specified ionic concentration and surface charge density, while exhibiting nearly equal bulk and liquid-solid interface regions.
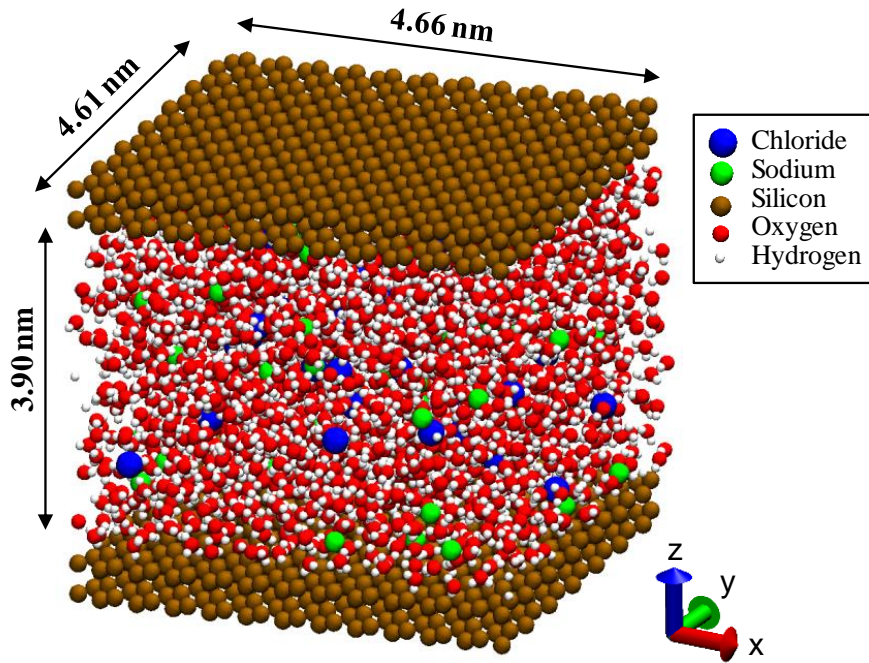
Fig. 6.3 Snapshot of the simulation domain.

Each solid wall contains four layers of silicon atoms organized in <111> direction. We constrain the wall atoms at their original positions to maintain a cold wall behavior, while remaining particles inside the simulation box are free to move. The innermost layers of each wall are assigned a negative surface charge by uniformly distributing a single point charge to each silicon atom. All other wall layers are electrically neutral. In the simulations, wall charges are exactly equal to the net charge difference between counter-ions and co-ions to satisfy the electrical neutrality condition. It should be noted that we use silicon nanochannel to avoid difficulties associated with numerical modeling

of different silanol surface groups (e.g. vicinal, germinal, isolated)[63]. Pure silicon rapidly reacts with oxygen and forms silica, which acquires surface charges when immersed in an ionic solution. In this study, we determined realistic surface charge density considering protonation/deprotonation reactions of silanol groups for a silica surface as a function of environmental parameters such as pH, ionic strength or temperature[208, 210-211]. Electric charges are imposed on silicon surfaces to mimic Coulomb interactions of the charged surface groups on silica.

Intermolecular interactions between all atomic species are calculated using Lennard-Jones (LJ) and Coulomb potentials given in Eq. (3.9). All force field parameters for each atomic species are provided in Table 6.1. Water molecules are modeled using a three-site rigid SPC/E model which adequately reproduces the structural and hydrodynamic properties of water at room temperature[131, 212]. To make water molecules rigid, bond lengths and angles are fixed using SHAKE algorithm[107]. In this study, we only consider oxygen atoms for calculating LJ interactions of water, assuming hydrogen's contribution is negligible because the mass and size of hydrogen is much smaller than the oxygen atom[213]. For electrostatic interactions, both hydrogen and oxygen atoms are modeled as point charges. The interaction parameters of sodium (Na^+) and chloride (Cl^-) are taken from GROMACS force field[214]. The LJ parameters of silicon atoms are taken from Qiao and Aluru[45]. Due to cold-wall assumption, interactions between silicon atoms are excluded. We use Lorentz-Berthelot combination rule to calculate the interactions between dissimilar atoms. In this study, we modify the LJ energy parameter (ε_{Si-O}) between silicon and oxygen atoms to investigate the effect of liquid-solid interaction strength. For this purpose, we use five different wall-liquid

interaction strength ratios $\varepsilon^*/\varepsilon_{Si-O}= 1$, 0.8, 0.5, 0.2 and 0.1, where ε^* is the modified energy parameter of silicon and oxygen.

Table 6.1 Molecular interaction parameters for atomic pairs

Atom	σ (nm)	ε (kj/mol)	q (ē)
O	0.3165	0.6507	-0.848
H	0	0	0.424
Na^+	0.2575	0.0625	1
Cl^-	0.4448	0.4445	-1
Si	0.3385	2.4491	-0.0655

We use Large-Scale Atomic/Molecular Massively Parallel Simulator (LAMMPS) for simulations[105]. Periodicity conditions are applied in x- and y-directions, while the domain is bounded by channel walls in z-direction. Long-range Coulomb interactions between charged particles are calculated using the particle-particle-particle-mesh method with a root-mean-accuracy of 10^{-5}.[109]. To compute the electrostatic interactions in z-direction, a slab modification is applied to the Ewald summation method[146]. A cut-off distance of 1.1 nm is set for all LJ and Coulomb calculations. Verlet algorithm is used to integrate Newton's equations of motion. Before applying any driving force or electric fields, we thermally equilibrate the system using an NVT ensemble. To this end, initial velocities of water molecules and ions are randomly assigned using Gaussian distribution at 300 K. Nose-Hoover thermostat is used to maintain a constant temperature. The system is run for 2 ns using 1fs time steps to reach an equilibrium state without any external forces.

Starting from these equilibrium conditions, we perform non-equilibrium flow simulations. Temperature is fixed at 300 K using a Nose-Hoover thermostat applied only to the degrees of freedoms perpendicular to the flow direction. For force-driven flow simulations, an external force in x-direction is imposed on each particle in the nanochannel based on their masses. EOF is driven by an external electric field applied in x-direction. For flow simulations, the maximum velocities do not exceed 40m/s in order to avoid any non-linear response due to high flow speed[114]. The linear response regime is verified by systematically investigating the average channel velocity with increasing the electric field and driving-force. Addressing this, we choose the electric field strength in the range of 0.1 to 0.25 V/nm and the driving-force per molecule in the range of 5×10^{-5} to 20×10^{-5} eV/Å for various $\varepsilon^*/\varepsilon_{Si-O}$ cases. Such high electric fields will be difficult to use in experimental conditions due to dielectric breakdown of water, but they are required in MD studies to minimize thermal noise[61]. In this study, the time scale for momentum diffusion is calculated using $t_d \approx h^2/v_k$, where h and v_k are the channel height and kinematic viscosity, respectively. Initially, we run each flow simulation for 2 ns ensuring steady flow, which corresponds to $12.5t_d$. Then, for statistical averaging, an additional 16 ns is carried out for force-driven flow simulations while an additional 50 ns is performed for EOF simulations. We use longer averaging time in EOF simulations, which was necessary for proper statistical sampling of relatively low number of Na^+ and Cl^- ions. The results are collected using 200 equally spaced slab-bins in the z-direction, which provides proper resolution of density and velocity profiles.

6.4 Results

EOF requires solution of PB equation with a specified zeta potential while MD simulations of electrokinetic transport require knowledge of the surface charge density. In order to address these requirements, a physical surface charge density and the corresponding zeta potential are determined using Equation 14 and Equation 20 reported in Yeh *et al.*[206], which was derived by considering the protonation/deprotonation reactions of silica. In addition, the surface charge (σ_s) is related to the number of co-ions ($\#_{Co-ions}$) and counter-ions ($\#_{Counter-ions}$) in the solution by

$$\sigma_s = \frac{[\#_{Counter-ions} - \#_{Co-ions}]Q_C}{2A} \tag{6.47}$$

where A is the surface area and Q_C is the electron charge in Coulomb. Excess counter-ions must correspond to the net charge on the walls to satisfy the electrical neutrality condition, while the ionic concentration in the bulk region must satisfy the desired ionic concentration.

In Fig. 6.4, we show the variation of surface charge density and zeta potential as a function of the ionic concentration and pH for NaCl solutions in contact with planar silica surfaces obtained using the methodology reported in Yeh *et al.*[206] At fixed pH, the magnitude of the surface charge density increases and the magnitude of the zeta potential decreases with increased ionic concentration. For a fixed ionic concentration, the magnitudes of both surface charge density and zeta potential increase with increased pH. Given these intrinsic behaviors, the surface charge should not be changed without considering its effects on the ionic concentration and pH. Fig. 6.4(a) shows

experimentally measured surface charge density variation for colloidal silica particles in

0.2 M NaCl solution obtained by Dove *et al.*[215], and comparison of these results with
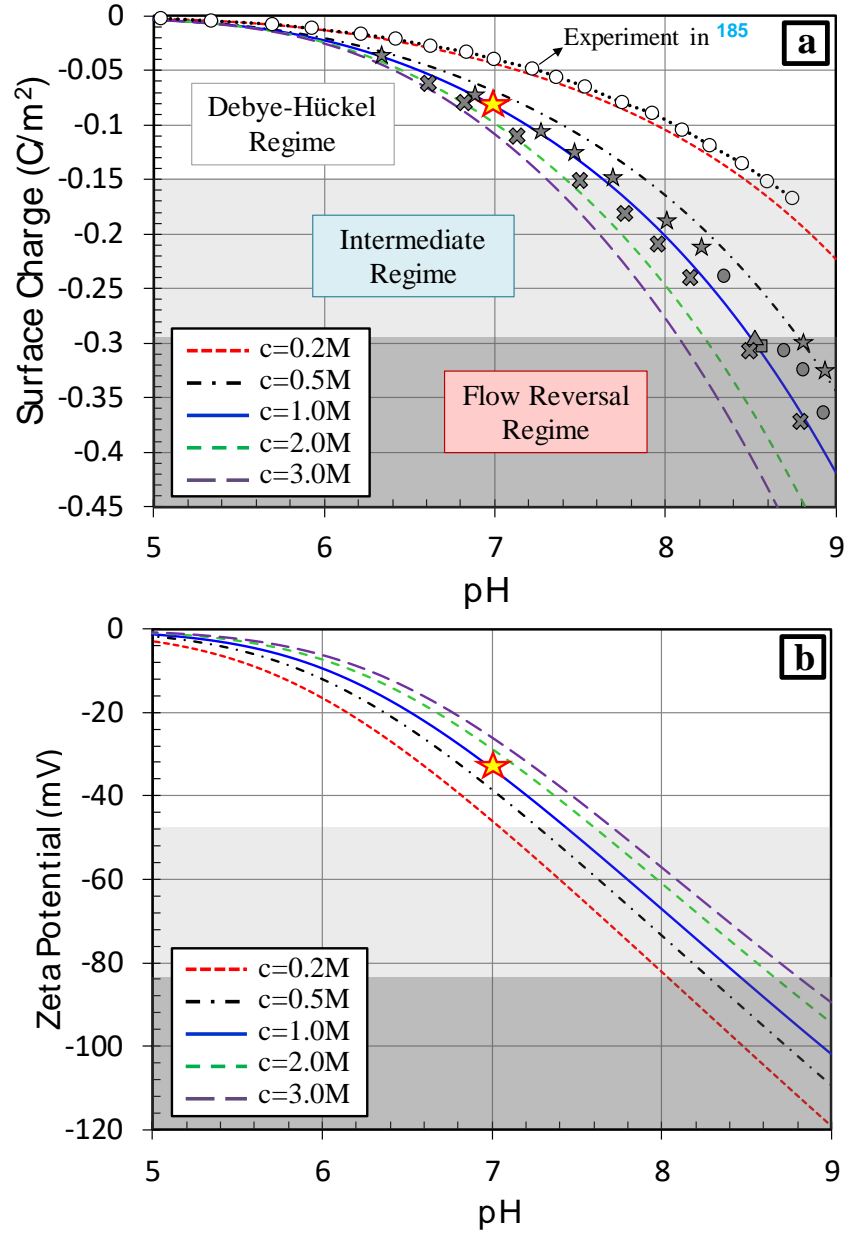
Fig 6.4 Variation of surface charge and zeta potential for different ionic concentration and pH values for NaCl solution in contact with planar silica surfaces. The △, ✖, ◯, ☐ and ✿ symbols refer to results by Qiao and Aluru[65], Rezaei *et al.*[62], Cao and Netz[200], Jelinek *et al.*[216] and several values at the present study, respectively. Experimental surface charge results (··◯··) of silica nanoparticles in 0.2 M NaCl are adopted from Dove *et al.*[215] The ★ symbol shows electrochemical conditions used in this study.

analytical solutions at the planar silica surfaces using the model in Yeh *et al.*[206] Discrepancies between the two are mostly due to the small particle size effects, as previously shown in [207]. Surface charge density values used in MD simulations by Qiao and Aluru[65], Rezaei *et al.*[62], Cao and Netz,[200] and Jelinek *et al.*[216] as well as several values used in the present study are shown in the figure with various symbols. Particularly, surface charge density values used by Rezaei *et al.*[62] and the present study show confinement within 1.0 M $\leq$ c $\leq$ 0.5 M and 6.4 $\leq$ pH $\leq$ 9 ranges. Within these conditions, the Debye-Hückel regime are identified for approximately $\sigma < 0.15$ C/m^2, where PB-S model is valid and EOF velocity increases with increased surface charge (and zeta potential). However in the 0.15 C/m$^2 \leq \sigma \leq 0.29$ C/m^2 range the EOF magnitude decreases with increased σ (Intermediate Regime), and eventually charge inversion and EOF reversal are observed for $\sigma > 0.29$ C/m^{2}[62, 65, 200, 216]. We also obtained MD results in the intermediate and flow reversal regions, which were consistent with the findings in Rezaei *et al.*[62] Since the objective of this study is EOF behavior where PB-S theory is valid, results for high surface charge density cases are not shown for brevity.

In this study, we choose the following electro-chemical conditions within the validity region of the PB theory: Monovalent NaCl solution with 1M bulk ionic concentration in silicon-based nanochannels at pH=7. These ionic conditions exhibit $\sigma_s = -0.082$ C/m^2 and $\zeta = -33$ mV, which results in 50 Na$^+$ and 28 Cl$^-$ ions in the used simulation domain. 22ē of charge of sodium excess correspond to the physical surface charge of the walls. We do not model any hydronium (H$^+$) or hydroxyl (OH$^-$) ions in the solution since the number of H$^+$ and OH$^-$ are extremely low when compared to the other

species in the solution ($pH = -\log([H^+])$). This study is conducted at pH=7, where the total number of H$^+$ or OH$^-$ ions is minimum and equal to each other. This pH value, along with the surface charge, co-ion and counter-ion concentrations ensures electrical neutrality of the bulk solution. In addition, NaCl is a neutral salt and it does not dissociate in water to produce any H$^+$ or OH$^-$ to change pH of the solution.

6.4.1 Equilibrium Simulations

Fig. 6.5 shows water density distributions obtained under five different $\varepsilon^*/\varepsilon_{Si-O}$ values. The density profiles show well-known liquid-wall interface phenomenon, creating near wall density layering and a bulk region in the middle of the channel[112]. The thermodynamic state in all our simulations are identical, since water attains a constant density of 997 kg/m^3 in the bulk region and the system's temperature is maintained at 300 K. For all $\varepsilon^*/\varepsilon_{Si-O}$ ratios, the density profiles show three pronounced layering with different magnitudes. The magnitude of the first density peak increases with increased $\varepsilon^*/\varepsilon_{Si-O}$ ratio. Larger ratio implies stronger liquid-wall interaction strength, accumulating more water molecules near silicon walls. In addition, the locations of the first density peaks remain similar under varying interaction strengths. The distance between the first density peak and wall center is about $L_O \approx 0.29$ nm. This is critical since we define an *effective channel height* (h_e) using the distance between the first density peaks as $h_e = h - 2L_O$, and base all continuum flow quantities on the effective channel height[18]. Furthermore, the (hydrodynamic) slip plane is also modeled L$_O$ away from the wall, since water molecules concentrated at the first density peak slip on the silicon surface.
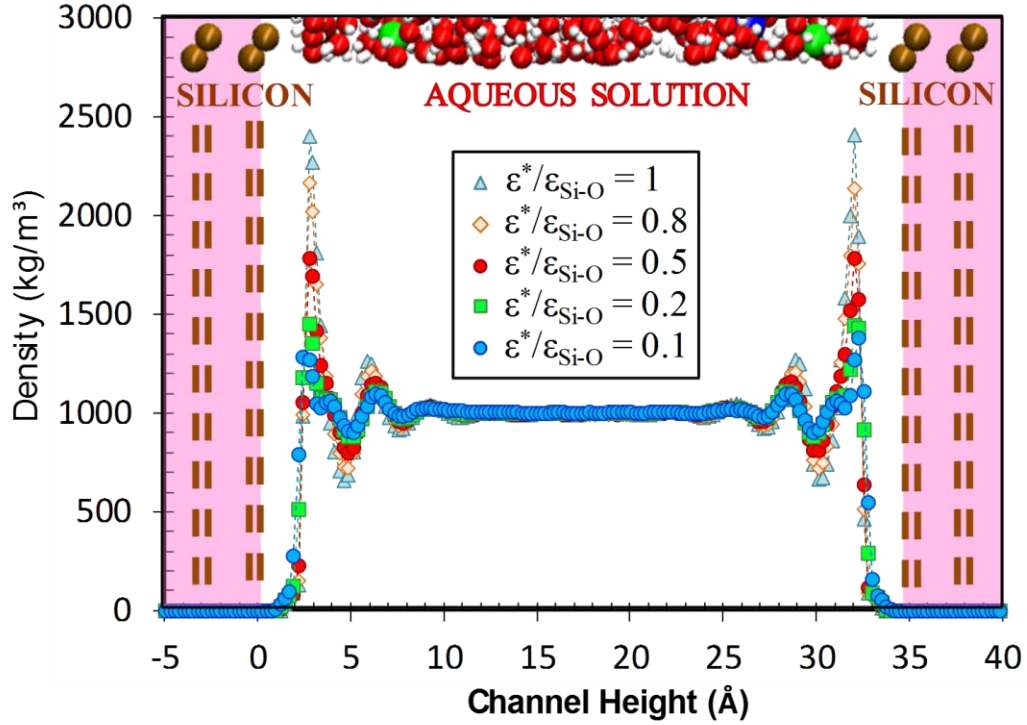
Fig 6.5 Water density profiles of 1 M NaCl obtained for different fluid-wall interaction $\varepsilon^*/\varepsilon_{Si-O}$ ratios in charged silicon nanochannels ($\sigma_s = -0.082$ C/m^2).

In Fig. 6.6, we show the ionic distribution for Na$^+$ and Cl$^-$ at $\varepsilon^*/\varepsilon_{Si-O}$=1, which is insensitive to the Si-O interaction strength. Similar to the water density profiles, ion distribution in silicon nanoconfinement also presents a layering region adjacent to the walls and a bulk region at the channel center. This behavior is mainly controlled by the wall-solvent-ion attractions as well as the net charge difference in the EDL. For monovalent NaCl solution with 1M bulk ionic concentration, Debye length is analytically calculated as $\lambda_D = 0.3$ nm using Eq. (6.14). Considering that the EDL thickness is typically $4.5\lambda_D$, we find the EDL thickness as 1.35nm. The distance between the slip plane (L$_O$) and the point with zero net electrical charge (ρ_e= 0) is about 1.1 nm, which indicates an approximate EDL thickness for MD results. Fluctuations in the counter- and co-ion distributions are due to the molecular size effects. Peak density in Na$^+$ is at z= 4.4

136

Å, which is farther away from the silicon wall than the first density peak of water at 2.9 Å. This behavior could be due to the hydration radius of Na^+, where the counter-ions could not get closer to the walls beyond a certain distance despite their atomic radius of σ=2.575 Å. These results and observations are consistent with the literature.[45]
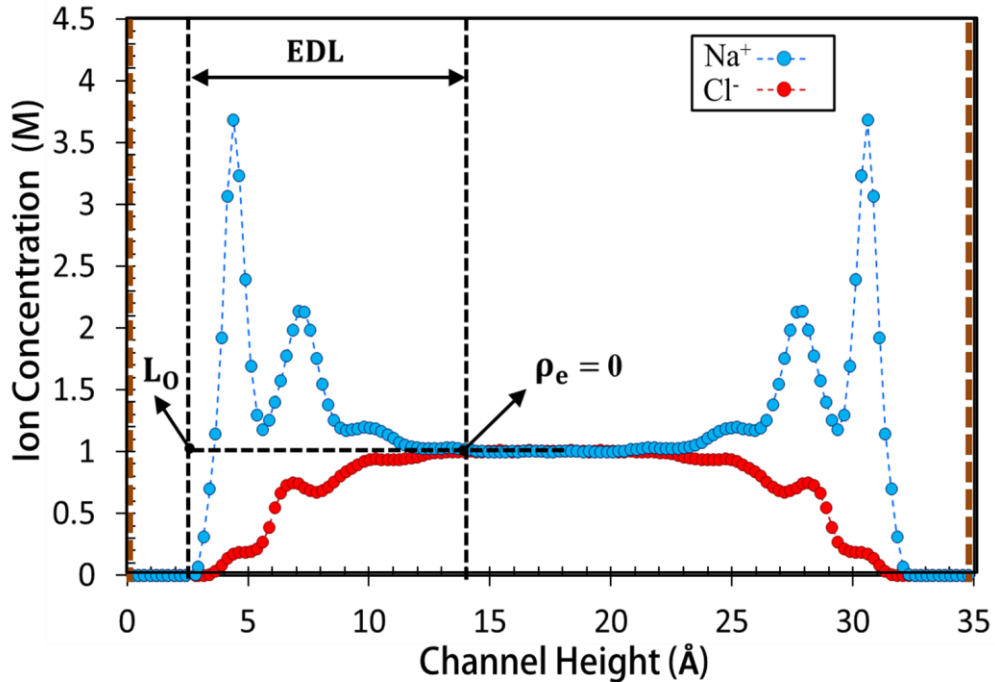
Fig. 6.6 Distribution of Na^+ and Cl^- ions in charged silicon nano channel for $\varepsilon^*/\varepsilon_{Si-O}$=1.

6.4.2 Force-Driven Flow Simulations

In order to investigate the effects of ionic concentration on viscosity of the solution, we first performed force driven flow simulations for deionized water and 1 M NaCl solution in a periodic box of 5.3nm×5.3nm×9.4nm. This approach utilizes two equal but opposite in direction body-forces acting in two equal sections of a periodic domain, which creates two counter-flowing streams in a periodic box without any confinement or wall effects[53]. Curve fitting parabolic profiles to the resulting velocity distribution enable extraction of the bulk viscosity of water. The viscosity of water using SPC/E model is

approximately 748 µPa.s at 300 K and 997 kg/m^3 density, which is in good agreement with the values reported in previous MD studies[49]. Addition of 1 M NaCl increases viscosity of the solution to 915 µPa.s. This value is consistent with the experimental values and theoretical calculations previously reported in the literature[40, 217].

Next, force driven flow simulations of 1 M NaCl solution in silicon nano channels are performed to obtain the apparent viscosities and slip lengths for various $\varepsilon^*/\varepsilon_{Si-O}$ cases. Force-driven ionic fluid flows are simulated for both charged and electrically neutral nano channels to distinguish the effects of surface charge and ionic flow on the viscosity and slip length. Fig. 6.7 shows the velocity profiles of 1 M NaCl solution in charged ($\sigma_s = -0.082$ C/m^2) and neutral silicon nanochannels normalized by the channel averaged velocity for different $\varepsilon^*/\varepsilon_{Si-O}$ cases. The normalized velocity profiles are parabolic and they exhibit increased slip length with decreased water-silicon interaction strength ($\varepsilon^*/\varepsilon_{Si-O}$). These parabolic velocity profiles are fitted to second-order polynomial equations in the form of $u(z) = Az^2 + Bz + C$. The viscosity and slip lengths are calculated by comparing the coefficients of the fitted equations with the following slip-modified continuum flow model

$$u(z) = \frac{fh^2}{2\mu}\left(-\left(\frac{z}{h}\right)^2 + \left(\frac{z}{h}\right) + \left(\frac{\beta}{h}\right)\right) \qquad (6.48)$$

where $u(z), f, \mu$ and β are the velocity field, driving-force, fluid viscosity and slip length respectively. This curve fitting method was explained extensively in previous studies[14, 53].
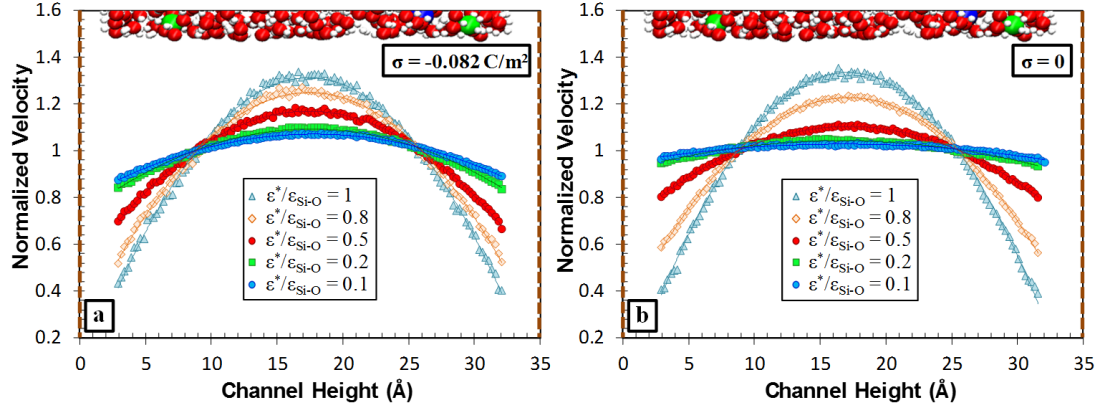
Fig. 6.7 Normalized velocity profiles of 1 M NaCl solution in (a) charged ($\sigma_s = -0.082$ C/m^2) and (b) neutral silicon nanochannels at different $\varepsilon^*/\varepsilon_{Si-O}$ ratios. Normalization was done using the channel averaged velocity

Table 6.2 shows the viscosity and slip length values of 1 M NaCl solution in both charged and neutral silicon nanochannels. Comparing with the neutral case, surface charge results in viscosity enhancement as well as reduction in the slip lengths. This behavior is mainly a result of increased interfacial strength due to the electrical charge, as previously explained[23]. For charged surfaces, the viscosities are found around 945 µPa.s at different $\varepsilon^*/\varepsilon_{Si-O}$ ratios, which indicates constant apparent viscosity for different liquid-wall interaction strengths, while the slip lengths vary in the range of 0.33-2.79 nm. The apparent viscosity and slip length in conjunction with the zeta potential have paramount importance in continuum-based analytical solution of the EOF velocity profile given in Eq. (6.35).

6.4.3 Electroosmotic Flow Simulations

In this section we focus on the development of pure EOFs under velocity slip. For cases with non-overlapping EDLs, we expect to observe plug like flow behavior in the bulk of the channel with sharp velocity gradients within the EDL region. The EOF speed in the bulk region is defined by the HS velocity with slip correction given in Eq. (6.37)

Table 6.2 Apparent viscosity and slip lengths in charged and uncharged silicon nanochannels for different $\varepsilon^*/\varepsilon_{Si-O}$ ratios. Viscosities obtained from periodic domain simulations for deionized water and 1 M NaCl solution are 748.0 and 914.6 µPa.s, respectively.

	Charged Nanochannel		Neutral Nanochannel	
	Viscosity (µPa.s)	Slip Length (nm)	Viscosity (µPa.s)	Slip Length (nm)
$\varepsilon^*/\varepsilon_{Si-O} = 1$	944.5	0.33	923.7	0.38
$\varepsilon^*/\varepsilon_{Si-O} = 0.8$	943.9	0.54	925.0	0.72
$\varepsilon^*/\varepsilon_{Si-O} = 0.5$	943.8	1.06	916.4	1.91
$\varepsilon^*/\varepsilon_{Si-O} = 0.2$	948.8	2.19	-	-
$\varepsilon^*/\varepsilon_{Si-O} = 0.1$	948.0	2.79	-	-

while the velocity profile in the half of the channel is given by Eq. (6.35). For implementation of the continuum equations we assumed the flow domain to start at the slip-plane (defined at the first water density peak from the surfaces), and therefore velocity slip and the zeta potential are imposed at L_O, which is approximately 0.29 nm away from the wall centers. Fig 6.8 presents MD calculated EOF velocity profiles for five different $\varepsilon^*/\varepsilon_{Si-O}$ ratios and compare these with the velocity profiles obtained from the continuum transport model. Each simulation case used different electric field to avoid nonlinear MD response. In order to compare the simulation results for different $\varepsilon^*/\varepsilon_{Si-O}$ ratios, we present in the figure velocity profile normalized by the applied electric field, which is known as the electroosmotic mobility of water ($\xi_{water} = u/E$). With reduced $\varepsilon^*/\varepsilon_{Si-O}$ ratio, the magnitudes of the mobilities increase due to increased slip length. For continuum predictions, we plot Eq. (6.35) using the viscosity and slip length
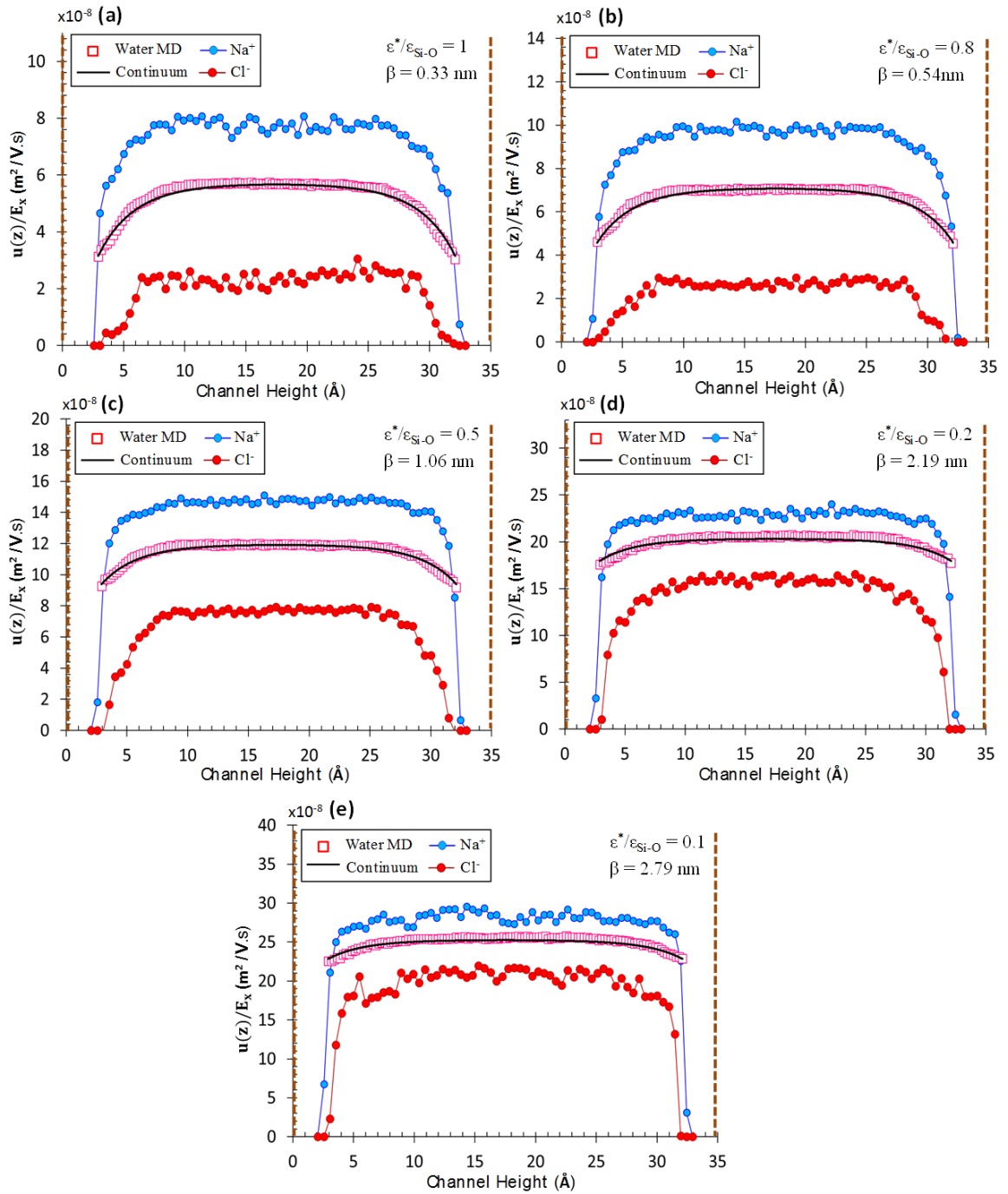
Fig. 6.8 Electroosmotic and ionic velocity profiles normalized by the applied electric field for different $\varepsilon^*/\varepsilon_{Si-O}$ values. Each case uses the corresponding slip length indicated in the figure. MD data are shown with squares while continuum predictions from **Eq. (6.35)** are represented by solid black lines. Ionic velocities for Na$^+$ and Cl$^-$ are shown by blue and red circles, respectively.

values obtained from force driven flow simulations (see Table 6.2). MD results are in good agreement with continuum profiles. For each $\varepsilon^*/\varepsilon_{Si-O}$ ratio, the continuum model can accurately predict the velocity profile both in the near wall and bulk flow regions. Comparison of the MD calculated and continuum predicted channel average velocities shows less than 2.4% variation. The EO mobility for the $\varepsilon^*/\varepsilon_{Si-O} = 0.1$ case is approximately 4.8 times larger than the $\varepsilon^*/\varepsilon_{Si-O} = 1$ case. This drastic difference is driven by 8.45 times increase in the slip length between these two cases.

We also present in Fig. 6.8 the ionic velocity distributions for various liquid-solid interaction values. For all cases, Na^+ ions move at a higher speed then the water molecules, while Cl^- ions move slower than the water molecules. This is because Na^+ ions are dominant in the diffuse layer, and they move in the applied electric field direction, while dragging electrically neutral water molecules with them. In the meantime, negatively charged Cl^- ions tend to move opposite to the applied electric field, but their motion is slower than the EOF. As a result, they move in the EOF direction but at a slower speed. These behaviors are independent of the liquid-solid interaction strength. Stokes-Einstein and Smoluchowski-Einstein equations describe an analytical formulation between ionic and water velocities, which are respectively given by

$$D_i = \frac{k_B T}{6\pi \mu r_i} \tag{6.49}$$

and

$$D_i = \frac{\xi_i k_B T}{q_i} \tag{6.50}$$

where D_i is the ion diffusivity, r_i is the Stokes radius, q_i is the ion charge, k_B is the Boltzmann constant, μ is the solvent viscosity, T is the temperature and ξ_i is the electrical mobility of the ith ion in the solution, which is defined as the ratio of ion velocity to the applied electric field $\xi_i = u_i/E$. Combining Eqs (6.49) and (6.50), an ionic mobility equation can be obtained as

$$\xi_i = \frac{q_i}{6\pi\mu r_i} \qquad (6.51)$$

Fig. 6.8 shows ionic mobilities in electroosmotic flow, which are affected by the electroosmotic mobility of water. In order to calculate the ionic mobilities in bulk flow region we calculated the average Na$^+$, Cl$^-$ and water velocities ($\bar{u}_{Na^+}$, $\bar{u}_{Cl^-}$ and $\bar{u}_{water}$) and obtained $\xi_{Na^+} = (\bar{u}_{Na^+} - \bar{u}_{water})/E$ and $\xi_{Cl^-} = (\bar{u}_{Cl^-} - \bar{u}_{water})/E$, where E is the applied electric field. Finally, using Eqs. (6.49) to (6.51) it is possible to obtain

$$\frac{r_{Cl^-}}{r_{Na^+}} = \frac{\xi_{Na^+}}{|\xi_{Cl^-}|} = \frac{D_{Na^+}}{D_{Cl^-}} \qquad (6.52)$$

According to this relation, MD calculated ionic mobilities can be compared with the ionic diffusivities at a known thermodynamic state. The diffusion coefficients of Na$^+$ and Cl$^-$ at 298 K were known as 13.3×10^{-6} and 20.3×10^{-6}cm^2/s, respectively, which results D_{Na^+} / D_{Cl^-}= 0.655 [209]. Using the average bulk velocities obtained from MD simulations (See Fig. 6.8), we calculated this ratio as 0.629, 0.627, 0.637, 0.604 and 0.669 for $\varepsilon^*/\varepsilon_{Si-O}$=1, 0.8, 0.5, 0.2 and 0.1 cases, respectively. Comparisons of MD calculations and analytical predictions based on kinetic theory are reasonable. Differences between these values are mainly due to the poor statistics of ionic velocities regarding relatively low number of ions in the solution.

Velocity distribution within the EDL for different liquid-solid interaction strength cases are shown in Fig. 6.9. The MD and continuum velocity profiles were both normalized by the slip-modified Helmholtz-Smoluchowski velocity given by Eq. (6.37), and the distance from the wall was normalized by λ_D. It is by coincidence that $L_o \approx \lambda_D$, and hence, the velocity profiles start about $z/\lambda_D \approx 1$ and extend up to $z/\lambda_D \approx 4.5$, where the electrokinetic potential reaches to zero and the EOF reach its maximum value. Comparisons of the MD results and continuum predictions in this region show reasonable agreements. Normalized velocity profiles show increased velocity slip due to weaker interfacial interactions induced by reduced $\varepsilon^*/\varepsilon_{Si-O}$ ratios, and the velocity gradients within the EDL are greatly reduced with increased slip effects.
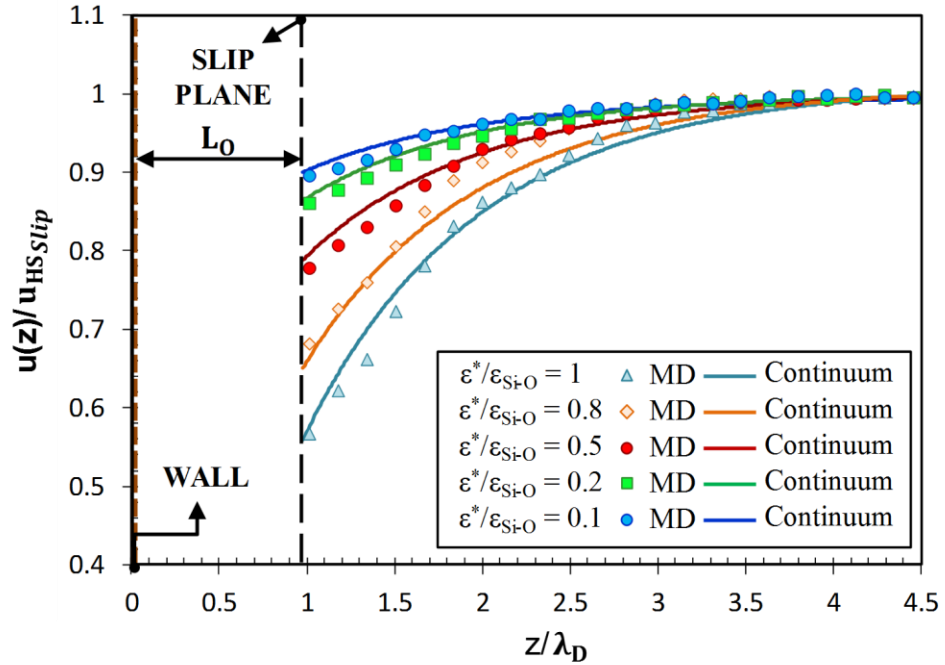
Fig. 6.9 Velocity profiles normalized by slip corrected Helmholtz-Smoluchowski electroosmotic velocity near bottom wall for various by $\varepsilon^*/\varepsilon_{Si-O}$ ratios.

Based on Eq. (6.37), enhanced EOF is a result of the normalized slip-length ($\beta^* = \beta/\lambda_D$), and it is independent from the channel height. Therefore, EOF velocity

profiles in larger channels must be similar to those obtained in smaller-scales for identical ionic conditions and electric field strength. In Fig. 6.10, we show dimensional velocity profiles in h=3.49 nm and h=6.0 nm channels with $\varepsilon^*/\varepsilon_{Si-O} = 0.5$. The velocity profiles show similar slip behavior in the near wall region for both channel sizes, with a constant bulk flow velocity. This result verifies the size independency of the electroosmotic slip flow.
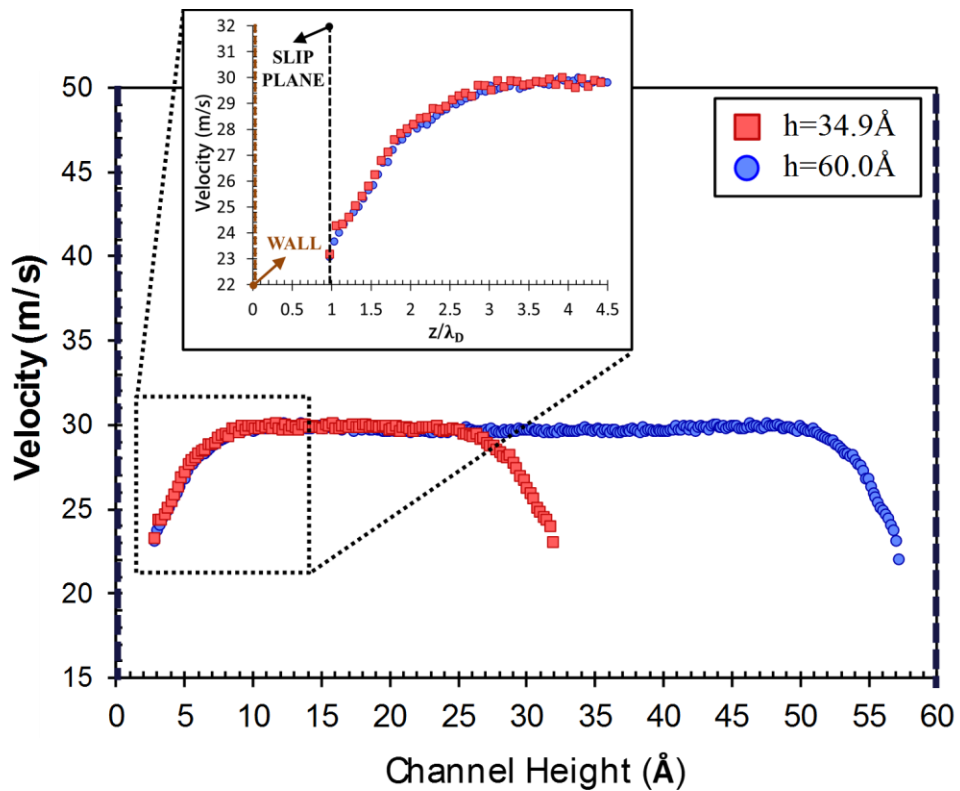
Fig. 6.10 Electroosmotic velocity profiles of 1 M NaCl solution in charged ($\sigma_s = -0.082$ C/m^2) silicon nanochannels with two different channel heights at $\varepsilon^*/\varepsilon_{Si-O} = 0.5$.

6.5 Conclusion

Electroosmotic flow in the Debye-Hückel regime is investigated using molecular dynamics simulations, and the results are compared with the predictions from analytical

solutions of the Poisson-Boltzmann and Stokes equations. Excellent agreements between the two are shown provided that the apparent viscosity of the ionic solution and the proper interfacial slip-lengths are used in the continuum model. Apparent viscosity of the ionic solution was obtained from MD simulations of force-driven salt water flow in periodic domains and charged nanochannels. In periodic domain simulations, the viscosity obtained using SPC/E water model increases nearly 26% with addition of 1M NaCl. Although nanoconfinement induced by the walls does not significantly alter the apparent viscosity of the ionic solution for the 3.49 nm height channel, wall surface charge increases the apparent viscosity compared to the uncharged surfaces. In order to obtain the slip length for ionized solution, we performed MD simulations of force-driven nanochannel flows for charged and uncharged surfaces using various silicon-oxygen interaction strengths ($\varepsilon^*/\varepsilon_{Si-O}$). The slip length increases with decreased $\varepsilon^*/\varepsilon_{Si-O}$ ratio. However, the slip-lengths for the charged surfaces are smaller than the neutral surfaces.

An interesting aspect of the analytical solution of EOF is that slip enhancement is not equivalent to having an enhanced zeta potential in pure EOF with no-slip. Velocity profile in the EDL shows a finite slip value at the first water density layer near the walls, followed with a typical viscous flow profile in the EDL that reaches the Helmholtz-Smoluchowski velocity in the bulk flow region. Therefore, HS velocity is improved due to velocity slip, which is a property of the water-surface interactions and the surface charge, while the zeta potential that depends on the ionic concentration, pH and surface chemistry, remains unaltered. This proves decoupling between the zeta potential and slip-length effects in EOF enhancement due to slip. In addition, slip length in the analytical solution is normalized with the Debye length instead of the channel height. As a result,

velocity slip and the resulting enhancement in HS velocity should be observable in micro-channels experiments. For example, one can systematically alter the ionic concentration to vary the Debye length, and measure the HS velocity in the bulk flow region to extract the slip length. However, this approach would require performing EOF experiments in high conductivity solutions, which are prone to Joule heating effects and Faradaic reactions on the electrodes.

Chapter 7

SUMMARRY AND FUTURE RESEARCH

This dissertation utilizes atomistic level simulations to enable an advanced understanding of liquid flows inside nanosized channels. Molecular dynamics simulations are carried out to investigate transport properties of nanoconfined water such as density profiles, velocity profiles, molecular orientation, flow rate, viscosity and slip lengths as a function of different physical parameters including the surface charge, electric field, channel height, wall curvature, salt ions, driving force and wall interaction strengths. Furthermore, we proposed a slip-modified analytical model that accurately predicts the electroosmotic flow in different sized nanochannels.

7.1 Summary of the Current Work

In chapter 1, a brief introduction to nanofluidics and its potential applications are discussed. Afterwards, fundamental aspects in nanoscale liquid transport phenomena are explained. Herein, we mainly target providing a broad perspective to the readers about liquid properties in nanochannels, concentrating on density, slip length, viscosity, velocity and flow rate.

Chapter 2 elaborates on molecular dynamics, which is the method used in this dissertation for all simulations. We begin with a chronological ordering of computational modeling and numerical simulations of liquids through last century, and

148

continue giving fundamental knowledge about MD simulations. Finally, we elucidate the general methodology followed in MD simulations.

In chapter 3, deionized water flows through uncharged planar graphene channels and carbon nanotubes at various channel sizes are investigated. Main objective is to clarify the effect of wall curvature and channel size on the slip characteristics of water in carbon-based nanochannels. This work also presents a detailed literature review on the slip length values of water in CNT and graphene channels that has previously been reported in many experimental and numerical studies.

Chapters 4 and 5 investigate force-driven nanochannel flow simulations of deionized water in charged graphene nanochannels. Graphene materials can act as gated electrodes when they are subjected to electrical charges. In our simulations, the planar surfaces of the nanochannel are either oppositely or identically charged. Opposite charges induce an electric field from positively charged wall to negatively charged one, while no electric field is developed between identically charged walls. The focused objectives are to display the variations on the water density distributions, molecular orientations, velocity profiles, viscosities, slip lengths and flow rates as a function of surface charges and electric field.

In chapter 6, we perform electroosmotic flow simulations (EOF) for a 3D system consisting of aqueous NaCl solution confined in charged silicon nano-channels under realistic electrochemical conditions. One of our objectives is to study the effects of slip length and viscosity variations on electroosmotic flow in silicon nano-channels. Force-driven nanochannel flow simulations present the results of viscosity and slip length (when there is a wall) of deionized and ionic solution with or without explicit wall and

charged or uncharged wall. Most importantly, we compare nano-scale electroosmotic slip flow simulations with well-known analytical continuum solutions of Poisson-Boltzmann and Stokes equations with slip correction at various liquid-solid interaction strengths.

7.2 Future Research

Nanoscale confined liquid flows have a promising future due to its relevance to many biological phenomena and potentially industrial applications. Our current studies showed many intriguing and significant outcomes, which motivate us to harness these insights in various practical nanoelectromechanical systems. For example, we would like to utilize our findings on electrofreezing of water in graphene nanochannels to create electrocrystallization driven nanoactuators. Controlled by an applied electric field, liquid pressure builds-up in graphene nanochannels, which can move the walls through electric field direction. In addition, this also allows polarizable water molecules to be transported by charge effect, which could be used as a charge driven nanopump. Furthermore, variation of viscosity due to the effect of salt ions and charge could be used to design tunable two-phase hybrid nanocomposites such as water-filled pillared graphene nanostructures. Moreover, we would like to employ our current knowledge on electroosmotic flow to explain the limits of continuum solutions. For instance, charge inversion and electroosmotic flow reversal are observed in MD simulations, while existing well-known PB equation combined with NS cannot predict these phenomena. Therefore, we plan to modify current analytical solutions of electroosmotic flow in a way that describes the flow reversal under different slip conditions. The slip conditions are well defined by changing the interaction strength between the water molecules and solid wall. Similar to the work explained in chapter 6, slip lengths and enhanced viscosities

could be taken from force-driven nanochannel flow simulations. We also target to verify the electroosmotic flow reversal at high surface charges by using microchannel experiments.

BIBLIOGRAPHY

1   R. B. Schoch, J. Han, and P. Renaud, Reviews of modern physics 80, 839 (2008).

2   J. C. Eijkel, and A. Van Den Berg, Microfluid. Nanofluid. 1, 249 (2005).

3   L. Bocquet, and E. Charlaix, Chem. Soc. Rev. 39, 1073 (2010).

4   A. Angelova, B. Angelov, S. Lesieur, R. Mutafchieva, M. Ollivon, C. Bourgaux, R. Willumeit, and P. Couvreur, J. Drug Deliv. Sci. Technol. 18, 41 (2008).

5   D. Cohen-Tanugi, and J. C. Grossman, Nano Lett. 12, 3602 (2012).

6   T. Sato, G. Masuda, and K. Takagi, Electrochim. Acta 49, 3603 (2004).

7   I. Vlassiouk, T. R. Kozel, and Z. S. Siwy, J. Am. Chem. Soc. 131, 8211 (2009).

8   X. Gong, J. Li, H. Lu, R. Wan, J. Li, J. Hu, and H. Fang, Nature nanotechnology 2, 709 (2007).

9   Y. Akkus, C. T. Nguyen, A. T. Celebi, and A. Beskok, arXiv preprint arXiv:1807.07491, (2018).

10   S. Bernard, R. Wirth, A. Schreiber, H.-M. Schulz, and B. Horsfield, International Journal of Coal Geology 103, 3 (2012).

11   J. Ghorbanian, (Southern Methodist University, 2017).

12   S. K. Kannam, B. Todd, J. S. Hansen, and P. J. Daivis, The Journal of chemical physics 135, 016313 (2011).

13   R. Hartkamp, and S. Luding, in International Conference on Multiphase Flow, Tampa, Florida (2010).

14   J. Ghorbanian, and A. Beskok, Microfluid. Nanofluid. 20, 121 (2016).

15   R. Hartkamp, A. Ghosh, T. Weinhart, and S. Luding, The Journal of chemical physics 137, 044711 (2012).

16   J. S. Hansen, B. Todd, and P. J. Daivis, Physical Review E 84, 016313 (2011).

17   K. P. Travis, and K. E. Gubbins, The Journal of chemical physics 112, 1984 (2000).

18   J. Ghorbanian, A. T. Celebi, and A. Beskok, The Journal of chemical physics 145, 184109 (2016).

19   R. J. Hunter, Foundations of colloid science (Oxford University Press, 2001).

20   A. Raghunathan, J. Park, and N. Aluru, The Journal of chemical physics 127, 174701 (2007).

21   G. J. Wang, and N. G. Hadjiconstantinou, Phys. Fluids 27, 052006 (2015).

22   W. Wu, H. Chen, and D. Sun, Phys. Lett. A 377, 334 (2013).

23   A. T. Celebi, M. Barisik, and A. Beskok, The Journal of Chemical Physics 147, 164311 (2017).

24   G. Nagayama, and P. Cheng, Int. J. Heat Mass Transfer 47, 501 (2004).

25   H. Lamb,   (Dover, New York, 1932).

26   A. Koklu, J. Li, S. Sengor, and A. Beskok, Microfluid. Nanofluid. 21, 11 (2017).

27   N. V. Priezjev, The Journal of chemical physics 127, 144708 (2007).

28   J. A. Thomas, and A. J. McGaughey, Nano Lett. 8, 2788 (2008).

29   A. A. Pahlavan, and J. B. Freund, Physical Review E 83, 021602 (2011).

30   K. Falk, F. Sedlmeier, L. Joly, R. R. Netz, and L. Bocquet, Nano Lett. 10, 4067 (2010).

31   S.-C. Yang, Microfluid. Nanofluid. 2, 501 (2006).

32   J. Marti, J. Sala, and E. Guardia, J. Mol. Liq. 153, 72 (2010).

33   A. T. Celebi, M. Barisik, and A. Beskok, Microfluid. Nanofluid. 22, 7 (2018).

34   S. Kumar Kannam, B. Todd, J. S. Hansen, and P. J. Daivis, The Journal of chemical physics 136, 024705 (2012).

35   S. Bernardi, B. Todd, and D. J. Searles, The Journal of chemical physics 132, 244706 (2010).

36   A. T. Celebi, and A. Beskok, The Journal of Physical Chemistry C 122, 9699 (2018).

37   R. Qiao, and N. Aluru, Appl. Phys. Lett. 86, 143105 (2005).

38   R. Qiao, and N. Aluru, Colloids Surf. Physicochem. Eng. Aspects 267, 103 (2005).

39   D. Out, J. Los, Solution Chem. 9, 19-35. (1980)

40   J. Kestin, H. E. Khalifa, and R. J. Correia, J. Phys. Chem. Ref. Data 10, 71 (1981).

41   M. Suk, and N. Aluru, RSC Advances 3, 9365 (2013).

42   J. A. Thomas, A. J. McGaughey, and O. Kuter-Arnebeck, International journal of thermal sciences 49, 281 (2010).

43   Qiao, R.; Aluru, N. R., . International Journal for Multiscale Computational Engineering (2004).

44   I. Bitsanis, S. A. Somers, H. T. Davis, and M. Tirrell, The Journal of Chemical Physics 93, 3427 (1990).

45   R. Qiao, and N. Aluru, The Journal of chemical physics 118, 4692 (2003).

46   B. Todd, J. Hansen, and P. J. Daivis, Phys. Rev. Lett. 100, 195901 (2008).

47   G. S. Fanourgakis, J. Medina, and R. Prosmiti, The Journal of Physical Chemistry

A 116, 2564 (2012).

48   S. Tazi, A. Boṭan, M. Salanne, V. Marry, P. Turq, and B. Rotenberg, J. Phys.: Condens. Matter 24, 284117 (2012).

49   M. A. González, and J. L. Abascal, The Journal of chemical physics 132, 096101 (2010).

50   S. Yongli, S. Minhua, C. Weidong, M. Congxiao, and L. Fang, Computational materials science 38, 737 (2007).

51   D. M. Heyes, The liquid state: applications of molecular simulations (Wiley, 1998),

52   L. Bocquet, and J.-L. Barrat, Physical review E 49, 3079 (1994).

53   J. Backer, C. Lowe, H. Hoefsloot, and P. Iedema, The Journal of chemical physics 122, 154503 (2005).

54   A. Markesteijn, R. Hartkamp, S. Luding, and J. Westerweel, The Journal of chemical physics 136, 134104 (2012).

55   G. Karniadakis, A. Beskok, and N. Aluru, Simple Fluids in Nanochannels (Springer, 2005),

56   G. E. Karniadakis, A. Beskok, and N. Aluru, Microflows and nanoflows: fundamentals and simulation (Springer Science & Business Media, 2006), Vol. 29,

57   V. Marry, J.-F. Dufrêche, M. Jardat, and P. Turq, Mol. Phys. 101, 3111 (2003).

58   L. Joly, C. Ybert, E. Trizac, and L. Bocquet, Phys. Rev. Lett. 93, 257805 (2004).

59   R. Bhadauria, and N. Aluru, The Journal of Chemical Physics 146, 184106 (2017).

60   R. Qiao, Microfluid. Nanofluid. 3, 33 (2007).

61   D. Kim, and E. Darve, Physical review E 73, 051203 (2006).

62   M. Rezaei, A. Azimian, and D. T. Semiromi, Heat Mass Transfer. 51, 661 (2015).

63   C. D. Lorenz, P. S. Crozier, J. A. Anderson, and A. Travesset, The Journal of Physical Chemistry C 112, 10222 (2008).

64   J. N. Israelachvili, Intermolecular and surface forces (Academic press, 2015),

65   R. Qiao, and N. Aluru, Phys. Rev. Lett. 92, 198301 (2004).

66   M. P. Allen, Computational soft matter: from synthetic polymers to proteins 23, 1 (2004).

67   W. Morrell, and J. Hildebrand, The Journal of Chemical Physics 4, 224 (1936).

68   N. Metropolis, and S. Ulam, Journal of the American statistical association 44, 335 (1949).

69   W. Wood, and F. Parker, The Journal of Chemical Physics 27, 720 (1957).

70   B. Alder, and T. Wainwright, The Journal of chemical physics 27, 1208 (1957).

71   A. Rahman, Physical Review 136, A405 (1964).

72   L. Verlet, Physical review 159, 98 (1967).

73   G. Harp, and B. J. Berne, The Journal of chemical physics 49, 1249 (1968).

74   A. Rahman, and F. H. Stillinger, The Journal of Chemical Physics 55, 3336 (1971).

75   J.-P. Ryckaert, and A. Bellemans, Chem. Phys. Lett. 30, 123 (1975).

76   J.-P. Ryckaert, and A. Bellemans, Faraday Discuss. Chem. Soc. 66, 95 (1978).

77   J. A. McCammon, B. R. Gelin, and M. Karplus, Nature 267, 585 (1977).

78   D. Rapaport, J. Phys. A: Math. Gen. 11, L213 (1978).

79   D. C. Rapaport, R. L. Blumberg, S. R. McKay, and W. Christian, Computers in Physics 10, 456 (1996).

80   A. A. Berlin, R. Joswik, and V. N. Ivanovich, The Chemistry and Physics of Engineering Materials, Volume Two: Limitations, Properties, and Models (CRC Press, 2015),

81   M. Ciocoiu, Materials Behavior: Research Methodology and Mathematical Models (CRC Press, 2015),

82   M. Barisik, Molecular dynamics studies on nanoscale gas transport (Old Dominion University, 2012),

83   https://en.wikipedia.org/wiki/Maxwell%E2%80%93Boltzmann_distribution

84   A. D. MacKerell, N. Banavali, and N. Foloppe, Biopolymers 56, 257 (2000).

85   J. Wang, R. M. Wolf, J. W. Caldwell, P. A. Kollman, and D. A. Case, J. Comput. Chem. 25, 1157 (2004).

86   L. Allinger, J. Am. Chem. Soc. 99, 8127 (1977).

87   J. Zielkiewicz, The Journal of chemical physics 123, 104501 (2005).

88   A. T. Celebi, M. Kirca, C. Baykasoglu, A. Mugan, and A. C. To, Computational Materials Science 88, 14 (2014).

89   S. J. Stuart, A. B. Tutein, and J. A. Harrison, The Journal of chemical physics 112, 6472 (2000).

90   M. P. Allen, and D. J. Tildesley, Computer simulation of liquids (Oxford university press, 1989),

91   D.L. Cheung, Structures and Properties of Liquid Crystals and Related Molecules from Computer Simulation. (Durham University, 2002)

92   R. Karnik, K. Castelino, and A. Majumdar, Appl. Phys. Lett. 88, 123114 (2006).

93   M. E. Suk, and N. Aluru, The Journal of Physical Chemistry Letters 1, 1590

(2010).

94   M. Majumder, N. Chopra, R. Andrews, and B. J. Hinds, Nature 438, 44 (2005).

95   J. K. Holt, H. G. Park, Y. Wang, M. Stadermann, A. B. Artyukhin, C. P. Grigoropoulos, A. Noy, and O. Bakajin, Science 312, 1034 (2006).

96   G. Liu, W. Jin, and N. Xu, Chem. Soc. Rev. 44, 5016 (2015).

97   R. Joshi, P. Carbone, F.-C. Wang, V. G. Kravets, Y. Su, I. V. Grigorieva, H. Wu, A. K. Geim, and R. R. Nair, Science 343, 752 (2014).

98   W. Xiong, J. Z. Liu, M. Ma, Z. Xu, J. Sheridan, and Q. Zheng, Physical Review E 84, 056329 (2011).

99   P. Koumoutsakos, R. Jaffe, T. Werder, and J. Walther, (2003).

100   B. Ramos-Alvarado, S. Kumar, and G. Peterson, Physical Review E 93, 023101 (2016).

101   X. Qin, Q. Yuan, Y. Zhao, S. Xie, and Z. Liu, Nano Lett. 11, 2173 (2011).

102   Q. Xie, M. A. Alibakhshi, S. Jiao, Z. Xu, M. Hempel, J. Kong, H. G. Park, and C. Duan, Nature nanotechnology, 1 (2018).

103   R. F. Cracknell, D. Nicholson, and N. Quirke, Phys. Rev. Lett. 74, 2463 (1995).

104   J. Shiomi, and S. Maruyama, Nanotechnology 20, 055708 (2009).

105   S. Plimpton, Journal of computational physics 117, 1 (1995).

106   J. L. Abascal, and C. Vega, The Journal of chemical physics 123, 234505 (2005).

107   S. Miyamoto, and P. A. Kollman, J. Comput. Chem. 13, 952 (1992).

108   T. Werder, J. H. Walther, R. Jaffe, T. Halicioglu, and P. Koumoutsakos, The Journal of Physical Chemistry B 107, 1345 (2003).

109   S. Plimpton, R. Pollock, and M. Stevens, in PPSC1997).

110   https://lammps.sandia.gov/doc/kspace_style.html

111   K. P. Travis, B. Todd, and D. J. Evans, Physical Review E 55, 4288 (1997).

112   J. Koplik, and J. R. Banavar, Annual Review of Fluid Mechanics 27, 257 (1995).

113   T. A. Ho, and A. Striolo, The Journal of chemical physics 138, 054117 (2013).

114   K. Binder, J. Horbach, W. Kob, W. Paul, and F. Varnik, J. Phys.: Condens. Matter 16, S429 (2004).

115   F. Sofos, T. Karakasidis, and A. Liakopoulos, Int. J. Heat Mass Transfer 52, 735 (2009).

116   R. S. Voronov, D. V. Papavassiliou, and L. L. Lee, Chem. Phys. Lett. 441, 273 (2007).

117   J. Thomas, and A. McGaughey, The Journal of chemical physics 128, 084715 (2008).

118   D. M. Huang, C. Cottin-Bizonne, C. Ybert, and L. Bocquet, Langmuir 24, 1442 (2008).

119   N. Wei, X. Peng, and Z. Xu, ACS applied materials & interfaces 6, 5877 (2014).

120   E. Wagemann, E. Oyarzua, J. H. Walther, and H. A. Zambrano, PCCP 19, 8646 (2017).

121   J. H. Walther, K. Ritos, E. R. Cruz-Chu, C. M. Megaridis, and P. Koumoutsakos, Nano Lett. 13, 1910 (2013).

122   E. Kotsalis, J. Walther, and P. Koumoutsakos, Int. J. Multiphase Flow 30, 995 (2004).

123   S. K. Kannam, B. Todd, J. S. Hansen, and P. J. Daivis, The Journal of chemical physics 138, 094701 (2013).

124   F. Du, L. Qu, Z. Xia, L. Feng, and L. Dai, Langmuir 27, 8437 (2011).

125   M. Whitby, and N. Quirke, Nature Nanotechnology 2, 87 (2007).

126   E. Secchi, S. Marbach, A. Niguès, D. Stein, A. Siria, and L. Bocquet, Nature 537, 210 (2016).

127   A. Maali, T. Cohen-Bouhacina, and H. Kellay, Appl. Phys. Lett. 92, 053101 (2008).

128   H. Moon, S. K. Cho, R. L. Garrell, and C.-J. C. Kim, J. Appl. Phys. 92, 4080 (2002).

129   F. Mugele, and J.-C. Baret, J. Phys.: Condens. Matter 17, R705 (2005).

130   G. Jo, M. Choe, S. Lee, W. Park, Y. H. Kahng, and T. Lee, Nanotechnology 23, 112001 (2012).

131   R. K. Kalluri, D. Konatham, and A. Striolo, The Journal of Physical Chemistry C 115, 13786 (2011).

132   J. Lyklema, Fundamentals of interface and colloid science: soft colloids (Elsevier, 2005), Vol. 5,

133   S. Joseph, and N. Aluru, Nano Lett. 8, 452 (2008).

134   J. Zhang, M. K. Borg, K. Ritos, and J. M. Reese, Langmuir 32, 1542 (2016).

135   F. Song, B. Li, and C. Liu, Langmuir 29, 4266 (2013).

136   N. Giovambattista, P. G. Debenedetti, and P. J. Rossky, The Journal of Physical Chemistry B 111, 9581 (2007).

137   C. D. Daub, D. Bratko, K. Leung, and A. Luzar, The Journal of Physical Chemistry C 111, 505 (2007).

138   R. Zangi, and A. E. Mark, The Journal of chemical physics 120, 7123 (2004).

139 J. Yan, and G. Patey, The Journal of Physical Chemistry Letters 2, 2555 (2011).

140 I. M. Svishchev, and P. G. Kusalik, Phys. Rev. Lett. 73, 975 (1994).

141 X. Xia, and M. L. Berkowitz, Phys. Rev. Lett. 74, 3193 (1995).

142 A. Yacoby, Nature Physics 7, 925 (2011).

143 Z. Wang, Y. Yang, D. L. Olmsted, M. Asta, and B. B. Laird, The Journal of chemical physics 141, 184102 (2014).

144 L. Liu, and G. Patey, The Journal of chemical physics 141, 18C518 (2014).

145 M. Barisik, and A. Beskok, International Journal of Thermal Sciences 77, 47 (2014).

146 I.-C. Yeh, and M. L. Berkowitz, The Journal of chemical physics 111, 3155 (1999).

147 S. Wei, X. Xiaobin, Z. Hong, and X. Chuanxiang, Cryobiology 56, 93 (2008).

148 I. Braslavsky, and S. Lipson, Appl. Phys. Lett. 72, 264 (1998).

149 P. Šunka, Physics of plasmas 8, 2587 (2001).

150 F. S. Cipcigan, V. P. Sokhan, A. P. Jones, J. Crain, and G. J. Martyna, PCCP 17, 8660 (2015).

151 T. A. Ho, and A. Striolo, Molecular Simulation 40, 1190 (2014).

152 C. Y. Lee, J. A. McCammon, and P. Rossky, The Journal of chemical physics 80, 4448 (1984).

153 W. R. Rice, Evolution 43, 223 (1989).

154 J. Yan, and G. Patey, The Journal of Physical Chemistry A 116, 7057 (2012).

155 N. Bjerrum, Science 115, 385 (1952).

156 T. Hozumi, A. Saito, S. Okawa, and Y. Eshita, International journal of

refrigeration 28, 389 (2005).

157   M. Orlowska, M. Havet, and A. Le-Bail, Food Res. Int. 42, 879 (2009).

158   J. Wedekind, J. Wölk, D. Reguera, and R. Strey, The Journal of chemical physics 127, 154515 (2007).

159   E.-M. Choi, Y.-H. Yoon, S. Lee, and H. Kang, Phys. Rev. Lett. 95, 085701 (2005).

160   H. Qiu, and W. Guo, Phys. Rev. Lett. 110, 195701 (2013).

161   J. Yan, and G. Patey, The Journal of chemical physics 139, 144501 (2013).

162   Å. Melinder, International journal of refrigeration 33, 1506 (2010).

163   Y. Maréchal, The hydrogen bond and the water molecule: The physics and chemistry of water, aqueous and bio-media (Elsevier, 2006),

164   J. Martı, The Journal of chemical physics 110, 6876 (1999).

165   J. D. Smith, C. D. Cappa, K. R. Wilson, B. M. Messer, R. C. Cohen, and R. J. Saykally, Science 306, 851 (2004).

166   K. Ritos, M. K. Borg, N. J. Mottram, and J. M. Reese, Phil. Trans. R. Soc. A 374, 20150025 (2016).

167   V. F. Petrenko, and R. W. Whitworth, Physics of ice (OUP Oxford, 1999),

168   K. A. Mahmoud, B. Mansoor, A. Mansour, and M. Khraisheh, Desalination 356, 208 (2015).

169   Y. Li, J. Xu, and D. Li, Microfluid. Nanofluid. 9, 1011 (2010).

170   T. Q. Vo, M. Barisik, and B. Kim, Physical Review E 92, 053009 (2015).

171   B. Radha, A. Esfandiar, F. Wang, A. Rooney, K. Gopinadhan, A. Keerthi, A. Mishchenko, A. Janardanan, P. Blake, and L. Fumagalli, arXiv preprint arXiv:1606.09051, (2016).

172   W. D. Nicholls, M. K. Borg, D. A. Lockerby, and J. M. Reese, Microfluid. Nanofluid. 12, 257 (2012).

173   W. L. Xu, C. Fang, F. Zhou, Z. Song, Q. Liu, R. Qiao, and M. Yu, Nano Lett. 17, 2928 (2017).

174   B. Chen, H. Jiang, X. Liu, and X. Hu, ACS Applied Materials & Interfaces, (2017).

175   N. Wei, X. Peng, and Z. Xu, Physical Review E 89, 012113 (2014).

176   A. Montessori, C. Amadei, G. Falcucci, M. Sega, C. Vecitis, and S. Succi, EPL (Europhysics Letters) 116, 54002 (2017).

177   B. Chen, H. Jiang, X. Liu, and X. Hu, The Journal of Physical Chemistry C 121, 1321 (2017).

178   Y. Chan, and Y. Ren, Journal of Applied Mathematics and Physics 4, 602 (2016).

179   K. Xiao, Y. Zhou, X.-Y. Kong, G. Xie, P. Li, Z. Zhang, L. Wen, and L. Jiang, (2016).

180   L. S. Puah, R. Sedev, D. Fornasiero, J. Ralston, and T. Blake, Langmuir 26, 17218 (2010).

181   P. P. Ewald, Annalen der Physik 369, 253 (1921).

182   R. W. Hockney, and J. W. Eastwood, Computer simulation using particles, 267 (1988).

183   J. S. Hub, B. L. de Groot, H. Grubmüller, and G. Groenhof, Journal of chemical theory and computation 10, 381 (2014).

184   S. Bogusz, T. E. Cheatham III, and B. R. Brooks, The Journal of chemical physics 108, 7070 (1998).

185   V. Ballenegger, A. Arnold, and J. Cerda, The Journal of chemical physics 131, 094107 (2009).

186   R. Ramsey, and J. Ramsey, Anal. Chem. 69, 1174 (1997).

187   C. Merlet, D. T. Limmer, M. Salanne, R. Van Roij, P. A. Madden, D. Chandler, and B. Rotenberg, The Journal of Physical Chemistry C 118, 18291 (2014).

188   P. Dutta, A. Beskok, and T. C. Warburton, Journal of Microelectromechanical Systems 11, 36 (2002).

189   R. Qiao, and N. Aluru, Langmuir 21, 8972 (2005).

190   L. Joly, C. Ybert, E. Trizac, and L. Bocquet, The Journal of chemical physics 125, 204716 (2006).

191   J. H. Wang, The Journal of Physical Chemistry 58, 686 (1954).

192   H. Ohtaki, and T. Radnai, Chem. Rev. 93, 1157 (1993).

193   V. Tandon, and B. J. Kirby, Electrophoresis 29, 1102 (2008).

194   Y. Ren, and D. Stein, Nanotechnology 19, 195707 (2008).

195   C. Bouzigues, P. Tabeling, and L. Bocquet, Phys. Rev. Lett. 101, 114503 (2008).

196   M.-C. Audry, A. Piednoir, P. Joseph, and E. Charlaix, Faraday Discuss. 146, 113 (2010).

197   F. H. Van der Heyden, D. Stein, K. Besteman, S. G. Lemay, and C. Dekker, Phys. Rev. Lett. 96, 224502 (2006).

198   K. Besteman, M. Zevenbergen, and S. Lemay, Physical Review E 72, 061501 (2005).

199   J. Lyklema, Colloids Surf. Physicochem. Eng. Aspects 291, 3 (2006).

200   Q. Cao, and R. R. Netz, Electrochim. Acta 259, 1011 (2018).

201   B. J. Kirby, Micro-and nanoscale fluid mechanics: transport in microfluidic devices (Cambridge university press, 2010),

202   P. Dutta, and A. Beskok, Anal. Chem. 73, 1979 (2001).

203   S. Sridharan, J. Zhu, G. Hu, and X. Xuan, Electrophoresis 32, 2274 (2011).

204   H. Schwan, Ann. N.Y. Acad. Sci. 148, 191 (1968).

205   D. Harrington, and B. Conway, Electrochim. Acta 32, 1703 (1987).

206   L.-H. Yeh, S. Xue, S. W. Joo, S. Qian, and J.-P. Hsu, The Journal of Physical Chemistry C 116, 4209 (2012).

207   M. Barisik, S. Atalay, A. Beskok, and S. Qian, The Journal of Physical Chemistry C 118, 1836 (2014).

208   K. Graf, and M. Kappl, Physics and chemistry of interfaces (John Wiley & Sons, 2006),

209   L. Yuan-Hui, and S. Gregory, Geochim. Cosmochim. Acta 38, 703 (1974).

210   J. M. Paz-Garcia, B. Johannesson, L. M. Ottosen, A. Ribeiro, and J. Rodriguez-Maroto, Electrochim. Acta 150, 263 (2014).

211   S. Atalay, M. Barisik, A. Beskok, and S. Qian, The Journal of Physical Chemistry C 118, 10927 (2014).

212   P. Mark, and L. Nilsson, The Journal of Physical Chemistry A 105, 9954 (2001).

213   Y. Wang, Y. Wang, K. Chen, and B. Li, Chem. Eng. Sci. 66, 2807 (2011).

214   M. Patra, and M. Karttunen, J. Comput. Chem. 25, 678 (2004).

215   P. M. Dove, and C. M. Craven, Geochim. Cosmochim. Acta 69, 4963 (2005).

216   B. Jelinek, S. D. Felicelli, P. F. Mlakar, and J. F. Peters, in ASME 2009 International Mechanical Engineering Congress and Exposition (American Society

of Mechanical Engineers, 2009), pp. 1511.

217   Z. Hai-Lang, and H. Shi-Jun, Journal of Chemical & Engineering Data 41, 516 (1996).